

Methods for the Numerical Simulation of Combustion Instabilities

A thesis accepted by the Faculty of Aerospace Engineering and Geodesy of the
Universität Stuttgart in partial fulfillment of the requirements for the degree of
Doctor of Engineering Sciences (Dr.-Ing.)

by

Dipl.-Ing. Francesca B. Rebosio

born in Genova

main referee: Prof. Dr.-Ing. Manfred Aigner

co-referee: Prof. Dr.-Ing. Hans-Jörg Bauer

Date of defence: 20th December 2012

Institute of Combustion Technology for Aerospace Engineering
University of Stuttgart

Acknowledgements

The research presented in this work was carried out during my experience as a researcher at the Institute for Combustion Technology of the German Aerospace Centre in Stuttgart. There I spent fruitful years, confronting myself with challenging research topics, meeting and working with researcher from different countries and cultures and growing in my professional position. Therefore I first like to express my deep gratitude to Prof. Dr.-Ing Manfred Aigner, head of the institute, who gave me the opportunity to join his staff and supervised my research. My gratitude and appreciation goes also to Prof. Dr.-Ing. Hans-Jörg Bauer, for his interest in my work and for accepting to be the co-referee of this doctoral thesis.

Furthermore I would like to express my very great appreciation to Dr.-Ing. habil. Berthold Noll, my research project supervisor, and Dr.-Ing. Massimiliano Di Domenico, former team leader of the DLR-THETA group. This work would not have been the same without their guidance, encouragement and useful critiques. I would also like to extend my thanks to Dr.-Ing. Daniele Panara, Dr.-Ing. Karina Nold, Dr. Patrick Le Clercq, Dr.-Ing. Peter Ess, Dr. Adam Steinberg, Jean-Michel Lourier and Georg Eckel. They were always there for a challenging technical discussions, for advices, critics and slowly became not just colleagues but good friends. Moreover I would like to acknowledge the support of the Combustion Diagnostic Department, in particular Dr.-Ing Michael Stöhr and Dr.-rer.-nat Wolfgang Meier.

I would like to offer my special thanks to the computing center of the University Karlsruhe and the Jülich Supercomputing Centre (JSC): the simulations presented in section 4.2 were performed on the high performance computer HP XC4000 at the computing center of University Karlsruhe, while those reported in section 4.3 were performed on the JUROPA supercomputer at the JSC under the NIC project number 3793.

Last but not least I would like to thank my family and friends, in particular my parents, Attilio and Martin: they were always there, they supported me in all the hard moments and tough decisions and always believed in me.

Contents

List of Figures	7
List of Tables	11
List of Symbols	13
Zusammenfassung	15
Abstract	17
1 Introduction	19
1.1 State of Research - Motivation	19
1.2 Goals of this work	21
2 Combustion Instabilities	23
2.1 Fundamentals of Low and High Frequency Combustion Instabilities	25
3 Computational Fluid Dynamics	27
3.1 The Governing Equations	27
3.2 Turbulent Flows and Turbulent Combustion	28
4 Experiences in Modeling Combustion Instabilities	31
4.1 Numerical Methods	31
4.2 Low Frequency Instabilities	34
4.3 High Frequency Instabilities	59
5 The Triple Decomposition Method	75
5.1 The Triple Decomposition Ansatz	75
5.2 The TDM Equations	77
5.3 Application of the Triple Decomposition Method	78
5.4 A Solution Methodology	79
6 Verification of the Triple Decomposition Method	83
6.1 The Square Cylinder Test Case	83
6.2 Results	85

7 Conclusions	93
Bibliography	95

List of Figures

4.2.1	Schematic drawing of the DLR gas turbine model combustor.[95]	35
4.2.2	Model combustor: computational domain.	36
4.2.3	Postprocessing equipment.	38
4.2.4	Time-averaged axial velocity field, $[m/s]$.	39
4.2.5	Baseline testcase. Streaklines plot of the time-averaged velocity field, in $[m/s]$.	40
4.2.6	Baseline testcase. Radial profiles of time-averaged and RMS velocities in $[m/s]$ on line $x = 10mm$. The green lines indicate case A, the red lines case C and the blue dots the experiment.	41
4.2.7	Baseline testcase. Radial profiles of time-averaged and RMS velocities in $[m/s]$ on line $x = 40mm$. The green lines indicate case A, the red lines case C and the blue dots the experiment.	42
4.2.8	Baseline testcase. Radial profiles of time-averaged and RMS velocities in $[m/s]$ on line $x = 90mm$. The green lines indicate case A, the red lines case C and the blue dots the experiment.	43
4.2.9	Time-averaged temperature profiles in $[K]$, from the baseline simulation (green line) against experiments (blue dots).	44
4.2.10	Time-averaged profiles of mixture fraction and methane mass fraction from the baseline simulation (green line) against experiments (blue dots).	44
4.2.11	Time-averaged temperature profiles in $[K]$ from case A (green line), case B (black line) against experiments (blue dots).	45
4.2.12	Case B: Simulation zones where EDM and FRC are active. The red zones are the EDM controlled zones, while the blue zones are FRC controlled.	46
4.2.13	Baseline testcase. Radial profiles at $x = 10mm$ for time-averaged, RMS temperature in $[K]$, mass fraction of CH_4 and mixture fraction. The green lines indicate case A, the red lines case C and the blue dots the experiment.	47
4.2.14	Baseline testcase. Radial profiles at $x = 20mm$ for time-averaged, RMS temperature in $[K]$, mass fraction of CH_4 and mixture fraction. The green lines indicate case A, the red lines case C and the blue dots the experiment.	48
4.2.15	Time-averaged reaction rate for CH_4 equation, $[mol/(cm^3s)]$.	49
4.2.16	Contour plot of time-averaged temperature in K .	49
4.2.17	Case C: Contour plot of time-averaged temperature in $[K]$, overlapped with experimental contour plots.	50

4.2.18	Baseline testcase. Streaklines plot of an instantaneous velocity field, [m/s]. . .	51
4.2.19	Baseline testcase. Unsteady structures: helical and tornado-like vortex described by iso-surface of pressure.	52
4.2.20	Representative pressure spectrum.	52
4.2.21	Case C. Planar velocity vectors on temperature contour, in [K].	53
4.2.22	Case C. Development of the reaction rate contour, [$mol/(cm^3s)$], on surface A over a PVC period.	54
4.2.23	Case C. Development of the reaction rate (step 1), [$mol/(cm^3s)$], on plane B over a PVC period.	55
4.2.24	Case C. Development of temperature contour, in [K] on plane B over a PVC period.	56
4.2.25	Case C. Development of the reaction rate contour, [$mol/(cm^3s)$], on plane A over a PVC period.	57
4.2.26	Case C. Scatter plots.	58
4.3.1	Schematic representation of the computational domain.	59
4.3.2	Grid adopted in the simulations.	61
4.3.3	Monitor points and radial profiles used for post-processing.	62
4.3.4	Resolved turbulence ratio (R_{Tu}) contour plots and isolines at $R_{Tu} = 0.8$	63
4.3.5	Instantaneous axial velocity field [m/s] for case $LSC - L_{60mm}$ performed with URANS and hybrid LES/RANS approach.	64
4.3.6	Contour plots of time-averaged axial velocity [m/s] and streaklines.	65
4.3.7	Contour plots of time-averaged pressure [Pa].	66
4.3.8	Radial profiles of time-averaged velocity components [m/s] at $h = 20$ mm. Red lines: case $B - L_{60mm}$. Green lines: case $W - L_{60mm}$	67
4.3.9	Contour plots of time-averaged temperature [K].	68
4.3.10	Radial profiles of time averaged temperature [K]. Red lines: case $B - L_{60mm}$. Blue lines: case $B - L_{40mm}$	68
4.3.11	Case $B - L_{60mm}$. Power spectra from the Fourier analysis at monitor point 1. .	70
4.3.12	Case $W - L_{60mm}$. Power spectrum from the Fourier analysis of the temperature signal at monitor point 1.	70
4.3.13	Case $B - L_{60mm}$. Reconstructed profiles for frequency $f = 2650$ Hz of temperature and methane mass fraction at monitor point 1.	71
4.3.14	Case $B - L_{60mm}$. Analysis of the acoustic modes of the chamber. Eigenfrequency at 2464 Hz.	72
4.3.15	Power spectra of pressure signal at monitor point 12.	72
4.3.16	Case $B - L_{40mm}$. Development of the pressure isosurface at 500400 Pa over a period at $f = 3300$ Hz.	73
4.3.17	Instantaneous pressure field [Pa].	73
4.3.18	$LSC - L_{60mm}$: Power spectra of axial velocity signal at monitor point 1. . . .	74

5.0.1	Schematic representation of time and length scales in a complex CFD simulation.	76
5.4.1	Flowchart of the SIMPLE algorithm.	80
5.4.2	Flowchart of of the solution strategy of the TDM equations.	81
5.4.3	Time development of the solution.	82
6.1.1	Original computational domain, as reported by Bosch et al., [7].	84
6.1.2	Monitoring points.	85
6.2.1	Instantaneous axial velocity field.	86
6.2.2	Simulation without TDM: Time-averaged axial velocity field.	87
6.2.3	Instantaneous Y-velocity field.	87
6.2.4	Feedback field at convergence.	88
6.2.5	FFT of the benchmark simulation.	89
6.2.6	FFT of tilde field quantites from the TDM simulation.	90

List of Tables

4.1	Constant standard values for the SST-SAS model	33
4.2	DLR gas turbine model combustor: experimental flame parameters.	36
4.3	DLR gas turbine model combustor: performed simulations.	37
4.4	Basic testcases set up for the swirled, lean, premixed can combustor configuration.	60
4.5	Main features of the testcases for the swirled, lean, premixed can combustor configuration.	60
6.1	Main parameters for the square cylinder testcase.	84

List of Symbols

Roman symbols

D	Size of the square rod	m
e_t	Stored energy	J/kg
f_{osc}	Characteristic frequency of a general oscillation	Hz
f_s	Shedding frequency	Hz
f	Body force per unit volume	m/s^2
h	Specific enthalpy	J/kg
j_{nj}	Mass diffusion flux of species n in j-direction	$kg/(m^2s)$
k	Turbulent kinetic energy	m^2/s^2
L	Characteristic length	m
p	Pressure	Pa
p'	Pressure fluctuation	Pa
q	Heat flux	W/m^2
q'_{th}	Heat release rate	W
S	Strouhal number	
t	Time	s
U	Block velocity imposed at inlet	m/s
u_i	Velocity vector components	m/s
V	Characteristic velocity	m/s
Y_n	Mass fraction of species n	

Greek symbols

β	Swirling angle in a combustion chamber	
ϵ	Dissipation rate of the turbulent kinetic energy	m^2/s^3
λ	Second viscosity	$kg/(ms)$
μ	Dynamic viscosity	$kg/(ms)$
ω	Turbulent eddy frequency	$1/s$
ω_n	Mass rate of production of species n	$kg/(m^3s)$
ω_r	Radiation term	$J/(m^3s)$
Φ	Generic scalar quantity	
ρ	Density	kg/m^3
τ_{ij}	Stress tensor	$kg/(ms^2)$
ν	Viscosity	m^2/s
ϕ	General field variable	

Zusammenfassung

Die Auslegung heutiger Gasturbinenbrennkammern erfolgt mit dem Ziel einer effizienten Verbrennung mit niedrigen Emissionen. Um dies zu gewährleisten, geht der Trend von Diffusionsflammen hin zu mageren, vorgemischten Verbrennungskonzepten. Die einströmende Frischgas Mischung wird mit einem Drall in die Brennkammer eingebracht, um eine gleichförmige Temperaturverteilung in der Verbrennungszone zu erhalten und die Flammenwurzel am Brennkammereinlass zu stabilisieren. Somit laufen die chemischen Reaktionen in einem klar definierten Bereich ab. Die Problematik vorgemischter, verdrallter, magerer Flammen liegt in der hohen Neigung zu ungewollten Verbrennungsinstabilitäten. Im Rahmen dieser Arbeit werden Verbrennungsschwingungen im Hinblick auf die zu Grunde liegende Physik der instationären Phänomene analysiert und ein besonderer Fokus auf Methoden und Modelle zur numerischen Simulation der Verbrennungsdynamik gelegt.

Nach einer allgemeinen Einführung in die Thematik und einer Definition der Ziele dieser Arbeit in Kapitel 1, werden in Kapitel 2 die Hauptunterschiede zwischen niederfrequenten und hochfrequenten Schwingungen hervorgehoben. Die Forschungsergebnisse in der veröffentlichten Literatur zeigen einen Kenntnismangel und Forschungsbedarf insbesondere im Bereich hochfrequenter Instabilitäten. Kapitel 3 liefert den mathematischen Hintergrund und beschreibt Methoden und Modelle der numerischen Strömungssimulation, welche in Kapitel 4 auf technisch relevante Brennkammerkonfigurationen angewandt werden. Das Ziel der Simulationen war auf der einen Seite die Bewertung der Stärken und Schwächen heutiger, modernster numerischer Methoden und Modelle. Auf der anderen Seite lag der Schwerpunkt darauf, ein besseres Verständnis der physikalischen Phänomene der nieder- und hochfrequenten Verbrennungsinstabilitäten zu erlangen. Niederfrequente Instabilitäten wurden anhand einer Drallbrennkammer unter mageren Bedingungen, nahe der mageren Verlöschgrenze untersucht. Die numerische Lösung zeigte thermo-akustische Instabilitäten und erfasste niederfrequente Oszillationen, welche in direkter Verbindung mit lokalem Flammenverlöschern und Wiederezünden stehen. Diese zwei Phänomene stellen Vorläufer eines vollständigen Verlöschens der Flamme dar. Intrinsische Verbrennungsinstabilitäten, die als Ursache hochfrequenter Oszillationen gelten, wurden mittels einer vereinfachten Brennkammergeometrie untersucht. Die Simulationsergebnisse dienen einer genaueren Beschreibung und Erklärung der Instabilitäten in Flammen nahe der Verlöschgrenze und führten zu einer Theorie eines möglichen Mechanismus als Ursache hochfrequenter Instabilitäten. Anhand der Simulationen zeigte sich, dass ein hoher numerischer Aufwand notwendig ist, um komplexe Verbrennungsprozesse numerisch zu erfassen.

Um hochfrequente Oszillationen in äußerst turbulenten Strömungen reproduzieren zu können, bedarf es der Fähigkeit, die Entstehung kohärenter Strukturen hoher Frequenz und kleiner Amplituden und deren Bewegung im turbulenten Feld wiederzugeben. Die Komplexität dieses Problems besteht in der Tatsache, dass ein großer Bereich zeitlicher und räumlicher Skalen aufgelöst werden muss. Unter diesen Voraussetzungen können mit konventionellen, d.h. auf einer Reynoldsmittelung (RANS) basierenden, Methoden die verschiedenen Skalen nicht unterschieden werden. Um diesen Informationsverlust zu vermeiden, sind Large Eddy Simulationen (LES) oder hybride LES/RANS Methoden (Kapitel 4) notwendig. Diese führen jedoch zu einem sehr hohen Rechenaufwand. Die oben genannten Überlegungen bezüglich der Modellierung der Skalen legen den Schluss nahe, alternative Methoden zu standardmäßigen RANS und LES Ansätzen zu erforschen. So wird in Kapitel 5 ein andersartiger, numerischer Ansatz, die sogenannte Triple Decomposition Methode (TDM) und deren mathematische Grundlagen vorgestellt. Die analytische Formulierung basiert auf der Annahme, die unabhängigen Strömungsvariablen in einen mittleren, einen kohärenten und einen stochastischen Anteil aufzuteilen; dies führt zu einer Zerlegung der Navier-Stokes-Gleichung in zwei Gleichungen, je eine für das gemittelte und das kohärente Strömungsfeld. Nach der Definition der TDM-Gleichungen wird deren Implementierung in den wissenschaftlichen CFD-Code DLR-THETA beschrieben. Die numerische Lösung des neuen Gleichungssystems ermöglicht die in Kapitel 6 beschriebene Simulation des zeitgemittelten Strömungsfeldes und der kohärenten Strukturen, welche sich durch das Strömungsgebiet bewegen. Die Verifikation der TDM-Gleichungen erfolgte mittels des Testfalles eines querangeströmten, quadratischen Zylinders. Die Wahl des Testfalles ist begründet in seiner guten Dokumentation in der Literatur als auch in seinen klar definierten, selbsterregten und kohärenten Oszillationen in einem turbulenten Strömungsfeld. Die Stärke des untersuchten Skalenseparationsansatzes und dessen numerischer Implementierung, welche im Rahmen dieser Arbeit verwirklicht wurde, zeigt sich im geringen Rechenaufwand, welcher mit standardmäßigen RANS-Ansätzen vergleichbar ist. Eine tiefer gehende Diskussion der im Rahmen dieser Forschungsarbeit erzielten Ergebnisse befindet sich in Kapitel 7.

Abstract

To date engineering requirements on combustion processes are efficiency and low emissions, therefore the technology in modern gas turbines moves from diffusive towards lean premixed flames. Even more uniform combustion conditions can be achieved when creating swirled flows in combustion devices, thus enabling to produce a uniform temperature field in the combustion zone and to anchor the flame in well defined regions of the combustion chamber. The very critical point, when employing lean premixed swirled flames, resides in the fact that the combustion process can undergo undesired unsteady processes and so called combustion instabilities can arise. This work aims to contribute to the research effort done in the past decades regarding combustion instabilities, with a focus on numerical methods and models for the simulation of combustion dynamics and on the physics, which explains the fundamentals of such unsteady phenomena.

After a general introduction on the topic and the definition of the goals of this work, given in chapter 1, chapter 2 highlights the main differences between high and low frequency instabilities. From the overview of the main research outcomes in the field, given in section 2.1, a lack of knowledge, in particular regarding high frequency instabilities, is identified. Chapter 3 provides the mathematical background and describes the numerical methods and models, which are adopted in chapter 4 to perform Computational Fluid Dynamics (CFD) simulations on technical relevant combustion chamber configurations. The scope of these simulations was on one hand to assess the strength and limit of nowadays cutting edge numerical methods and models, and on the other hand to gain better understanding on the physics of low and high frequency combustion instabilities. In fact section 4.2 provides the analysis of a swirled combustion chamber at very lean conditions, next to weak extinction limit. The resolved computational field exhibits, as expected, thermo-acoustic instabilities but also properly captures low frequencies dynamics, linked directly to local flame extinction and reignition, which are precursors of the flame blow off itself. Moreover, in section 4.3 intrinsic combustion unsteadiness, considered responsible for the arising of high frequency oscillations are studied in a simplified combustion chamber geometry. Thus, the first outcome of the simulations was the better explanation of instabilities in flames near to the blow off limit and the suggestion of a possible mechanism leading to high frequency instabilities. Anyhow these simulations also showed what a high computational cost is required when complex combustion processes are resolved numerically. In fact, in order to be able to reproduce high frequency oscillations in strongly turbulent flows, it is mandatory to succeed in solving the development of coherent structures, with high frequencies and small amplitudes, which travel across the turbulent field; the complexity of this problem

is that a very wide range of time and space scales must be solved at the same time. In such a situation the simulation with conventional Reynolds Averaged Navier Stokes (RANS) methods could not allow to distinguish the different scales, with a loss of information; therefore, to overcome the problem, Large Eddy Simulations (LES) or LES/RANS hybrid methods, as those used in chapter 4, are required, which though lead to very high computational cost. The above mentioned considerations on scale modeling suggested the research on methods alternative to the standard RANS and LES approaches: in chapter 5 the mathematical background of a different numerical approach, the so-called Triple Decomposition Method (TDM), is presented. The analytical formulation is based on the assumption of splitting the independent flow field variables in mean, coherent and random quantities; this leads to a different formulation of the Navier Stokes equation, which is decomposed in two equations, one for the mean and one for the coherent flow field. Furthermore, section 5.4 describes the numerical approach to implement the TDM equations in the DLR-THETA code, a CFD research code. Finally, the numerical solution of the new set of equations allows the simulation of correlated fields representing a time-averaged flow field and of coherent disturbances traveling across it respectively, as shown in chapter 6. For the verification of the TDM equations, the chosen test case was the square cylinder, which suited our scope well for two reasons: first it is a very well documented test case in the literature and furthermore it reveals a simple and well defined self-excited coherent oscillation in a turbulent flow field. The strength of the investigated scale splitting technique and of its numerical implementation, as achieved in the present work, resides in the low computational effort required, which is comparable to a standard RANS approach; anyhow, a deeper discussion of the results of this work is presented in chapter 7.

1 Introduction

1.1 State of Research - Motivation

Modern gas turbines (GT) are designed to achieve high efficiency with low exhaust emissions. The two key parameters to enhance efficiency are the pressure ratio, directly dependent on the compressor parameters and the temperature at the turbine rotor inlet. The life of the turbine is directly dependent on this temperature, in fact, even though materials and cooling techniques are constantly improving, there will still be a maximum temperature above which the thermal stress on the first stage vanes becomes too high. Regarding emissions more and more stringent limits are prescribed and pollutants, which till twenty years ago were not considered critical, like NO_x , are now strictly controlled and minimized, due to their proven environmental impact, [43], [93]. The principal pollutants, which are created during the combustion process in a GT, are unburnt hydrocarbons (UHC), nitro-oxides (NO_x , mainly thermal and prompt), carbon monoxide (CO) and soot. Unfortunately, often achieving the minimum emission of one pollutant implies higher emission of another one. Throughout this work just gaseous fuels are taken into account and therefore issues like atomization and evaporation, which are very important to control emission levels in liquid-fueled GT, are not relevant in this survey. When burning gaseous fuels, the concentration of pollutants in the combustion products is influenced mainly by the equivalence ratio of the mixture, the homogeneity of the fuel/air mixture in the combustion zone, or in the primary combustion zone for staged combustion, the temperature in the combustion region, the pressure at which the combustion process takes place, the residence time of the products in the combustion chamber and quenching effects,[10]. Moreover, following the trend in the development of new GT combustors, this work focuses on partially premixed and perfectly premixed lean combustion.

Lean premixed flames can reduce pollutant formation drastically: the lower flame temperature, compared to stoichiometric combustion, minimizes the production of thermal NO_x and lowers also the creation of HCN, which constitute the main species for the path of the formation of prompt NO, [40]. Premixed flames enable a more efficient combustion, the homogeneous distribution of the reactants abates the production of UHC and CO, which otherwise can be formed in rich fuel pockets. On the other hand lean conditions slow down the oxidation process of the carbon oxides into carbon dioxide and the further combustion of unburnt hydrocarbons. Therefore a sufficient long residence time shall be chosen to compensate this drawback. It also is to remark, that at too lean conditions, i.e. next to lean blow out, the CO concentration grows exponentially due to local flame extinction; this operating condition is also to be avoided. Lean

conditions are also positive for the reduction of the formation of polycyclic aromatic hydrocarbons (PAHs), precursors of soot, so that soot for lean premixed combustion is not considered an issue.

Taken into account the above mentioned constrains, combustion in state-of-the-art stationary gas turbines is lean and premixed. For stationary GT, the combustion chamber operates as follows: premixed air/fuel mixture is fed to the chamber, the inlet configuration can force the mixture to follow a swirled path and therefore to create large recirculation zones in the combustion chamber, which anchor the flame at the burner tip through the recirculation of hot combustion products in the main reaction zone, avoiding the formation of hot and cold spots and thus keeping the flame compact, viz. achieving relative short residence times in the combustor, [32]. However, this lean premixed swirled combustion chambers are prone to instabilities, which can cause structural damages due to large amplitude vibrations and/or high thermal loads at walls and can also affect the combustion process and result in flame flashback and blow off, [45]. These so-called combustion instabilities are driven by different mechanisms, can have different feedback loops and can be associated with different characteristic frequencies. In the following it is distinguished between low and high frequency combustion instabilities and in Chapter 2 a description of the research done till now on both types of dynamics is presented.

Over the years, the studies on unsteady combustion phenomena have been carried out both through experiments and numerical analysis. In particular Computational Fluid Dynamics (CFD) has grown in importance in the past decades, thanks to the scientific research effort and the resulting improvement in numerical methods and models but also thanks to always more powerful super-computers. In fact, as very well described by Westbrook et al. in their review publication on computational combustion, [96], the continuous increase in computer power enabled a constant enhancement in turbulent combustion modeling. This is due to the possibility of increasing the complexity of the combustion models, which can take into account a more accurate description of the chemical kinetic processes, with a constantly growing number of species considered, and to the chance of using at the same time very complex turbulence models, which reproduce a much larger spectrum of the turbulent scales. Therefore CFD is nowadays a reliable tool in the design of new combustion chambers as well as in the research; in particular well validated numerical tools can be used also to understand the physics of the combustion processes, improving the data from the experimental practice, because CFD enables to gain comprehensive datasets in regions of the combustion chamber, which are hard to detect thorough experiments, [17]. Though, the use of numerical tools for simulating unsteady combustion phenomena still presents some issues; the Reynolds Averaged Navier Stokes (RANS) approach, also in its time-resolved form, URANS, described in Chapter 3 has been proven of not being capable of resolving all time and space scales, which play crucial roles in highly turbulent unsteady combustion, [68]. In order to be able to solve a large multitude of time and spaces scales the LES approach shall be adopted, which is highly time consuming. The computational effort becomes almost prohibitive, even for modern super-computers, if, in addition to turbulence resolution by means of LES, also for combustion modeling more complex

approaches, e.g. finite rate chemistry,[18], are chosen; this finally confines such very complex and advanced simulations to the research facilities. An interesting method to reduce the CPU time is to adopt hybrid LES/RANS methods, as it has been done in this work, although the time needed for the simulation would still be too much for industrial applications.

1.2 Goals of this work

This work addresses the problem of combustion instabilities in gas turbines combustion chambers; the study focuses on the numerical methods and models, which can be used for CFD simulation of unsteady turbulent combustion and also on the mechanisms originating and controlling low and high frequency combustion unsteady phenomena.

Within this framework, three issues constitute the core of the analysis carried out in this essay. At first today's cutting edge numerical models for turbulent combustion have been adopted for the simulation of unsteady combustion processes in lean premixed GT combustion chamber configurations. Through these computations the reliability as well as the limits of the CFD models could be tested.

Once the numerical results have been proven against experimental data and have demonstrated to reproduce unsteady turbulent combustion phenomena correctly, the simulations could be used for the second key issue of this work, i.e. to gain a better understanding of the physics of low and high frequency combustion instabilities. In fact for low frequency instabilities a very lean flame, next to the weak extinction limit, has been chosen with the scope of investigating thermo-acoustic instabilities and also low frequency phenomena typical of lean blow off conditions, i.e. local extinction and reignition in the flame front sheet. The challenge of the second set of simulations resides in the capability of predicting a self excited high frequency oscillation and to examine the established numerical database focusing on the possible intrinsic flame unsteadiness, which can be considered responsible for the arising of the instability itself.

In order to successfully perform complex numerical simulations as those just described it is mandatory to resolve a very large spectrum of time and length scales. In fact, combustion instabilities exist because of the interaction between turbulence and combustion and therefore a good resolution of both processes is crucial, i.e. the turbulent cascade shall be properly taken into account and the main chemical kinetic aspects of the combustion process shall be considered by the combustion model. Numerical methods and models, as those used in this work, are able to take into account the above mentioned constraints, but have several drawbacks: so far the experience is confined to research facilities, the development of dedicated boundary conditions is still ongoing and above all the simulations are very expensive from a CPU point of view, so that they can last over many months, also when run on powerful super-computers. Therefore the last question addressed in this work focuses on alternative methods to today's most popular LES and hybrid LES/RANS hybrid methods. The Triple Decomposition Method (TDM) is the one suggested in the following: it is based on a scales separation, which enables to simulate a superposition of a steady state turbulent field and a coherent oscillatory field. This approach, first introduced by Reynolds et al. [75] to filter in his experiments coherent

waves from a turbulent field, has been implemented in the DLR-THETA research CFD code and its capabilities have been verified by means of a simple testcase.

2 Combustion Instabilities

Combustion instabilities are flame-driven unsteady processes, which can finally lead to large amplitude pressure fluctuations; these are very dangerous for the life of combustion devices. Combustion driven oscillations can be encountered whenever a combustion process takes place: in fact they had been a critical issue starting from liquid fuel boosters for space vehicles, as documented by the pioneering work of Crocco et al. [15], down to common domestic furnaces, e.g. [11, 72]. Moreover combustion instabilities represent a challenge also for the proper operation of gas turbine (GT) combustion chambers, [101]. Understanding combustion instabilities and therefore being able of controlling or even avoiding them, is a key issue for the secure and stable operation of any of the above mentioned devices.

As already pointed out in the introduction, chapter 1, this work focuses on combustion instabilities in gas turbines; as a matter of fact in nowadays state-of-the-art GT the combustion process adopted, i.e. lean swirl-stabilized premixed combustion, is very sensitive to disturbances, which can grow into combustion instabilities and finally lead to flashbacks, or cause significant structural damages or induce complete flame blowouts. It is clear that for aeronautical applications such hazards must be avoided for safety reasons, but also for industrial applications combustion instabilities are critical since they can result in long outages due to shutdown/start up procedures, [88] and can reduce the life of the combustor, since they generate strong mechanical stresses and high thermal loads on the combustion chamber components. Both high and low frequency dynamics can be observed in GT.

A precise boundary between low and high frequency instabilities is hard to be named: many authors [32, 57, 39] consider instabilities with characteristic frequencies larger than 1000 Hz to be high frequency instabilities. This border applies well to real GT combustors but can lead to misunderstandings when dealing with research scale-combustors, due to scaling effects. This misinterpretation can be avoided, if a definition based on the Strouhal number, S , is considered and therefore the frequency is normalized by a characteristic velocity and a characteristic length. Thus, a mathematical description can be stated as:

$$S = f_{osc} \cdot \frac{L}{V} \quad (2.0.1)$$

Hence using the burner diameter as the characteristic length and the averaged burner exit velocity as the characteristic velocity, as it was done for example by Paschereit et al., [63, 64], low frequency oscillation are those with Strouhal number less than one, while high frequency oscillations are characterized by Strouhal numbers larger than one.

Furthermore, focusing on GT combustion chambers, in the past years a more intensive research effort has been dedicated to low frequency instabilities than to high frequency instabilities. In fact, as Krebs and coworkers, [39], emphasize, the first natural mode of a GT combustor lays within 50 Hz and 300 Hz and these are consequently the most critical frequencies when dynamics arise in a GT. Thus in the last two decades very intensive studies on the formation and feedback mechanism of low frequency instabilities have been done, while high frequency oscillations have been less investigated. This is also related to another crucial issue, which has been the lack of methods to analyze high frequency processes. Difficulties have been encountered both for experiments and Computational Fluid Dynamics (CFD) studies and just in the recent past reliable approaches to investigate high frequency instability have been made available: for experimental works high repetition rate laser techniques serve the scope well, [9] and for numerical studies the use of Large Eddy Simulation (LES) and/or hybrid methods, e.g., Scale Adaptive Simulation (SAS), in combination with complex combustion models gives good results, [18, 32]. Focusing on the numerical simulation of high frequency instabilities, the main challenge resides in the capability of simulating at the same time a wide range of time and length scales, i.e to achieve a good resolution of the turbulent flow field as well as of the combustion processes, in order to assess the interaction between flame and flow instabilities, furthermore achieving a good numerical description of the processes can be even more complex since in some cases the chemical and physical phenomena are not yet fully understood, [60]. The difficulties, which can be encountered in performing such simulations will be more deeply analyzed in Chapter 4, Section 4.3.

Another method, alternative to the experimental and CFD approaches, which has been intensively used to investigate combustion instabilities is based on the acoustic analysis of the GT combustor. This kind of concept relies on the linear stability analysis and through the linear perturbation of the mathematical description of the system, those frequencies for which the instability grows exponentially in time can be identified. A very high level of complexity can be achieved in this modal analysis by taking into account temperature gradients, geometrical effects, the acoustics from the compressor exit to the turbine entry, etc., as shown by Dowling et al. [21]. Finally the acoustics must be coupled with a flame model in order to assess the response of the combustion process to the disturbance, [29, 13].

The description of the response of the combustion process to instabilities by means of flame transfer functions constitute also the fundamentals of control techniques to eliminate combustion dynamics; passive as well as active control methods can be used and Candel, [12], clearly explains the differences between the two approaches. Passive methods require a deep physical understanding of the phenomenon and afterwards imply operating modification or even geometry redesign of the combustion chamber, thus altering the response of the combustion system to perturbations. Active methods otherwise inject perturbations in the system and change the dynamical response of the system itself. A review of active approaches is given in [20], and include methods based on phase-shifted sound signal generated via loud-speakers in the combustion chamber, as well as direct modulation of the fuel mass flow, [31]. The typical

passive control methods are reviewed by Richards et al. [77], and include changing the average time lag, combining injectors with different dynamic responses and changing the flame location and flame geometry. Moreover Helmholtz resonators are also effective devices to inhibit pressure oscillations in combustion chambers. As explained in [68] these devices are able to dump significantly just one pressure oscillation frequency, in fact they act on the frequency next to their characteristic one and need to be modified whenever the combustion chamber conditions change.

2.1 Fundamentals of Low and High Frequency Combustion Instabilities

As already pointed out in the previous section, in this work the demarcation between low and high frequency combustion instabilities is set by the non-dimensional frequency, i.e. the Strouhal number, such that combustion driven oscillation with Strouhal numbers less than one are considered low frequency instabilities (LFI) and combustion dynamics characterized by Strouhal numbers greater than one are high frequency instabilities (HFI). Nevertheless, low and high frequency combustion instabilities can also be distinguished depending on how they manifest themselves; in the industry it is often referred to "cold tones", "hot tones" and "screech", [81]. Cold tones emerge at very low frequencies, less than 50 Hz, and are distinguished by the amplitude increasing when the flame temperature decreases. In case of hot tones, which can be found in a frequency range between 100 Hz and 300 Hz, the amplitude increases when raising the flame temperature. At frequencies in the order of kHz screech phenomena are observed, which are the most detrimental for the engine parts. Moreover also the acoustic response of the system is different for low and high frequency instabilities: LFI are associated to longitudinal modes whereas HFI couple with radial modes, tangential modes or even mixed modes, [65, 81].

Anyhow, it is commonly accepted that, although combustion instabilities always involve the coupling of the combustion process and of the acoustic pressure field in the combustor, the mechanisms leading to low and high frequency instabilities are different, [39]. In case of low frequency instabilities the most general description on how they arise, which is widely accepted in the research community, states that flow disturbances perturb the far field and consequently produce fluctuations in the rate of reaction, [37]. The consequent oscillation is self-sustained as long the energy variation in the reaction zone and the pressure fluctuation, due both to acoustic and/or convective modes, are in phase. This is stated by the Rayleigh criterion and can be expressed by the mathematical formulation:

$$\int_T p'(t)q'_{th}(t)dt > 0 \quad (2.1.1)$$

where p' is the pressure fluctuation and q'_{th} the heat release rate. The heat release variation is commonly associated to the fluctuation in the fresh mixture composition, [52]; Meier et al.,[51],

remark that oscillating fuel supply in combination with a convective time delay generate the feedback for the self-sustenance of the instability. Moreover, the heat release can vary even if the inlet of the burner is choked and the perturbation cannot be transferred to the fuel/air lines: this so called mixture feed instability, first demonstrated by Janus et al. [35], is due to the effect of acoustic waves traveling between the choked section and the flame front and therefore reducing or increasing the supply rate of fuel/air mixture.

Furthermore, several other mechanisms can be found in the literature as being responsible for low frequency oscillations. In his review publication, Candel, [12], evidences different classes of elementary processes which can drive low frequency oscillations; among others, he addresses unsteady strain effects, the interaction of perturbed flames with boundaries and flame/vortex interactions. In fact, the pairing process of the vortices shed at the dump plane of the combustion chambers is very often considered responsible for the arising of this kind of combustion instabilities: these vortical structures influence the mixing process by entraining fresh mixture and carrying it downstream the combustion zone, therefore realizing unsteady heat release conditions, [63]. This last issue is focus of intensive research, since the phenomenon can also be utilized for achieving more uniform combustion conditions, in fact the motion of these coherent structures can also significantly enhance turbulent mixing, [30], with a positive influence on the emissions.

Moreover, swirl-induced vortex breakdown can also lead to the formation of large scale vortical structures precessing in the combustion chamber, which influence both mixing and combustion. It is commonly accepted that the so-called precessing vortex core interferes with the acoustics of the combustion chamber and consequently thermo-acoustic instabilities arise, [66, 65, 85, 87], still, how precisely the coupling happens is focus of intense ongoing research.

Despite the fact that to date, an extensive and systematic review of high-frequency instabilities, i.e., how they arise and perturb the combustion process, is not known to the author, in the following the main outcomes on the subject are summarized. High frequency oscillations seem not to follow the formation path described above for thermo-acoustic instabilities, [19]; more likely intrinsic combustion instabilities drive these oscillations and acoustic fluctuations arise as a consequence, but are not necessarily involved in the feedback path. Matalon reviewed combustion dynamics driven by intrinsic flame instabilities, i.e. combustion associated unsteadiness which would have arose even if the combustion process would not interact with the surroundings; in case of premix combustion the thermal expansion through the flame front leads to hydrodynamic instabilities, which manifest themselves on a macro-scale with the wrinkling of the flame surface, [49]. Thermo-kinetic instabilities, [19], the influence of pressure on the chemical kinetic properties of the flame, as well as ignition time delay, [15], and/or instabilities due to the interactions of small scale vortices shedding from the shear layer, [65] are also addressed to be responsible of inducing high frequency combustion dynamics.

3 Computational Fluid Dynamics

To achieve the numerical resolution of combustion related phenomena, it is mandatory to know the equations constituting the fundamentals of any computational fluid dynamics (CFD) problem. These equations are the key to understand the physical meaning of the obtained solution, as well as the modeling assumptions, the errors and/or approximations which consequently arise. The CFD governing equations are particular statements of the mass conservation equation, of Newton's force law and of the energy conservation equation. CFD textbooks, e.g. [4], [24], describe how to derive and discretize these equations. Moreover, the following references can be addressed for the specific combustion related fundamental topics: [27], [40], [68].

This chapter has not the ambition of giving a review of the fundamentals of CFD, but just to list the governing equations, which are needed in the following chapters of this publication. An overview of the main approaches for the numerical resolution of turbulent combustion flows is presented, enlightening the key difference between Reynolds Averaged Navier Stokes (RANS) and Large Eddy Simulation (LES).

3.1 The Governing Equations

The governing equations are written in partial differential form and are presented in their conservative expression, i.e., as explained in [4], the equations are derived applying the physical principles to an infinitesimally small fluid element, a control volume, fixed in space. A cartesian coordinate system is chosen. To derive the equations in the most general form, a multicomponent, reactive, compressible flow is considered.

All the conservation equations written in the following sections resume the form of the transport equation of a generic scalar:

$$\underbrace{\frac{\partial(\rho\Phi)}{\partial t}}_A + \underbrace{\frac{\partial(\rho\Phi u_j)}{\partial x_j}}_B + \underbrace{\frac{\partial}{\partial x_j} \left[\Gamma \left(\frac{\partial\Phi}{\partial x_j} \right) \right]}_C + \underbrace{S_\Phi}_D \quad (3.1.1)$$

where term A is the local time variation of the scalar quantity, B the convection of Φ , C the diffusion and D the source term.

3.1.1 The Mass Conservation Equation - Continuity Equation

The continuity equation for the mixture is expressed by:

$$\frac{\partial\rho}{\partial t} + \frac{\partial(\rho u_j)}{\partial x_j} = 0 \quad (3.1.2)$$

For each species in the multiphase mixture a mass conservation equation can be written, equation 3.1.3:

$$\frac{\partial(\rho Y_n)}{\partial t} + \frac{\partial(\rho Y_n u_j)}{\partial x_j} + \frac{\partial j_{nj}}{\partial x_j} = \omega_n \quad (3.1.3)$$

being Y_n the n-th species mass fraction, with $n = 1, 2, \dots, N - 1$ and N is the total number of species in the multicomponent flow. Usually, $N - 1$ transport equations are solved, while the N -th equation is constituted by the conservation of the chemically reacting mixture.

3.1.2 The Momentum Equation - Navier Stokes Equations

The momentum equation is reported in equation 3.1.4, the derivation of the single terms and of the final form of the equation can be found in [40].

$$\frac{\partial(\rho u_i)}{\partial t} + \frac{\partial(\rho u_i u_j)}{\partial x_j} = -\frac{\partial p}{\partial x_i} + \frac{\partial}{\partial x_j} \left[\mu \left(\frac{\partial u_i}{\partial x_j} + \frac{\partial u_j}{\partial x_i} \right) + \lambda \frac{\partial u_k}{\partial x_k} \delta_{ij} \right] + \rho f_i \quad (3.1.4)$$

where $\lambda = -\frac{2}{3}\mu$.

3.1.3 The Energy Conservation Equation

The conservation of energy can be stated by means of different variables, i.e. energy, enthalpy or temperature; in [40] all different forms are reported. To perform the simulations reported in chapters 4 and 6 the commercial ANSYS-CFX code and the research DLR-THETA code have been used; these two codes rely on the formulation of the energy equation by means of the stored energy, equation 3.1.5, and of specific enthalpy, equation 3.1.6, respectively. The stored energy per unit mass is defined as: $e_t = e + \mathbf{u}^2/2$, where e is the specific internal energy. Following [27], it is assumed that in e the energy of formation of the gas phase is included, and therefore in equation 3.1.5 there is no source term for the reactions.

$$\frac{\partial(\rho e_t)}{\partial t} + \frac{\partial}{\partial x_i} (\rho u_i e_t + u_i p) - \frac{\partial(u_j \tau_{ji})}{\partial x_i} + \frac{\partial q_i}{\partial x_i} = \rho u_i f_i + \omega_r \quad (3.1.5)$$

$$\frac{\partial(\rho h)}{\partial t} + \frac{\partial(\rho u_i h)}{\partial x_i} = \frac{Dp}{Dt} - \frac{\partial q_i}{\partial x_i} + \frac{\partial(u_j \tau_{ij})}{\partial x_j} + \rho u_i f_i + \omega_r \quad (3.1.6)$$

being D/Dt the material derivative.

3.2 Turbulent Flows and Turbulent Combustion

Generally turbulence¹ can be described as a chaotic flow regime happening at high Reynolds numbers, i.e. where the inertial forces are predominant and the dissipative effects are very small. In this situation the main variables characterizing the flow fluctuate both in time and

¹For a deeper and more comprehensive description of turbulence and all related problems, mono-thematic books as that of Pope [69] are recommended

space around a mean value and often described mathematically as follows:

$$f = \bar{f} + f' \quad (3.2.1)$$

being f the general variable, \bar{f} its ensemble averaged value and f' the stochastic fluctuation describing the turbulence motion.

The numerical resolution of a non-reactive turbulent flow field implies the solution for all points in the computational domain of the continuity and the momentum conservation equations, 3.1.2 and 3.1.4. The decision of solving directly the above mentioned equations, implies a constraint on the spatial and temporal discretization. Considering exemplarily the spatial discretization, the cell size must be able to capture the kinetic energy dissipation which occurs on the smallest turbulent length scale, i.e. the Kolmogorov length scale:

$$\eta_k = \left(\frac{\nu}{\epsilon}\right)^{\frac{1}{4}} \quad (3.2.2)$$

Thus, as explained by Ferziger and Peric [24], for such a fine resolution the cost of the simulation typically scales with Re_L^3 , where Re_L is the Reynolds number constituted with the velocity fluctuation and the turbulent integral length scale and is normally 0.01 times the macroscopic Reynolds number. Considering that in combustion chambers Reynolds numbers are typically of some hundreds of thousands, it is straightforward to calculate that such a simulation would require roughly milliards of computational points, which is still a prohibitive number even for nowadays high performance clusters. Therefore different techniques have been developed over the years for the solution of turbulent flows, e.g. Reynolds Averaged Navier Stokes (RANS) approach, section 3.2.1, or the Large Eddy Simulation (LES), section 3.2.2.

Performing the computation of a turbulent reactive flow adds new issues to those already described. In fact combustion and turbulence interact with each other [68]: flame can enhance the flow turbulent degree, so called flame generated turbulence, as well as cause a relaminarization of the flow. On the other hand turbulence enhances chemical reactions by increasing the reaction rate, but can also lead to flame quenching and extreme flame wrinkling. In chapter 4 possible strategies are shown to deal with turbulence chemistry interaction in simulations for technically relevant configurations.

3.2.1 Averaged Transport Equations

The RANS approach relies on equation 3.2.1, which is introduced in the governing equations, 3.1.2 to 3.1.6, to obtain a new set of equations. Once the substitution is performed averaged transport equations are obtained, containing new terms, which represent the correlation between the mean and the fluctuating part of the flow. Moreover, when operating with flows with variable density, as it is the case in combustion, mass-weighted average is adopted:

$$\tilde{f} = \frac{\overline{\rho f}}{\bar{\rho}} \quad (3.2.3)$$

When adopting this so called Favre-averaging technique, still each relevant flow variable can be expressed as:

$$f = \tilde{f} + f'' \quad (3.2.4)$$

being \tilde{f} the mass-weighted averaged term and f'' the stochastic fluctuation. Also in this case the substitution of equation 3.2.4 in equations 3.1.2 to 3.1.6 leads to a new set of averaged equations with some additional terms ².

In particular in the momentum conservation equation the so called Reynolds stresses appear, $\overline{\rho u_i'' u_j''}$, which represent the closure problem of turbulence. In fact, these terms are unknown and can be resolved or by deriving new transport equations for each term, and therefore shifting the closure problem at higher order or by direct closure, i.e. by modeling. Typical turbulence models for RANS approach are two equations models, as $k - \epsilon$ [41], $k - \omega$ [100] or a blend of both, the SST- $k - \omega$ [53]. It is necessary to point out that, when adopting this approach no turbulence is resolved; just the averaged field is obtained.

3.2.2 Large Eddy Simulation

The Large Eddy Simulation (LES) approach resolves large, energy containing scales and filters out the smaller ones. The filtering technique can be generally expressed as:

$$\bar{f} = \int_{\Omega} f(y) G(x - y, \Delta) dy \quad (3.2.5)$$

being G the filtering function, Δ the filter width and Ω the computational domain [38]. Spectral space filtering is commonly used and in this case the grid size can be adopted as the filter width.

The filtered governing equations, obtained by introducing equation 3.2.5 in equations 3.1.2 to 3.1.6 have a general form similar to that achieved for the RANS approach, [62]. Therefore, models need to be used to close the turbulent subgrid scales. Anyway, as Poinot and Veynante point out, [68], LES introduces additional information, due to the direct resolution of the larger turbulent scales and allows to adopt similarity assumptions for the smaller scales, which can be considered to behave as larger ones. Nevertheless also models similar to those adopted in RANS simulations, i.e. based on the kinetic energy and its dissipation rate, can be used to model the subgrid scales.

The resolution of a portion of the turbulent cascade allows a better description of the unsteady features of the flow, but is highly expensive in terms of computational demand: a LES simulation can be 100 or even 1000 times more expensive than a normal unsteady RANS simulation, [68]. Therefore, hybrid methods, as the SAS-SST model described and adopted in chapter 4, which combine URANS and LES approaches and enable a sensible reduction of the computational costs gain more and more interest.

²The complete derivation of the equations and their final form is reported in the work of Poinot and Veynante [68].

4 Experiences in Modeling Combustion Instabilities

The scope of this chapter is to analyze low and high frequency oscillations in combustion chamber relevant geometries by means of numerical simulation. Therefore, numerical methods have been adopted, as explained in 4.1, which are a compromise between computational effort, reliability and, for what concerns the combustion process, the capability of reproducing very turbulent flow as well as chemistry-turbulence interaction. Since as already pointed out in chapter 2, low frequency instabilities such as thermo-acoustic oscillations has been the focus of many research work in the past decade, it has been decided, regarding low frequency phenomena to focus this study on very lean conditions, next to lean blow off. For what concerns high frequency instabilities (HFI) the focus of this chapter is on intrinsic combustion phenomena, considered responsible for the arising of high frequent dynamics. In both cases well suited test-cases have been chosen: the gas film nozzle model combustor, section 4.2 is a DLR developed scientific burner, technically relevant for applications beyond research. The choice of a combustion chamber configuration to use as a demonstrator for high frequency instabilities was more problematic. On the one hand not much literature is available, on which we could rely, moreover since HFI develop in small time and space scales, it was clear that we would need fine grid resolution and small time steps, i.e. very high computational requirements. Therefore we needed a simple geometry to minimize the computational domain: the simple can combustor, described in section 4.3, presents a compact geometry and the work of Di Sarli et al. [19] already proved that high frequency instabilities can arise in the device. The limit of the work presented by Di Sarli, et al. resided in the numerical tools used, in fact the simulations were RANS-based, therefore dramatically restricting the possibility of detaching different mechanisms likely responsible for the arising of high frequency combustion instabilities. Some first findings on both numerical studies presented in section 4.2 and 4.3 had already been published in [73] and [74] respectively.

4.1 Numerical Methods

The simulation presented in section 4.2 were performed with the commercial code ANSYS CFX, while for those reported in section 4.3 the in house DLR-THETA code was adopted. The two different codes enabled to assess different problems: while CFX can perform simulations taking into account compressibility effects, the DLR-THETA code provides a very solid chemistry module, able to support a detailed description of the chemistry-related processes. This aspect

becomes crucial when chemistry and turbulence affect each other and finally influence the dynamics of a combustion chamber. In the following a brief description of the codes is given. The models for turbulence and combustion described afterwards are available for both codes, although, due to the intrinsic differences of the two codes, their implementation is not necessarily the same.

4.1.1 ANSYS CFX 11.0 Code

The code is a commercial general purpose CFD code. The set of governing equations, in their fully compressible formulation, are discretized with a finite-volume, Favre-average approach and second order accuracy in both time and space can be achieved. The linearized equations are solved in coupled manner with multi-grid techniques and the solution can be obtained on both structured and unstructured computational grids. From a computational point of view, very expensive simulations can be run efficiently thanks to parallel calculations, based on domain decomposition techniques, which can be performed on a multitude of processing cores simultaneously, [28]. Moreover, the user can choose among a large number of turbulence and combustion models.

4.1.2 DLR-THETA Code

DLR-THETA is a research CFD code developed at the Institute for Combustion Technology in Stuttgart,[3]. Over the years the code has been optimized to simulate reactive flows in complex geometries at low Mach number. The discretization of the governing equations is accomplished in a finite volume, vertex centered manner, obtaining an accuracy of second order in both time and space. The discretized equations are solved sequentially, for the pressure equation a multi-grid approach can be adopted to enhance convergence. The solution of the chemistry module, i.e. species and enthalpy equations, is obtained with a coupled method to overcome numerical stiffness. Two different solution strategies can be chosen for the coupling of the pressure and velocity fields, the SIMPLE algorithm [67] or the projection scheme [14]. Several models for turbulence, both for high and low Reynolds numbers, and for combustion are available.

4.1.3 Shear Stress Transport - Scale Adaptive Simulation Model

The SST-SAS model is based on the two equation SST model. This model blends between a $k-\epsilon$ and a $k-\omega$ formulation for the turbulence closure depending on whether the computational cell is located in the near wall region or not. In the SAS model, the von Karman length scale is added within the turbulence length scale equation, thus the model changes dynamically from a URANS to a LES resolution scheme. This means that no explicit grid information is required, but still the model is able to partially resolve the turbulent spectrum [54], [55]. The equations for the model can be written by means of turbulent kinetic energy, k , and turbulent eddy frequency, ω , as follows:

$$\frac{\partial \rho k}{\partial t} + \frac{\partial U_j \rho k}{\partial x_j} = P_k - c_\mu^{\frac{3}{4}} \rho \frac{k^2}{\Phi} + \frac{\partial}{\partial x_j} \left(\frac{\mu_t}{\sigma_k} \frac{\partial k}{\partial x_j} \right) \quad (4.1.1)$$

$$\begin{aligned} \frac{\partial \rho \omega}{\partial t} + \frac{\partial U_j \rho \omega}{\partial x_j} = & \alpha \rho S^2 - \beta \rho \omega^2 + \frac{\partial}{\partial x_j} \left(\frac{\mu_t}{\sigma_\omega} \frac{\partial \omega}{\partial x_j} \right) \\ & + \frac{2\rho}{\sigma_\Phi} \left(\frac{1}{\omega} \frac{\partial k}{\partial x_j} \frac{\partial \omega}{\partial x_j} \right) + F_{SST-SAS} \\ & + \left[\frac{\rho \omega}{k} \frac{\partial}{\partial x_j} \left(\frac{\nu_t}{\sigma_\omega} \frac{\partial k}{\partial x_j} \right) \left(\frac{1}{\sigma_k} - \frac{1}{\sigma_\Phi} \right) \right] \end{aligned} \quad (4.1.2)$$

where P_k is the production rate of the turbulent kinetic energy, Φ is defined as:

$$\Phi = \frac{1}{c_\mu^{\frac{3}{4}}} \frac{k}{\omega} \quad (4.1.3)$$

S is the absolute value of the strain rate and

$$\begin{aligned} F_{SST-SAS} = & \rho \cdot F_{SAS} \cdot \\ & \max \left[\tilde{\zeta}_2 \mathbf{k} S^2 \frac{L}{L_{vK}} - \frac{2}{\sigma_\Phi} k \cdot \max \left(\frac{1}{\omega^2} \frac{\partial \omega}{\partial x_j} \frac{\partial \omega}{\partial x_j}, \frac{1}{k^2} \frac{\partial k}{\partial x_j} \frac{\partial k}{\partial x_j} \right), 0 \right] \end{aligned} \quad (4.1.4)$$

The constant standard values are reported in Table 4.1:

Table 4.1: Constant standard values for the SST-SAS model

c_μ	σ_k	σ_ω	σ_Φ	F_{SAS}	\mathbf{k}	$\tilde{\zeta}_2$
0.09	2/3	2/3	2/3	1.25	0.41	1.755

The von Karman length scale is defined by

$$L_{vK} = k \left| \frac{\frac{\partial U}{\partial y}}{\frac{\partial^2 U}{\partial y^2}} \right| \quad (4.1.5)$$

and L is

$$L = \frac{\sqrt{k}}{c_\mu^2 \omega} \quad (4.1.6)$$

4.1.4 Eddy Dissipation Model

The Eddy Dissipation Model (EDM) relies on the assumption that reactions take place only when reactants are mixed at molecular level and that the reaction rate is controlled by the mixing time rather than the chemical kinetic time [48]. Thus the rate of consumption of the fuel or oxidant is proportional to the turbulent kinetic energy and the turbulent length scale, or turbulent dissipation rate. Therefore, if the reaction rate is limited by reactants, the elementary

reaction rate of progress for a reaction s , R_s , can be written as follows:

$$R_{sEDM} = A \frac{\epsilon}{k} \min \left(\frac{[I]}{\nu_{sI}'} \right) \quad (4.1.7)$$

A is a constant value, $[I]$ the concentration of the species I , and ν_{sI}' the exponent of species I for the reactant side. If the products limiter is preferred, the equation results:

$$R_{sEDM} = AB \frac{\epsilon}{k} \left(\frac{\sum_P [I] W_I}{\sum_P \nu_{sI}'' W_I} \right) \quad (4.1.8)$$

being A and B constant values, W_I the molecular weight of species I and ν_{sI}'' the exponent of species I for the products side.

The assumption made for the EDM no longer holds true when one chemistry time scale becomes relevant. However, the limits of application of the EDM can be extended by combining it with the Finite Rate Chemistry (FRC) model, in which the reaction rates are calculated by means of a chemical kinetic mechanism:

$$R_{sFRC} = F_s \prod_{I=X_1, X_2, \dots}^{N_s} [I]^{\nu_{sI}'} - B_s \prod_{I=X_1, X_2, \dots}^{N_s} [I]^{\nu_{sI}''} \quad (4.1.9)$$

F_s and B_s are the forward and backward rate constants, which are calculated through an Arrhenius like expression. According to the local conditions, the overall model (EDM-FRC) switches between the reaction rates calculated with the EDC or the FRC model. Although the boundaries of applicability of the EDM model are clearly expanded by adding FRC effects, there is still a clear limit to the model due to the very simple chemical kinetics schemes which can be adopted in this context. Normally the schemes which are supported in this numerical technique are single step global reaction schemes.

4.2 Low Frequency Instabilities

In this section the behavior of a combustion chamber operated at very lean conditions next to the lean blow off limit is analyzed. The dynamics at low frequency which are successfully simulated in this section are due to several different phenomena: a thermo-acoustic oscillation can be identified, as well as oscillations which are related to the flame conditions near the lean extinction limit; the latest are the focus of this analysis.

4.2.1 Experimental Test-Case Description

The burner, adopted for many prior research works and for the present numerical investigation, is a laboratory scaled burner developed at DLR. Figure 4.2.1 shows a schematic drawing of the gas film nozzle model combustor; air at room temperature is fed from a plenum in the combustion chamber through two concentric swirlers, which generate a co-rotating flow. The central and annular air nozzle have 8 and 12 channels respectively. The burner could be operated with gaseous fuel, in this case pure methane, which is injected in the chamber from

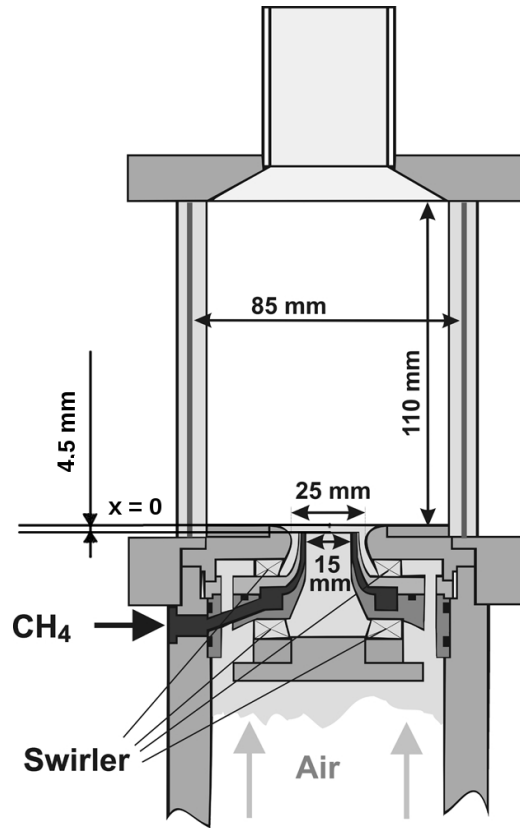


Figure 4.2.1: Schematic drawing of the DLR gas turbine model combustor.[95]

72 channels forming a ring between the two air swirlers. The non-swirling supply channels of fuel and the central air swirler are positioned 4.5 millimeters below the annular swirler. The latter is positioned at the height of the combustion chamber dump plane and is considered as the reference height for the chamber, $x = 0$ mm. The combustion chamber has a square cross section of 85 x 85 mm and is 110 mm long, it ends in a conical contraction followed by an exhaust tube of 40 mm diameter. It was equipped with quartz walls to enable non-intrusive experimental measurements, which constitute the reference dataset for the numerical analysis performed in this work. Further information about the construction of the model combustor and the measurements techniques applied can be found in the following works: [50], [94], [80], [88].

Among other operational points, a very lean methane air flame near blow off, which is numerically analyzed in this section, was extensively investigated in the following experiments: [95], [50], [86], [87], [22]. The thermal power was 7.4 kW, the overall mixture fraction was 0.031 and the global equivalence ratio ϕ was 0.55. This value is very close to the measured extinction limit of 0.53, reported in [22]. The main experimental settings for the flame conditions are summarized in table 4.2 and have also been adopted for the numerical simulation.

4.2.2 Numerical Set-Up

Scope of the numerical investigation was to get a better insight in the phenomena taking place at conditions next to lean blow out (LBO). Therefore, it was important to chose a test-case with

Table 4.2: DLR gas turbine model combustor: experimental flame parameters.

Air [g/min]	CH ₄ [g/min]	P _{th} [kW]	ϕ_{glob} -	f _{glob} -
281	9.0	7.4	0.55	0.031

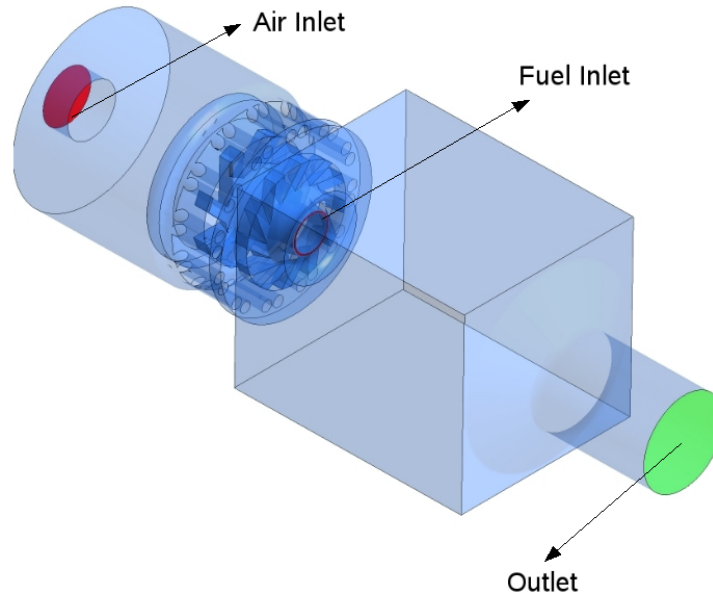


Figure 4.2.2: Model combustor: computational domain.

a broad and reliable experimental database and to adopt numerical models which had already been proven to lead to high quality results in other numerical investigations, [98, 99, 73].

The numerical set-up, which recollected the experimental configuration described in the previous section, stemmed from the numerical work of Widenhorn, et al., [98, 99]. The computational domain employed is shown in figure 4.2.2: plenum, swirlers, combustion chamber and exhaust tube are included. For meshing such a large domain 1.9 million grid points were necessary. The combustion chamber and the nozzle were meshed with an unstructured hexaheder grid with 1.6 million grid points. The plenum was meshed with an unstructured tetrahedral mesh with 0.3 million grid points. Particular attention was dedicated to local refinements in regions of potentially high turbulence generation and large velocity gradients. On the other side, the large computational domain chosen enabled to adopt boundary conditions derived directly from experimental data. Mass boundary conditions for fuel and air inlets were set, accordingly to table 4.2. The global equivalence ratio had therefore the desired value of 0.55. Air and methane entered the combustion chamber at 330 K. At the outlet, a static pressure boundary condition was set. The plenum wall temperature was 330 K and the swirler walls were considered adiabatic. For the combustion chamber dump plane isothermal boundary conditions at 500 K were imposed.

Table 4.3: DLR gas turbine model combustor: performed simulations.

Testcase	Features	Combustion Chamber Wall Temperature	Combustion Modeling
Case A	Baseline	1050 [K]	EMD with FRC Chemistry Nicols, et al.
Case B	Low Wall Temperature	800 [K]	EMD with FRC Chemistry Nicols, et al.
Case C	Modified FRC	800 [K]	EMD with FRC Modified Reaction Scheme

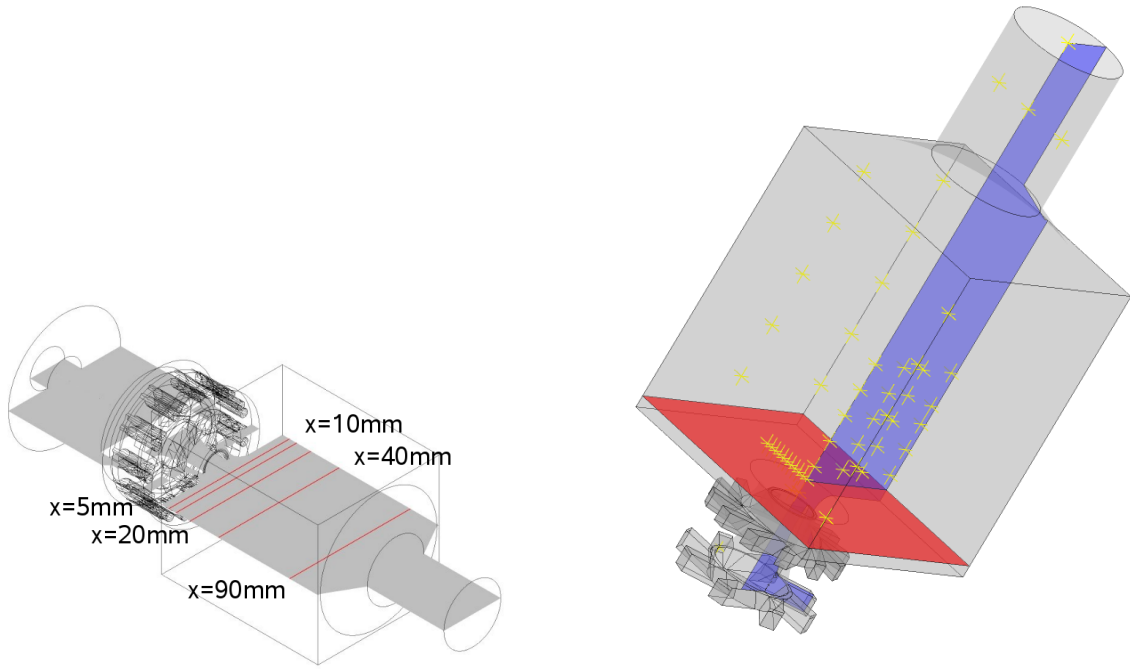
In the baseline set up, case A in table 4.3, the temperature of the combustor walls was set to 1050 K. This value constituted an uncertainty in the simulation. In fact, the value was chosen to be consistent with measurements from other operational points and therefore, a second simulation with lower wall temperature, case B, investigated the impact of this parameter. The isothermal combustion chamber walls were kept at 800 K for case C, too.

The combustion process was modeled by means of an eddy dissipation approach. Knowing from previous studies, [99], that chemical kinetics effects played a distinctive role in the flame dynamics of this model combustor a finite rate chemistry module was added to enhance the EDC performances, see section 4.1.4. For cases A and B, the FRC model relied on a three step global reaction model with a CO subset [59]. Finally, the third simulation performed, case C, addressed the issues related to the influence of the chosen chemical kinetic mechanism: the three step mechanism used in cases A and B for the FRC module was adapted with regards to the laminar flame velocity.

Turbulence modeling was assessed with a hybrid LES/RANS model, the SAS-SST model described in section 4.1. The main advantages of the model are to solve a large turbulent spectrum in the regions of interest and meanwhile to allow the use of RANS typical boundary conditions and to reduce the computational time, compared to pure LES.

The time step for all simulations was set to $2.5 \cdot 10^{-05}$ seconds. The selected time step, dependent on the required resolution needed for the combustion dynamics, is moreover limited to small values in order to achieve a Courant number around one and below in the whole computational domain, which is beneficial for the correct resolution of the turbulence field, [92].

The computations were run with the commercial CFD-program ANSYS-CFX 11. To solve the CFD governing equations for reactive flows a fully implicit scheme was chosen. The discretization of convection and diffusion terms was second order, except for the species and energy equations for which the High Resolution scheme was adopted. This latest scheme adopts a bounded, upwind-based, second order discretization, as described in [2, 6]. Time discretization



(a) Section and lines for evaluation purposes (b) Evaluation planes and monitor points, surface A is colored in blue, surface B in red

Figure 4.2.3: Postprocessing equipment.

was second order, too. A domain parallelization enabled to run the simulations on a multi-processor supercomputer. All computations were run on 20 AMD Opteron processors. Not just the number of CPUs was the same for all simulations, but also the methodology adopted to achieve the converged solution: after a transient phase, averaging was started and continued for a simulation time necessary to obtain converged time-averaged and RMS values. In particular, case A was initialized with a steady RANS simulation, the transient phase was successfully concluded after two combustion chamber residence times, estimated by means of the mean axial velocity,[44]; the averaging phase lasted over four residence times. The total simulated time was 0.7 seconds. The total CPU time for the whole simulation was of 2115 hours. Cases B and C were initialized with the converged solution of case A, and for both cases a transient phase of one residence time was sufficient. The averaging phase for case B lasted over two residence times, achieving a total simulated time of 0.43 seconds with a computational cost of 1450 hours. The averaging phase for case C was of 2.5 residence times, for a total simulated time of 0.45 seconds and required 2050 hours.

4.2.3 Results

Figure 4.2.3a shows the central cross-section, at which the time-averaged and instantaneous results are presented, as well as the different axial positions, at which the profiles of velocity, temperature, mass fraction and mixture fraction have been extracted. Figure 4.2.3b shows further positions relevant for the evaluation of the numerical results. The computational field was

equipped with monitor points, yellow stars in figure 4.2.3b, situated at the chamber wall, these resembles the position at which microphones had been placed to gather the experimental data; further monitoring points are set in the flame sheet averaged position from preliminary RANS simulations. Moreover the blue and the red planes were used for providing result samplings at a very high repetition rate, i.e. 8000 Hz, corresponding to a sample each 5 time steps.

Parts of the findings presented in the following for case A have been published by Rebosio, et al. in [73].

4.2.3.1 Time-Averaged Quantities

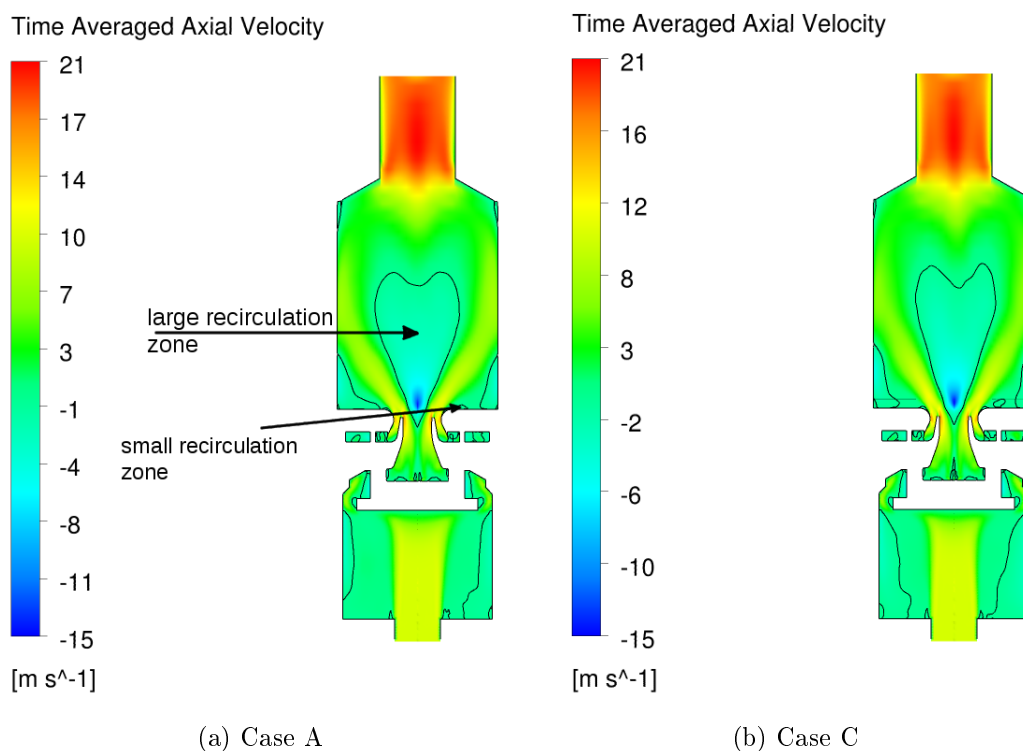


Figure 4.2.4: Time-averaged axial velocity field, $[m/s]$.

The three test cases did not reveal substantial differences in the flow field configuration: in particular cases A and B presented no significant modifications concerning the time-averaged flow field characteristics, while case C indicated a slight overall improvement in comparison to cases A and B. Figure 4.2.4 shows the time-averaged axial velocity fields for cases A and C, the black line denotes the zero velocity isoline and supports a quick visualization of the main flow features, characteristic of swirled flows. All cases captured a large central recirculation zone (CRZ), the outer recirculation zone (ORZ). Small recirculation zones could be observed at the combustion chamber inlet and are due to the unstable separation point of the flow forming the outer shear layer. In fact, due to the curvature in the geometry of the swirler when entering into the combustion chamber, the separation point is fluctuating back and forth, forced by the local fluctuation of the pressure gradient. The experiments, [95], measured that the CRZ extends

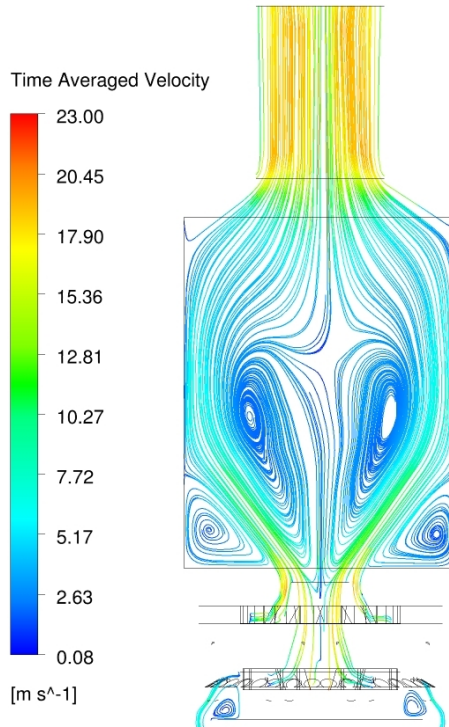


Figure 4.2.5: Baseline testcase. Streaklines plot of the time-averaged velocity field, in $[m/s]$.

in the combustion chamber till the height of $x = 73$ mm. Case A reproduced the extension of the IRZ perfectly, while for case C the value was underestimated by circa 10%, due to the slightly stronger contraction along the combustion chamber axis of the IRZ. Moreover, as it can be noticed from figure 4.2.4, both cases reveal a strong negative axial velocity directly at the inlet; this was due to the fact that the CRZ penetrates upstream the combustion chamber inlet, as the analysis of the streakline plot of the time-averaged velocity field confirms, figure 4.2.5. The reason for this is that the vortex breakdown in all three examined numerical simulations happened already inside the nozzle, as it was already observed in [91] for a similar very lean configuration.

Furthermore, the radial profiles of the time-averaged axial velocity components extracted 10 mm above the combustion chamber inlet, figure 4.2.6a, reveal that case C, red lines, overestimates the negative axial velocity on the axis in comparison to case A by approximately 5%, green line, and to the experimental data, blue dots. Then again, case C captures the intensity of the flow between the inner and outer shear layers better, figure 4.2.6a, and also the shape of the ORZ is better reproduced from the profiles extracted for case C, figures 4.2.6a, 4.2.6c and 4.2.6e. All testcases show the right penetration of the ORZ in the chamber: at $x = 40$ mm, the ORZ is not present anymore, figure 4.2.7. Due to the contraction of the chamber into the exhaust tube a peak of velocity was registered next to the outlet in the experiments, blue dots in figure 4.2.8a, which is very well reproduced for all testcases. Generally, the time averaged characteristics of the flow field were very well captured by all numerical simulations.

Analyzing the time-averaged temperature profiles for case A, Fig. 4.2.9, it can be shown that temperature is overestimated from the flame root, $x = 10$ mm, all along the chamber, $x =$

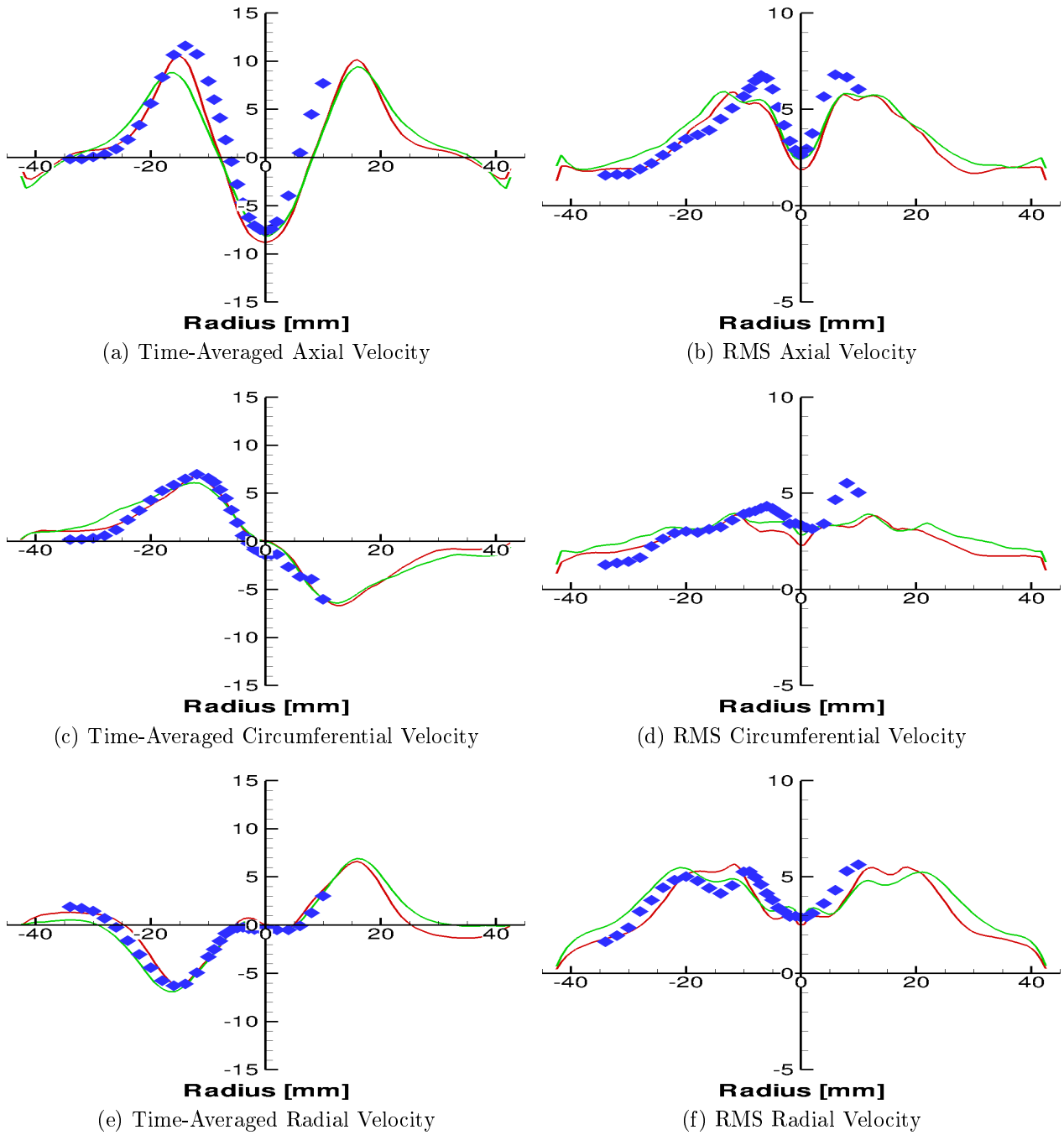


Figure 4.2.6: Baseline testcase. Radial profiles of time-averaged and RMS velocities in $[m/s]$ on line $x = 10mm$. The green lines indicate case A, the red lines case C and the blue dots the experiment.

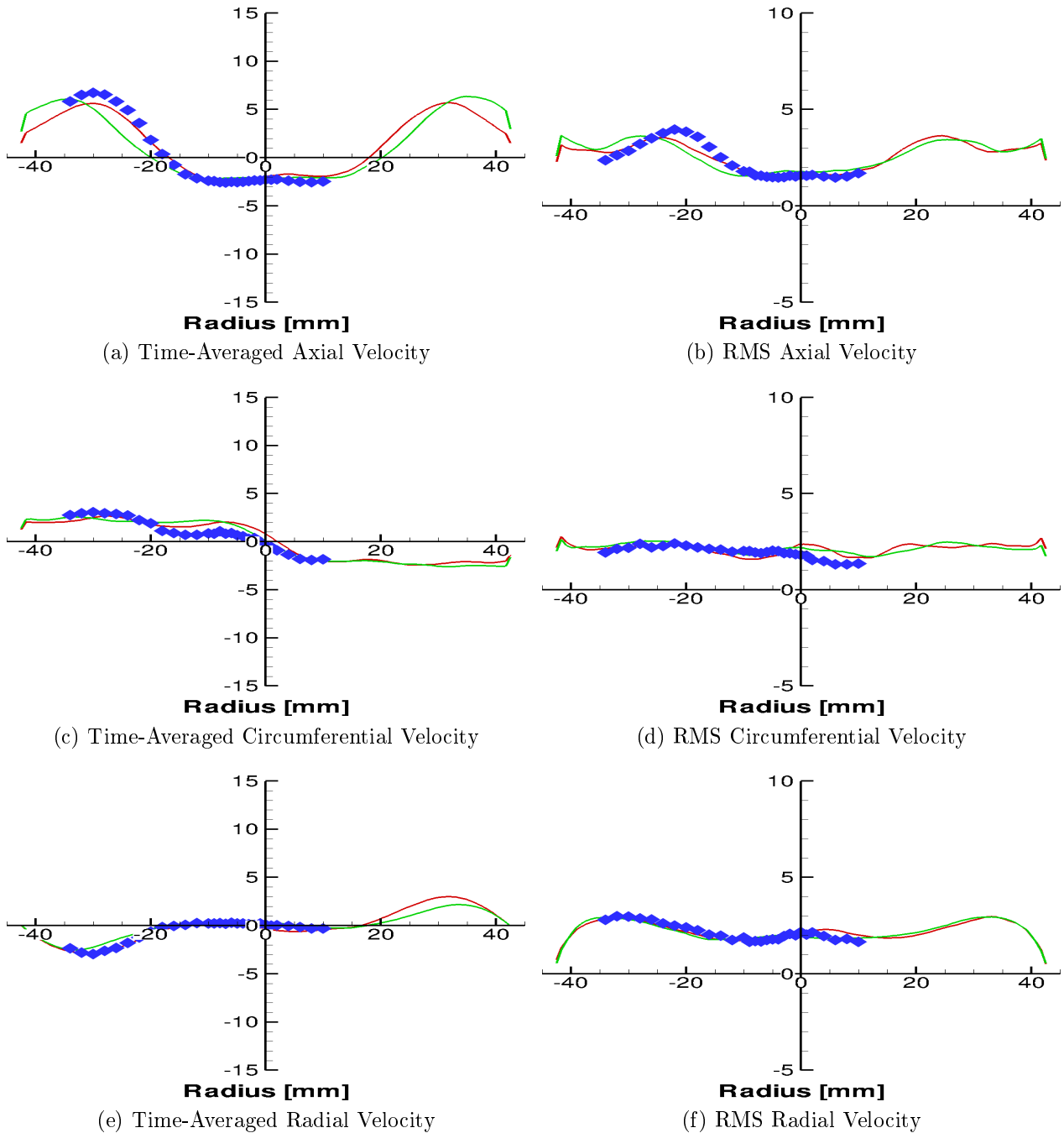


Figure 4.2.7: Baseline testcase. Radial profiles of time-averaged and RMS velocities in $[m/s]$ on line $x = 40mm$. The green lines indicate case A, the red lines case C and the blue dots the experiment.

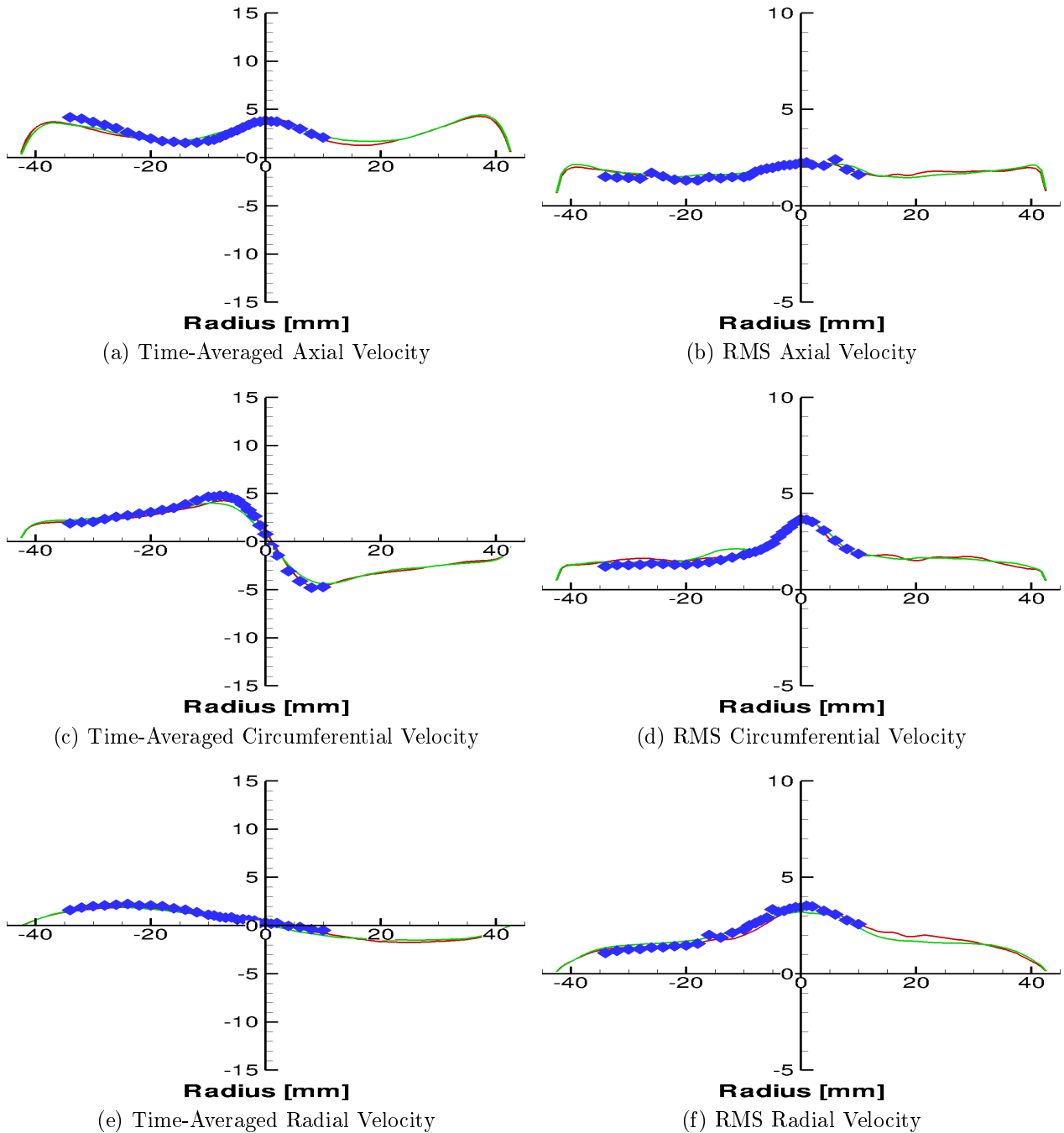


Figure 4.2.8: Baseline testcase. Radial profiles of time-averaged and RMS velocities in $[m/s]$ on line $x = 90mm$. The green lines indicate case A, the red lines case C and the blue dots the experiment.

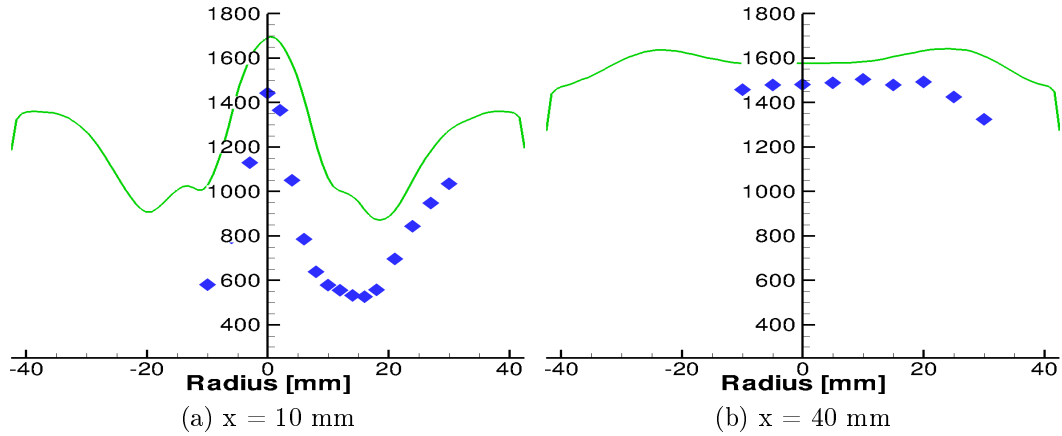


Figure 4.2.9: Time-averaged temperature profiles in $[K]$, from the baseline simulation (green line) against experiments (blue dots).

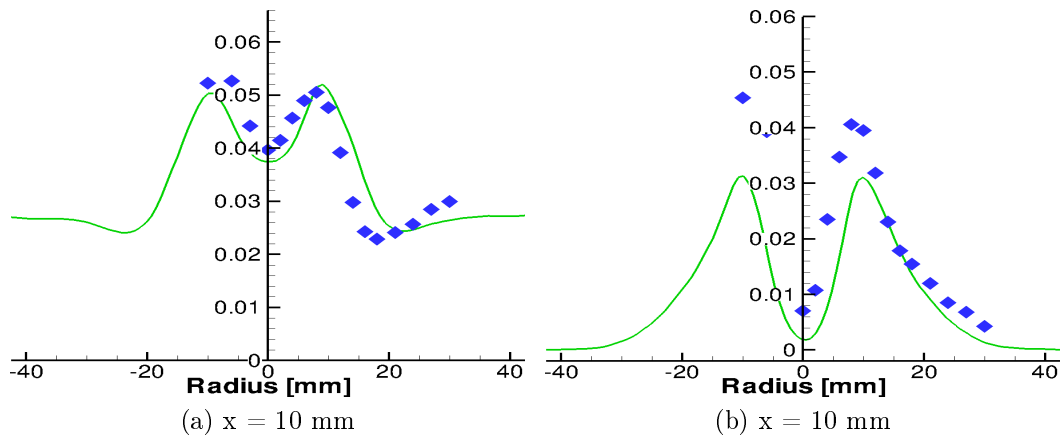


Figure 4.2.10: Time-averaged profiles of mixture fraction and methane mass fraction from the baseline simulation (green line) against experiments (blue dots).

40 mm. Considering the respective profile of methane mass fraction at 10 mm, Fig. 4.2.10b, it is clear that combustion started much closer to the nozzle exit than observed in the experiment and the flame lift off, which Weigand et al. [95] measured being of some millimeters, was not statistically well reproduced in the simulation for case A. Since the mixing process was well replicated in the simulation, as can be seen by comparing the calculated mixture fraction from case A with the values from the experiments, Fig. 4.2.10a, the deficiencies of the numerical solution could be due to the chemical kinetic model adopted. It furthermore was considered that the prescribed temperature at the combustor walls might be too high as well. The numerical simulations of cases B and C focused on these two uncertainties, see table 4.3.

From the results of case B it became clear that a too high prescribed temperature at the combustor walls did not affect the combustion process at the flame root, so that the flame is still too close to the burner exit, Fig. 4.2.11a and the temperature profile in the axial region is almost unchanged. On the other hand a modification of the exhaust temperature can be noticed in Fig. 4.2.11b; in this picture the scale is set to the range of the temperatures of

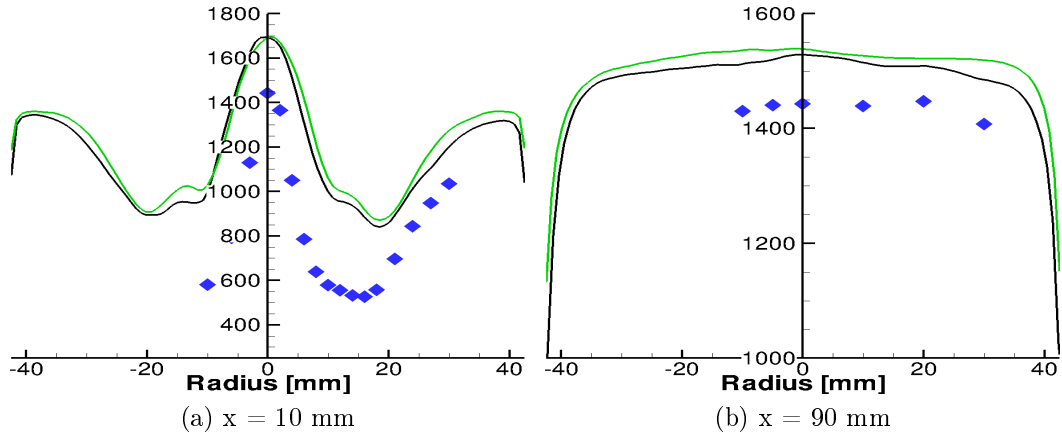


Figure 4.2.11: Time-averaged temperature profiles in [K] from case A (green line), case B (black line) against experiments (blue dots).

the hot products and shows that the temperature is reduced by circa 100 K. This effect could be explained by looking closely at the combustion model behavior: figure 4.2.12 shows in red the zone of the combustion chamber where the reaction rate is calculated by means of the eddy dissipation concept and in blue the zone where it is calculated by means of the finite rate chemistry module. The flame root zone is mainly controlled by chemical kinetics effects, so that the wall temperature modification can barely alter this process, since it has no direct impact on the calculated temperature in the flame root zone.

The simulation reported by case C investigated the possible improvements in the simulation due to chemical kinetics effects. Since using very large reaction models would lead to a too high computational effort, the analysis of the chemistry effects was performed by tuning the available mechanism of Nicols et al. [59]. The flame of the model combustor can be considered as a technically premixed flame: as already pointed out when describing the geometry of the gas film nozzle model combustor, the fuel admission holes are positioned between the inner and outer swirler, and retrieved from the dump plane of the chamber, so that fuel and air can premix to a certain extent before arriving in the primary reaction zone. It therefore can be estimated that the flame anchoring point is mainly controlled by means of turbulent flame velocity, and consequently the mechanism must predict the laminar flame velocity properly. The reference laminar flame velocity, [25], was calculated with Cantera [1] for a premixed mixture with ϕ 0.55 in one-dimension adopting GRI 3.0 mechanism, [83] and was three times smaller than the one predicted with the mechanism of Nicols, et al., indicating that as expected the reaction rate was overestimated in cases A and B. The Arrhenius-like pre-exponential factor for the first step of the mechanism of Nicols et al. [59] was therefore readjusted so that the laminar flame velocity was properly predicted.

Close to the combustion chamber inlet, case C reveals better profiles for the time averaged temperature as well as for the RMS values of temperature, figure 4.2.13a and 4.2.13b. The comparison from experiments and simulations shows also for the time averaged profile of methane mass fraction, figure 4.2.13c better results for case C than for case A. On the other hand, the

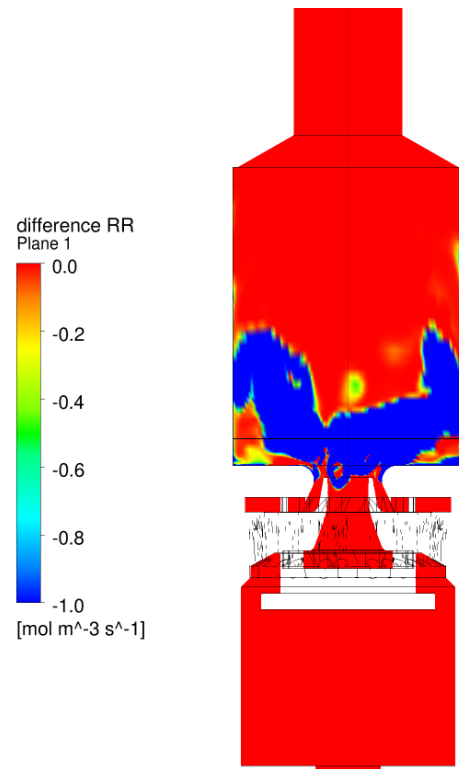


Figure 4.2.12: Case B: Simulation zones where EDM and FRC are active. The red zones are the EDM controlled zones, while the blue zones are FRC controlled.

mixture fraction, figure 4.2.13d, which mainly depends on the turbulent mixing is not particularly influenced. The same improvements could be shown at all heights in the combustion chamber, exemplarily the radial profiles at 20 mm are reported in figure 4.2.14. The profiles also evidence that the time-averaged temperature in the middle of the combustion chamber is still overestimated but it is to expect that a more complex chemical kinetics model could improve it and stabilize the flame more upstream.

The negative axial velocities along the centerline, already shown in figure 4.2.6a, enhanced the recirculation of hot exhaust gases and the mixing in the lower part of the combustion chamber, this produced a quite short “V”-shaped flame for all the performed simulations. In Figure 4.2.15 the flame shape of cases A and C is confronted by means of the reaction rate of the first step of the chemical kinetic mechanism. In case C the flame is more stretched and the V-shaped flame contracts more toward the centerline of the chamber, as expected from the experimental results. Though, as already suggested by the time-averaged temperature profiles the flame root is still anchored at the inner center body and does not provide the proper lift off. It will be shown in the next section that this behavior influences also the capability of capturing a complete flame blow off. Moreover, the area over which combustion takes place is quite large for all cases. This was due to the highly unsteady character of the flame, which will be considered in the following section, too.

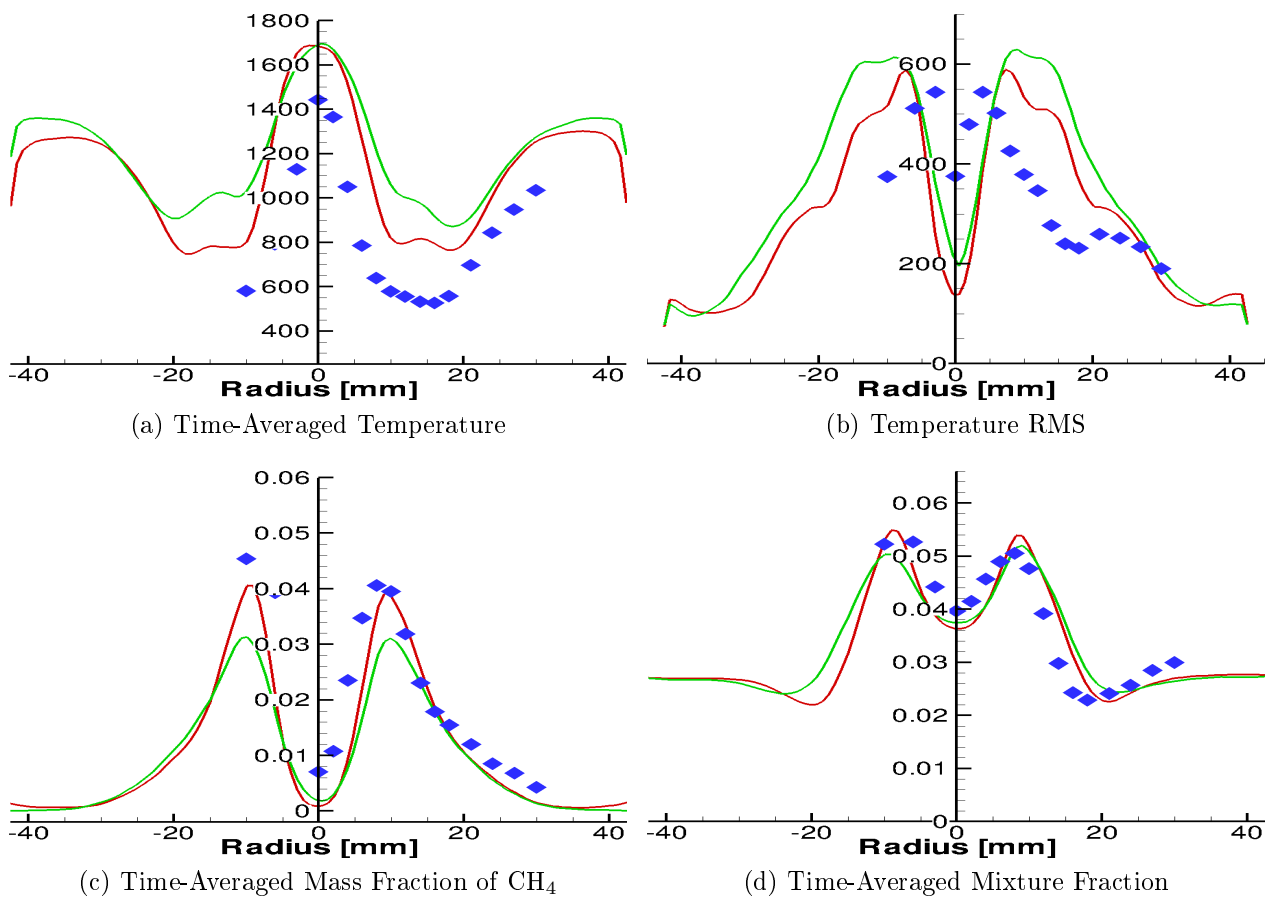


Figure 4.2.13: Baseline testcase. Radial profiles at $x = 10\text{mm}$ for time-averaged, RMS temperature in $[K]$, mass fraction of CH_4 and mixture fraction. The green lines indicate case A, the red lines case C and the blue dots the experiment.

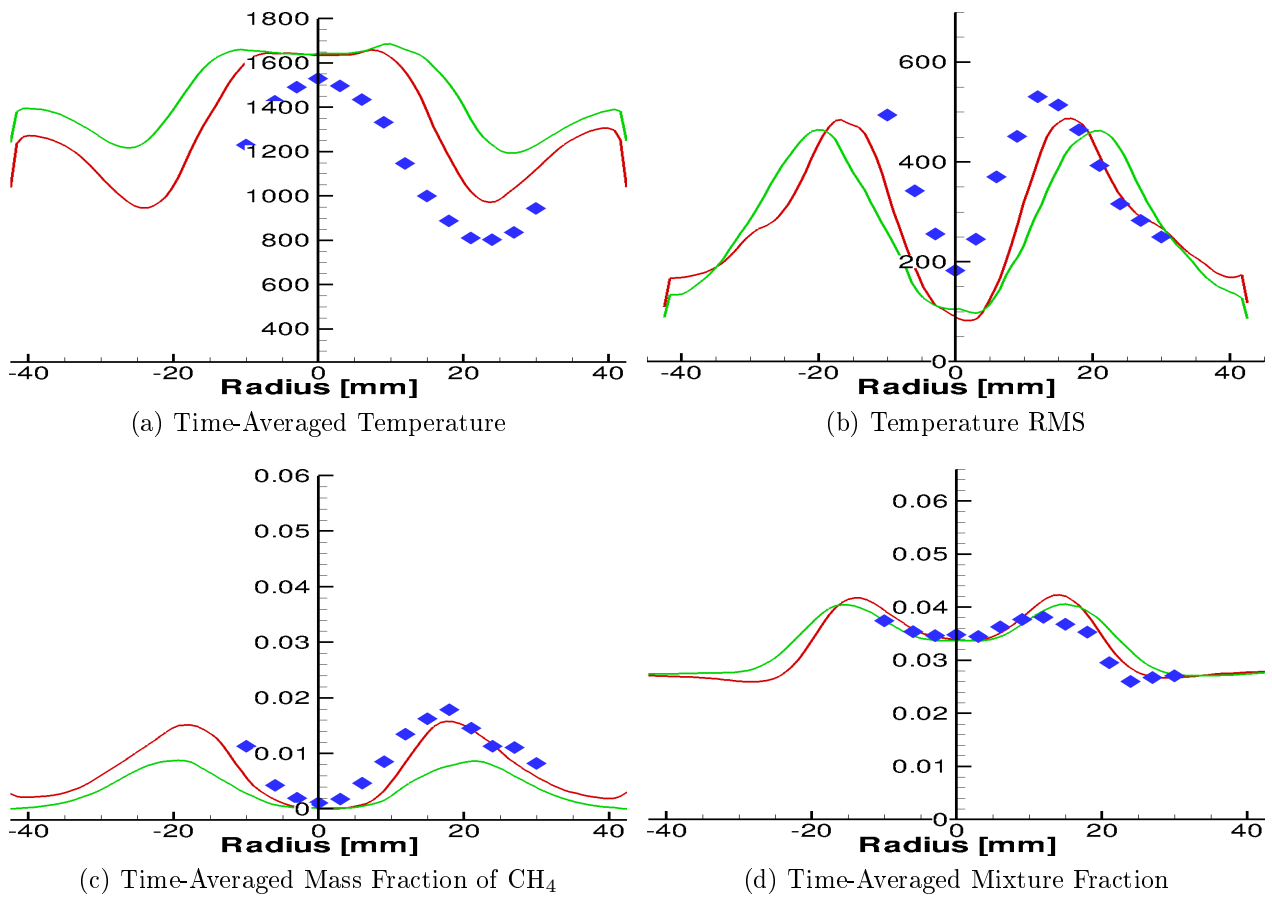


Figure 4.2.14: Baseline testcase. Radial profiles at $x = 20\text{mm}$ for time-averaged, RMS temperature in [K], mass fraction of CH_4 and mixture fraction. The green lines indicate case A, the red lines case C and the blue dots the experiment.

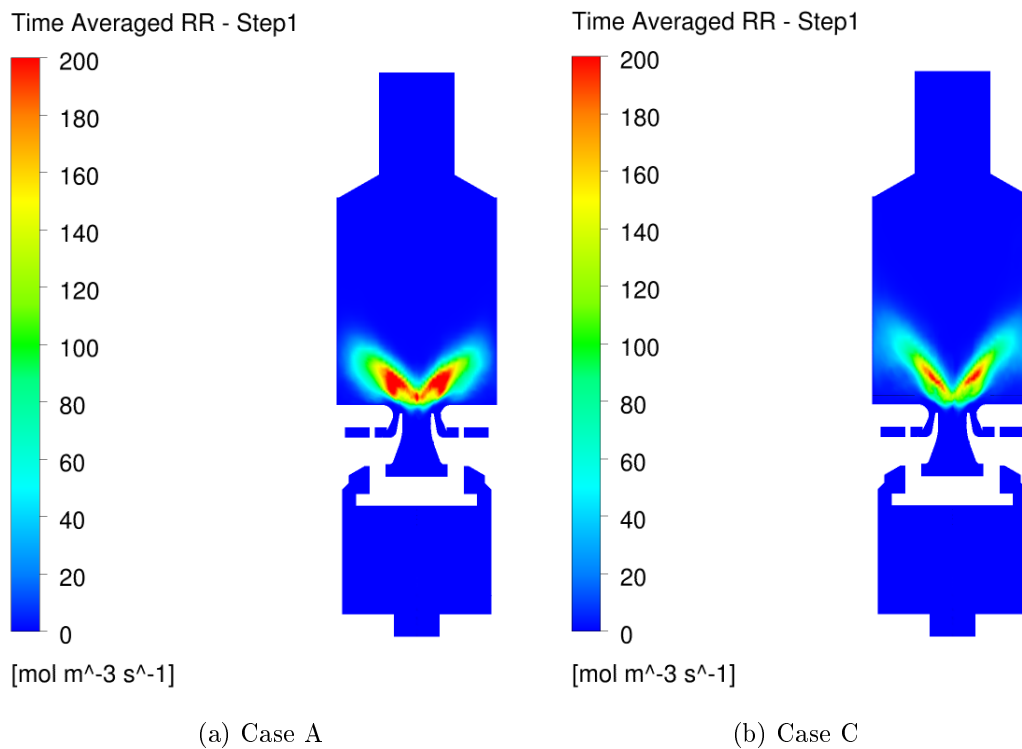


Figure 4.2.15: Time-averaged reaction rate for CH₄ equation, [mol/(cm³s)].

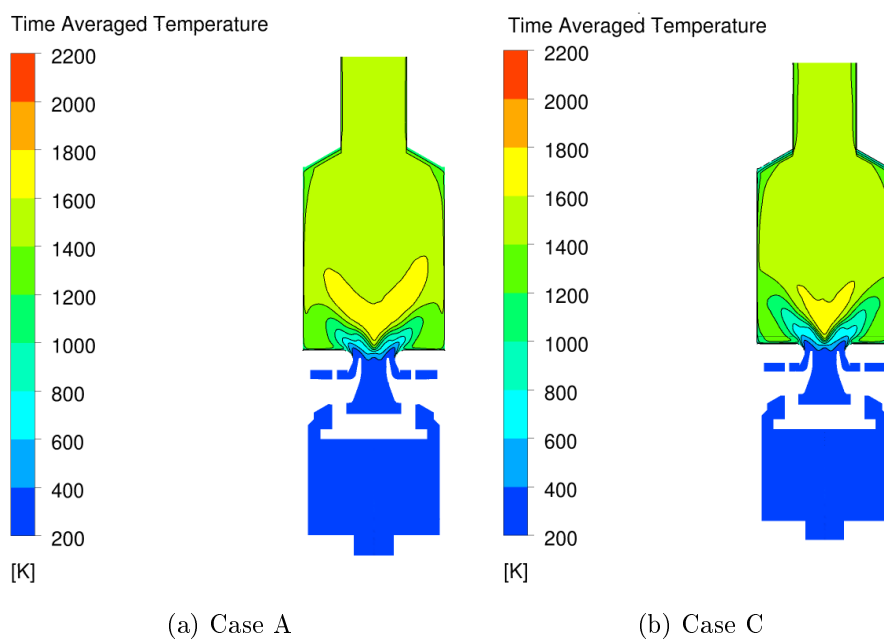


Figure 4.2.16: Contour plot of time-averaged temperature in *K*.

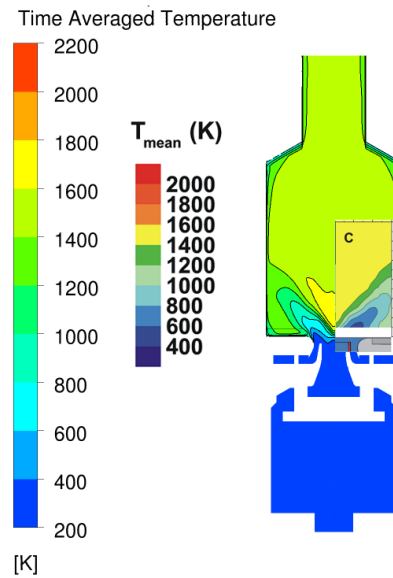


Figure 4.2.17: Case C: Contour plot of time-averaged temperature in [K], overlapped with experimental contour plots.

Finally comparing the contour plots of the time-averaged temperature for cases A and C, figure 4.2.16, it is interesting to notice that the central zone at higher temperature is smaller in case C than in case A.

4.2.3.2 Instantaneous Quantities

Combustion instabilities are the main focus of this chapter; specifically, the numerical studies presented in this section and in section 4.3, want to prove that advanced numerical methods can reproduce low and high frequency oscillations, as well as highly unsteady features as those typical of conditions next to LBO.

While discussing the time-averaged results for the gas film nozzle model combustor, it has been pointed out that, among the different numerical set-up reported in table 4.3, case C achieved the best results; therefore, this section focuses on the unsteady features examined for case C. Still, it is important to clarify that already the analysis of the unstable behavior for case A, which is reported in detail in [73], highlighted some of the phenomena presented in the following, but generally case C showed a better description of the combustor dynamics.

The instantaneous picture of streaklines colored by the velocity magnitude, presented in figure 4.2.18, resembles the time-averaged characteristics described in figure 4.2.5 and adds further crucial information. The injected flow from the nozzle is still clearly visible and reproduces the V-shape discussed in the previous section. However, the flow field is highly wrinkled: vortical structures align along the inner shear layer (ISL) and are present in the outer recirculation zone (ORZ), too. Furthermore, the vortices positioned along the ISL, follow a helical pattern, as evidenced by the black segmented line in figure 4.2.18. The same structure is shown in its three dimensional development in figure 4.2.19, by means of a pressure iso-surface, colored by axial

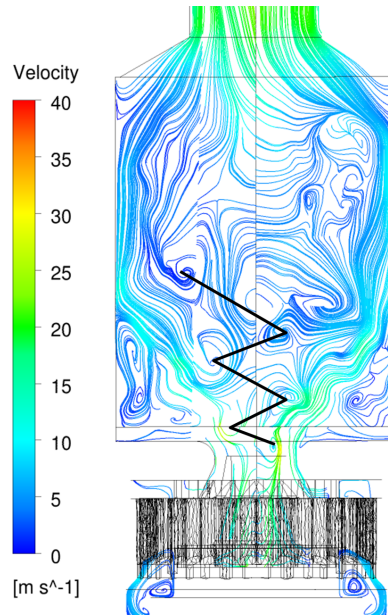


Figure 4.2.18: Baseline testcase. Streaklines plot of an instantaneous velocity field, $[m/s]$.

velocity. In the following, it will be shown that the inner recirculation zone (IRZ) is not just forced to rotate around the axes due to this pressure gradient, but also precesses; the structure identifies therefore a so called precessing vortex core (PVC). A comprehensive review of the arising vortical structures due to vortex breakdown and their behavior in swirled combustion chamber configurations is reported in [56]. A tornado-like vortical structure created by the contraction of the combustion chamber into the exhaust tube, is also clearly visible in figure 4.2.19. The pressure decrease is responsible of the higher axial velocity at the outflow of the chamber, as well as of the contraction of the IRZ in correspondence of the centerline, figure 4.2.4b. For other thermal loads, these structures have already been observed in the gas film nozzle model combustor, as reported in the experimental work of Stöhr et al., [86], [87] and simulated by Widenhorn et al., [98], [97]. The position of the tornado-like vortical structure at the exit must be quite stable as shown by the low and almost constant values of axial RMS velocity component, Fig. 4.2.8b, while the peaks of circumferential and radial RMS velocity components at the centerline, figures 4.2.8d and 4.2.8f, indicated the structure revolution around the geometrical axis of the chamber. The very good agreement of the RMS values of the three velocity components computed within the numerical simulation and those measured in the experiments suggests the turbulence model predicted the three-dimensional time-dependent structures well, figures 4.2.6 - 4.2.8.

The identification of the frequency associated with the PVC can be done in two different ways: either by analyzing, through a Fast Fourier Transformation (FFT) the velocity signal of monitor points in the ISL, or by evaluating the power spectrum of the difference of the pressure signals of monitor points located at two opposite combustion chamber walls, i.e. with a relative angle difference of 180 degree. Following the experiments of Stöhr et al., who through the analysis of the pressure spectrum measured a frequency of 510 Hz, figure 4.2.20 shows the corresponding

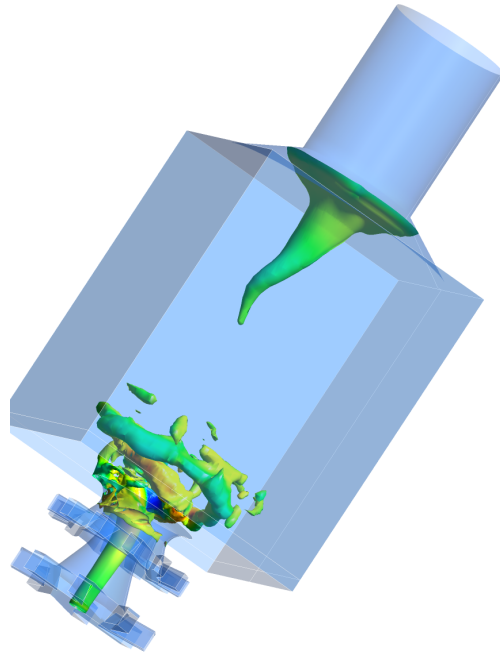
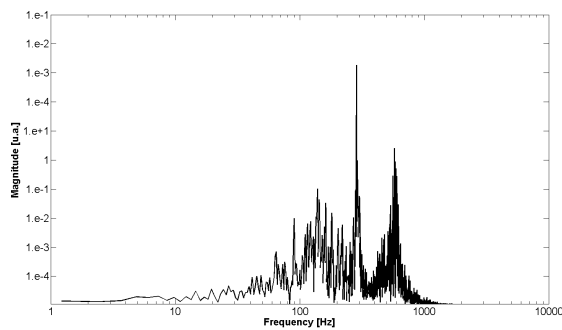
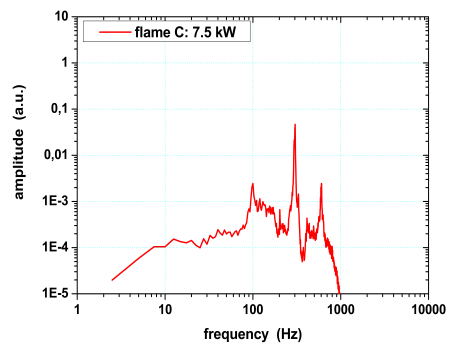


Figure 4.2.19: Baseline testcase. Unsteady structures: helical and tornado-like vortex described by iso-surface of pressure.



(a) Numerical Simulation, case C



(b) Experimental Measurements

Figure 4.2.20: Representative pressure spectrum.

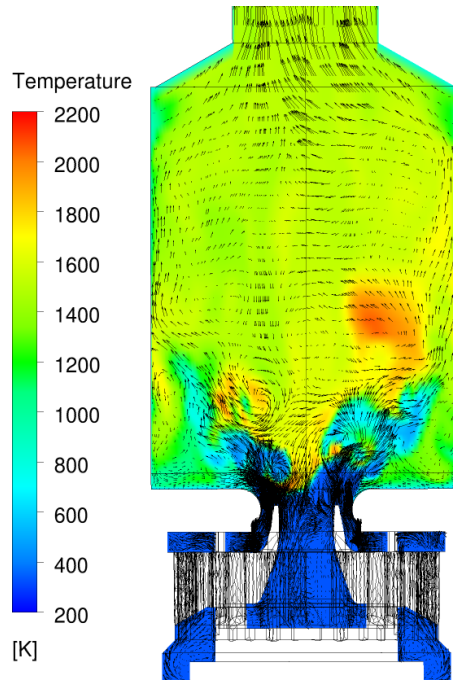


Figure 4.2.21: Case C. Planar velocity vectors on temperature contour, in [K].

power spectrum of the pressure difference at the two opposing monitor points; these are in perfect agreement with the measured data, [94]. The signals of figure 4.2.20 are extracted 56 mm above the inlet of the combustion chamber, but the same very good consistency between experiments and numerical simulation could be proved at all positions along the combustion chamber. The peak at 290 Hz corresponds to a thermo-acoustic oscillation, as it was reported already in many publications about the gas film nozzle model combustor, i.e. [73]. The other peak at 590 Hz is probably a second harmonic of the 290 Hz signal. Moreover, frequency peaks are spread around 150 Hz is shown. This augmented pressure signal can be associated with the local extinction of the flame; in fact, instabilities near LBO conditions are random rather than periodic, [23], and this could cause the broadband low frequency signal.

The unsteady behavior presented by flames next to LBO is characterized through the interaction of the flow field and the flame surface: many authors describe a disruption of the flame front due to the penetration of vortical, turbulent structures in the reaction zone, [82, 23]. In fact, also for case C a mutual interaction of the flow field on the flame and vice versa is observed, figure 4.2.21: the vortical structures are visualized by means of flow vectors, the contour plots evidence how the fresh mixture is entrained in the vortical structures and transported downstream. Therefore, occasionally the fresh mixture ignites further downstream of the flame root. This was confirmed by the analysis of the flame front, which is here visualized by means of the reaction rate of the methane reaction; figure 4.2.22 reports the development on surface A, in blue in figure 4.2.3b, of the flame front over a PVC period. The proper interpretation of such post-processed results can be very helpful: as pointed out by Boxx et al.[8, 9], isolated portions of the flame front on a surface do not necessarily suggest a disrupted flame sheet but can also be a continuous flame wrinkled in three dimensions. Therefore the analysis of the

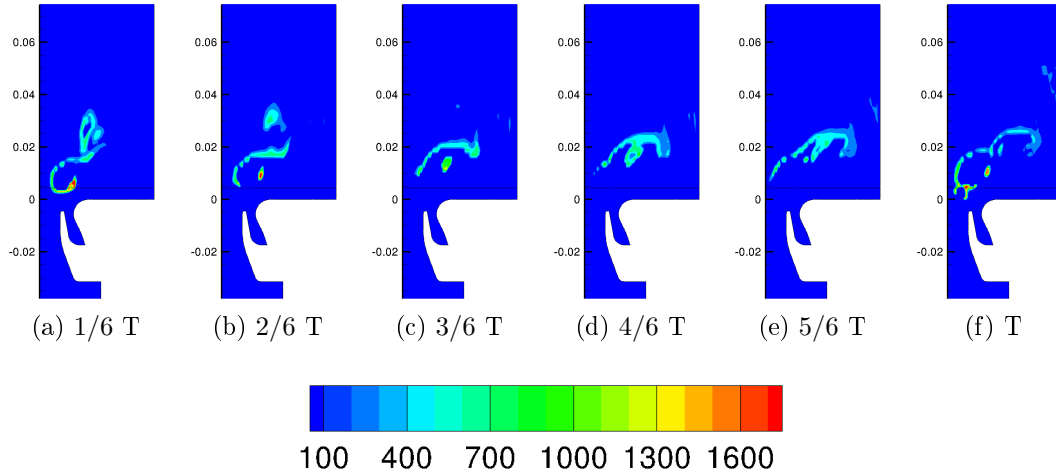


Figure 4.222: Case C. Development of the reaction rate contour, $[mol/(cm^3s)]$, on surface A over a PVC period.

same quantity on a perpendicular surface, plane B, can help to draw the proper conclusions. Figures 4.222c, 4.222d, 4.222e suggest a flame root extinction, in fact, no flame sheet is to see till $x = 10$ mm, still the flame root does not extinguish at all. As it can be seen in the series of instantaneous shots in figure 4.223, plane B, the flame root and the flame front itself follow the dynamical behavior of the PVC, precessing around the central axis, and therefore disappearing locally from plane B. On contrary, the local absence of the flame on plane B at $x = 20$ mm and upwards in figures 4.222a, 4.222b, 4.222c, as well as in figure 4.223f suggest that there a real local extinction takes place.

The precession of the flame structure can be identified even better when analyzing the single shots over a PVC period of the temperature contours, figures 4.225 and 4.224. Figure 4.224 particularly shows that the flame root remains anchored on the flame holder, although as well evidenced in figure 4.225 the flame dynamics are highly unsteady and mixing is strongly enhanced by vortical flow. The flame root behavior is different than that observed in the experiments: Stöhr et al. [88] reported that the flame root extinguished over several PVC periods and this is considered the main effect causing a complete blow off of the flame. Since in the simulation the flame is anchored indefinitely on the central body of the chamber, no complete blow off could be reproduced.

Further information on the flame behavior were drawn by the analysis of scatter plots. Figure 4.226 reports three scatter plots at respectively 5, 10 and 20 mm height in the combustion chamber. The symbols represent single instantaneous samples and each color distinguishes a radial position, red points are positioned at $r = 0$ mm, i.e. at the chamber axis, blue points are at $r = 15$ mm, green ones at $r = 25$ mm. The blue point, depending on the height at which they are extracted, are statistically located in the CRZ, ISL for $x = 5$ mm and 10 mm respectively and almost in the fresh flow stream at 20 mm height. The green points are statistically located in the ORZ and, at $x = 20$ mm, eventually in the outer shear layer (OSL); clearly these positions can just represent an average configuration, since the flow is highly unsteady

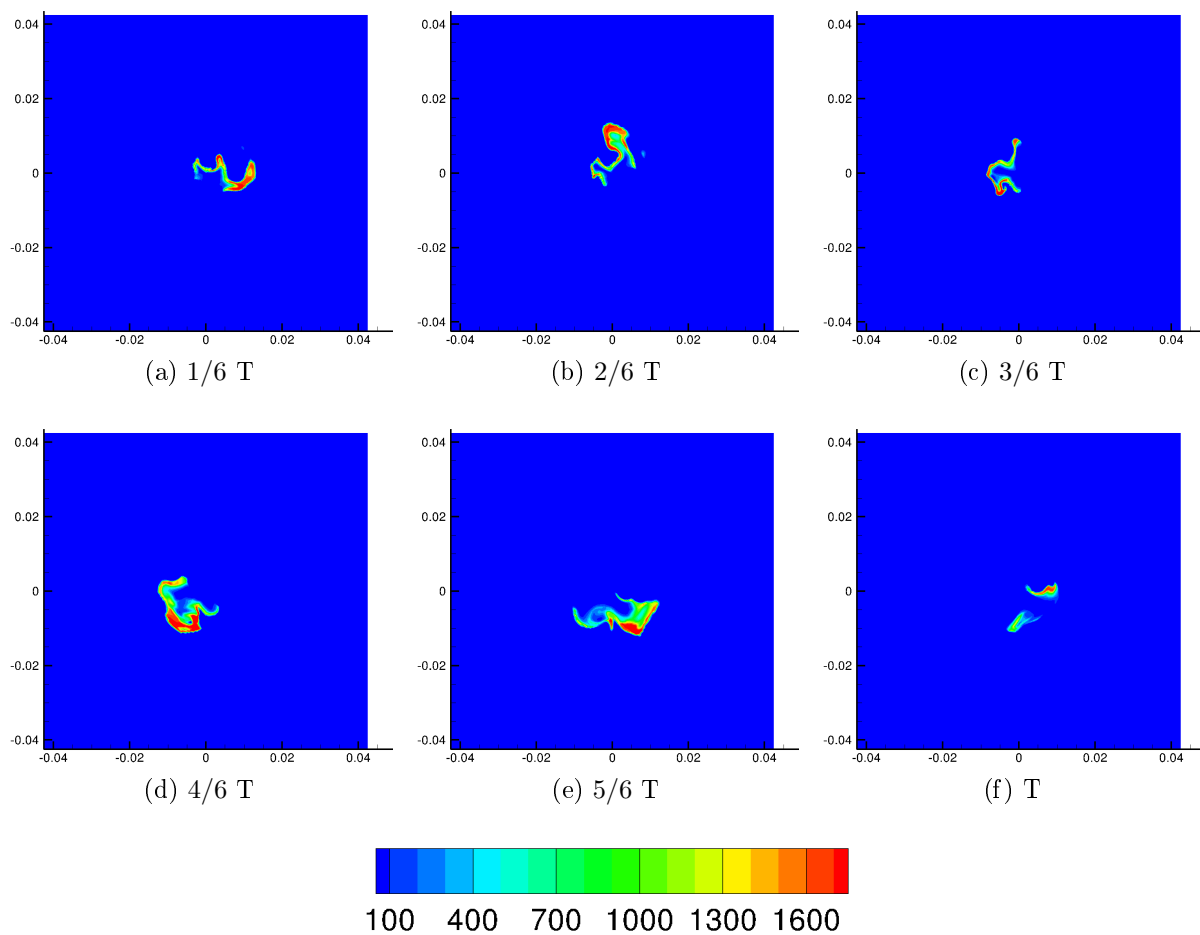


Figure 4.2.23: Case C. Development of the reaction rate (step 1), $[mol/(cm^3s)]$, on plane B over a PVC period.

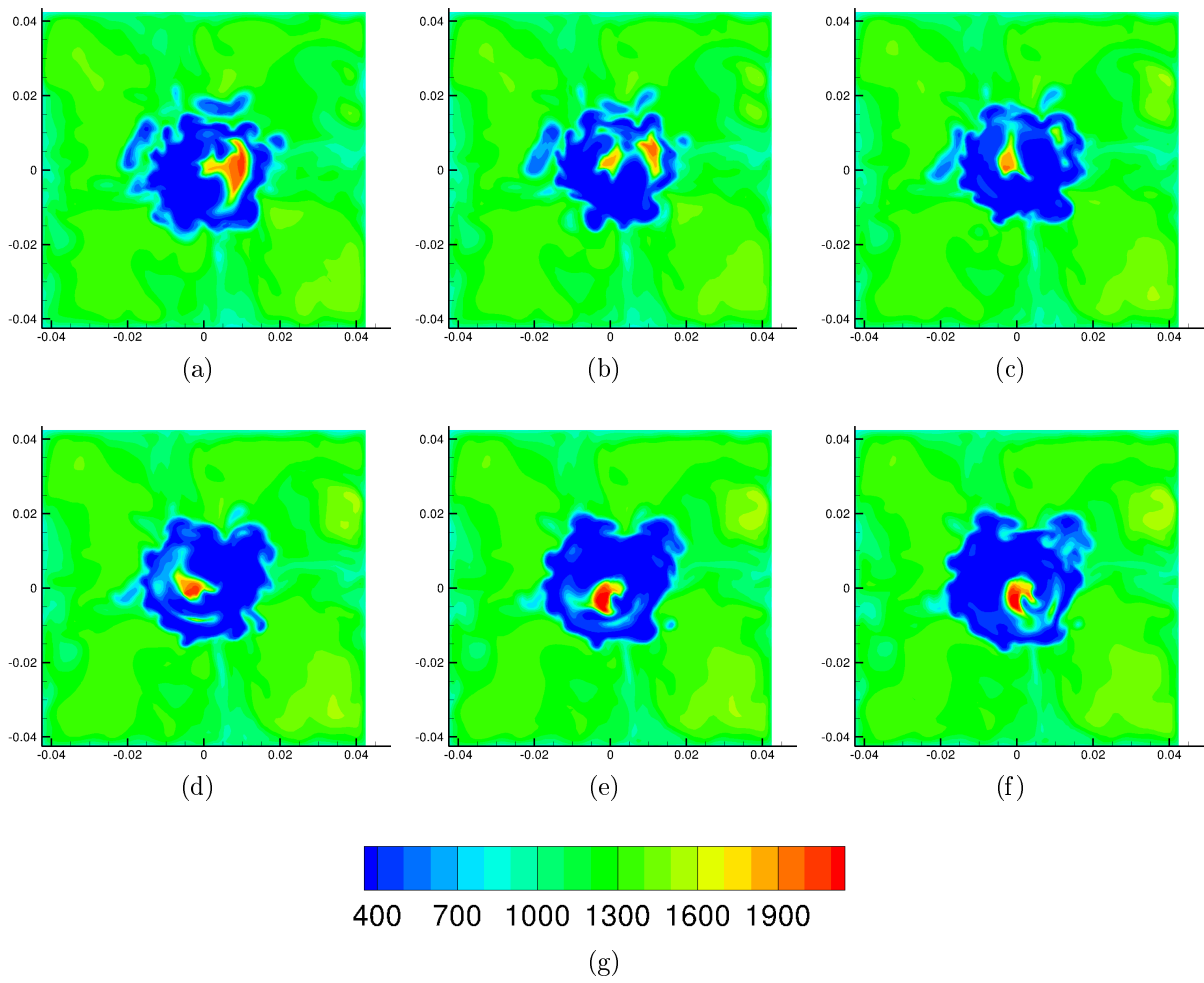


Figure 4.2.24: Case C. Development of temperature contour, in $[K]$ on plane B over a PVC period.

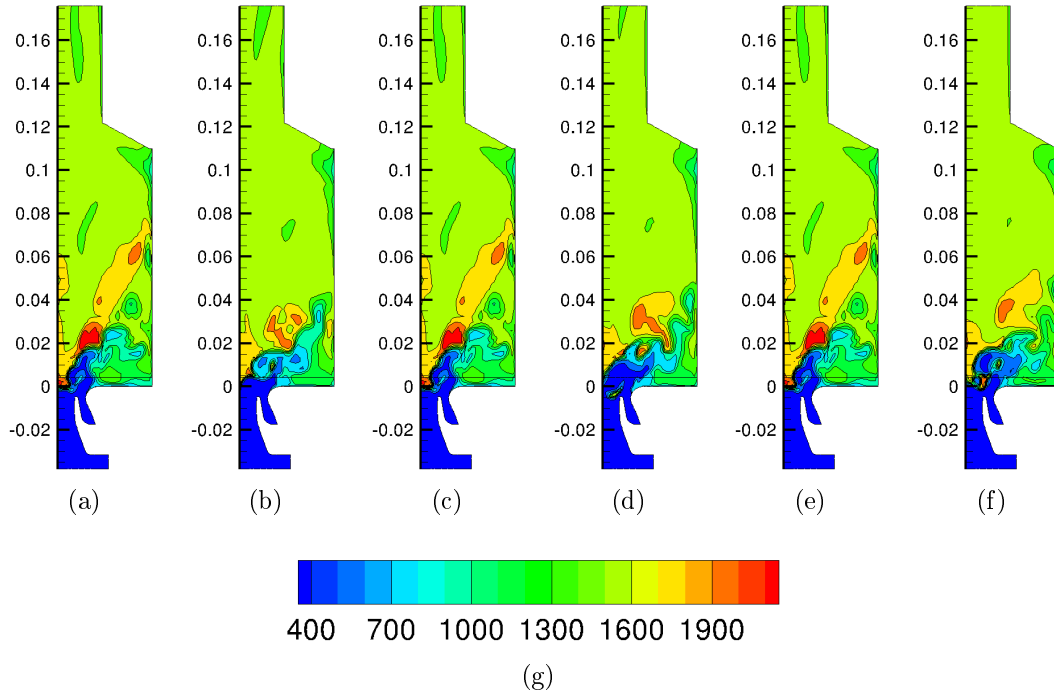


Figure 4.2.25: Case C. Development of the reaction rate contour, $[mol/(cm^3s)]$, on plane A over a PVC period.

and turbulence dominated and the averaged zones, as represented in figure 4.2.4, are therefore very different from the instantaneous configurations. As a reference to discuss the scatter plots, the chemical equilibrium curve, result of a Cantera simulation for a perfectly premixed mixture with no strain adopting the GRI 3.0 mechanism, is reported in all figures, black line, and also the averaged mixture fraction, $f = 0.031$, table 4.2 is plotted with a black dashed line. For all three plots the values are scattered from $f = 0$, pure air, to $f = 0.15$.

Figure 4.2.26a reports just the position next to the flame holder at the chamber axis. Most of the points are next to the chemical equilibrium curve and suggest that the mixture in this position is mostly burned, as expected since the flame does not extinguish at the flame root. There are still some points scattered at lower temperature, but most likely these are due to mixing effects and not to extinguish phenomena. It is interesting to notice that the largest amount of the points have a mixture fraction around 0.05, indicating that fuel is preferentially transported in the central part of the combustion chamber. The same observation was done by Meier et al. [50] analyzing the scatter plot from the experiments of the gas film model combustor in this same configuration.

The red dots concentrate along the chemical equilibrium curve also 10 mm above the nozzle, figure 4.2.26b. Here, also two further positions are plotted: the blue dots are points situated at radius 15 mm, i.e. in the ISL. A lot of these points present very low temperatures, around 400 K, and have mixture fractions ranging from 0 to 0.05, suggesting that the flame is fairly premixed; this was already suggested by the observations of the averaged temperature contour plot, figure 4.2.16. Nevertheless, it is important to notice that a certain amount of pure air is present, so it is right to describe the flame as technically premixed. The ORZ, green dots,

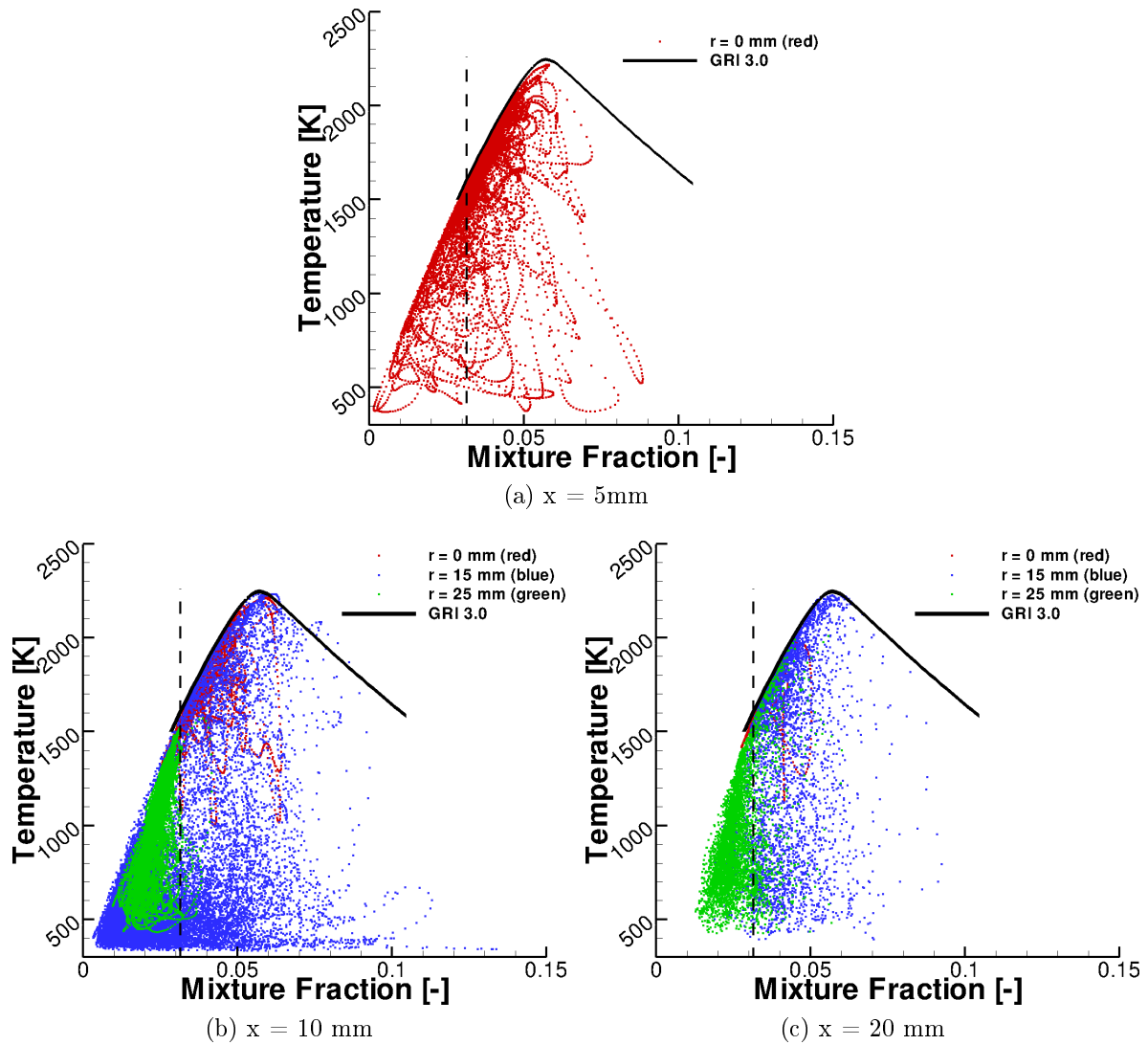


Figure 4.2.26: Case C. Scatter plots.

is a very lean region. This was explained in the previous experimental work, [50], by the fact that combustion is enhanced and stabilized in such swirled devices by the recirculation of hot gases. This happens though mainly in the IRZ, since the ORZ remains isolated due to the strong boundaries created by the ISL and the OSL. Generally the plots, except for the points along the axis, are dominated by partially reactive mixtures due mainly to local extinction phenomena. In the experiments this behavior was observed till $x = 30$ mm, by 60 mm height the values were all around the adiabatic conditions, [50].

4.3 High Frequency Instabilities

The possible mechanisms originating high frequency instabilities have been numerically studied on a swirled lean premixed can combustor.

4.3.1 Test-Case Configuration

As already pointed out in chapter 2, when analyzing high frequency instabilities very small length and time scales play a crucial role and lead to severe prerequisites concerning the computational grid, which must be very fine resolved, and simulation time steps, which have to be small enough to capture frequency dependent phenomena of some kHz. Therefore, it was important to adopt a compact device and finally keep the computational effort to reasonable values. The geometry presented is derived by the experiments of Richards, et al. [76], [78], who was able to test the sensitivity of the combustion chamber to several parameters, obtaining reliable stability charts, evidencing the operational points most prone to unstable behavior, which are finally those adopted in this study. Moreover, Di Sarli et al. used this combustion chamber configuration in a previous numerical study, [19], and were able to prove that high frequency instabilities arise in this device. Though, in their work Di Sarli et al. approached the problem with URANS simulations, introducing high uncertainties in their solutions due to the numerical models themselves, which are not able to resolve the turbulence spectrum, [68].

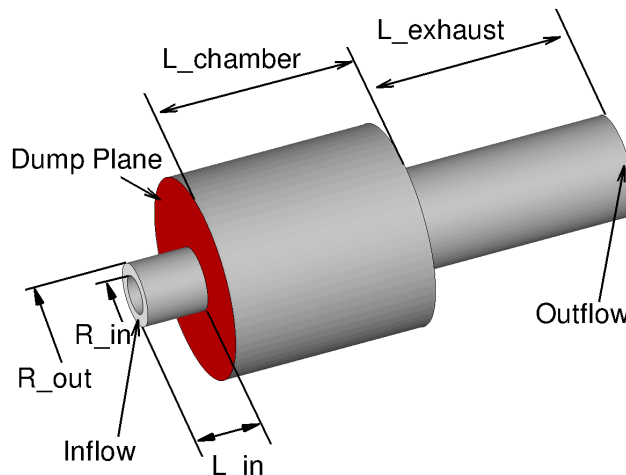


Figure 4.3.1: Schematic representation of the computational domain.

Table 4.4: Basic testcases set up for the swirled, lean, premixed can combustor configuration.

T_{in} [K]	Φ	T_{walls} [K]	$Pressure_{ref}$ [Pa]	$Timestep$ [s]
533	0.77	400	$5 \cdot 10^5$	$1 \cdot 10^{-5}$

Table 4.5: Main features of the testcases for the swirled, lean, premixed can combustor configuration.

<i>Case</i>	<i>Inlet Duct Length</i>	<i>Inlet Velocity</i>	<i>Dump Plane Wall</i>	<i>Numerical Models</i>
$B - L_{60mm}$	60 mm	20 m/s	isotherm	SAS, EDM/FRC
$W - L_{60mm}$	60 mm	20 m/s	adiabatic	SAS, EDM/FRC
$B - L_{40mm}$	40 mm	30 m/s	isotherm	SAS, EDM/FRC
$LSC - L_{60mm}$	60 mm	20 m/s	isotherm	SAS, non reactive

The computational domain is sketched in figure 4.3.1. The inner and outer radii are 0.0193 m and 0.0316 m, respectively, the chamber and the exhaust pipe are both 0.2 m long and have a diameter of respectively 0.2 and 0.1 m. The chamber is operated in fully premixed conditions, at a lean fuel to air ratio of $\phi = 0.77$. The flow developing in the chamber is swirled, although the swirler is not included in the domain to reduce grid points, but is imposed through appropriate boundary conditions: at the inlet velocity boundary conditions are applied to recreate the swirler effect, based on bulk flow and geometrical consideration. Premixed methane and air are introduced in the chamber at a temperature of 533 K. Turbulent properties were set at the inflow to achieve a turbulent length scale of 1 mm and a turbulence degree of 5%, thus any anisotropy of the turbulence was neglected at the inflow boundary. The outflow is positioned after an exhaust tube, in order not to affect the region of interest of the combustion chamber and pressure boundary conditions are prescribed there. The walls in the domain are isothermal except for the dump plane, figure 4.3.1, which, depending on the simulated testcase, is or isothermal, i.e. cooled at 400 K, or adiabatic. The main computational parameters are listed in table 4.4.

Four different configurations have been tested to analyze different effects and mechanisms leading to high frequency instabilities. Table 4.5 reports the main parameter for each simulation. From case $B - L_{60mm}$ to case $W - L_{60mm}$ the boundary conditions applied at the dump plane vary from isotherm to adiabatic, enabling to identify the role played by the cooling effect of the wall on thermo-kinetic instabilities. In case $B - L_{40mm}$ a slightly different geometry, with a shorter inlet duct of 40 mm and higher overall mean velocity at the inlet, is used to investigate the effect of swirling dependent structures. From this analysis it was clear that the disruption of coherent structures after the dump plane due to high swirl number, as already observed by [33], could be reproduced here too. Finally, case $LSC - L_{60mm}$ was performed to assess the behavior of the flow structures at a lower swirl number. Therefore the case was run non-reactive

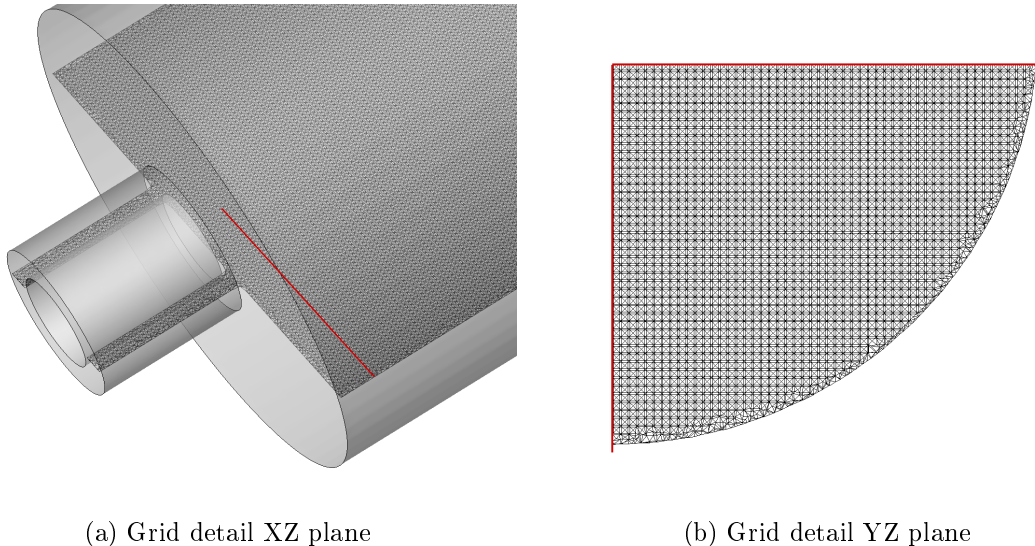
to avoid the influence of the combustion zone on the PVC and on the vortex shedding at the dump plane.

The swirl number can be calculated by means of geometry parameters using the definition of Huang, et al. [33]:

$$S = \frac{2}{3} \left[\frac{1 - \left(\frac{R_{inner}}{R_{outer}}\right)^3}{1 - \left(\frac{R_{inner}}{R_{outer}}\right)^2} \right] \tan\beta \quad (4.3.1)$$

For cases $B - L_{60mm}$, $W - L_{60mm}$ and $B - L_{40mm}$ a swirling angle of 45 degrees was chosen, realizing a swirl number $S=0.9$, while for case $LSC - L_{60mm}$ the angle was changed to 22.5 realizing a swirl number of 0.37. The Reynolds number, calculated at the inlet with the hydraulic diameter of the inflow duct was 127000 for case $B - L_{40mm}$ and 85000 for all other testcases.

All test-cases have been simulated in full domain, i.e. 360 degrees, on the same computational grid, of which two particulars are extracted in figure 4.3.2; the grid cells are tetrahedral with prism layers at the walls. For case $B - L_{40mm}$ the inlet duct was shortened, but the grid was kept the same as for the other test-cases. The fine spatial resolution required, led to 2.72 million points for case $B - L_{40mm}$ and 2.75 million points for all other simulations. Moreover the same models were adopted for all simulations, i.e. an SAS-SST hybrid RANS/LES model ensured the resolution of large portions of turbulent scales, while an EDM combined with FRC modeled the combustion process. To assess the effect of chemical kinetics, the single-step mechanism of Truffin et al. [90] was used. The simulations were run at high pressure, 5 MPa, as it is common in technical-relevant configurations. The time step was chosen to ensure an overall Courant number around one in the whole domain and to meet the basic requirements of the turbulence model.



(a) Grid detail XZ plane

(b) Grid detail YZ plane

Figure 4.3.2: Grid adopted in the simulations.

The residence time was used as an indicative value to estimate the time needed for achieving converged statistics. It was calculated by means of the mean axial velocity and is 0.05 seconds for case $B - L_{40mm}$ and 0.07 seconds for all other test-cases. The method adopted for obtaining

the statistically converged results was the same for all simulations. After the simulation has been initialized with a URANS simulation, two residence times were simulated to overcome the transient phase and finally all converged solutions were obtained over the averaging of at least three residence times. The simulations were performed on a high performance cluster equipped with Intel Xeon X5570, quad-core processors. 40 central processing units (CPU) were used to run the simulations, leading to an averaged CPU time of 8.5 hours per residence time.

In order to have a broad band of data to rely on, the combustion chamber domain was equipped with monitor points, figure 4.3.3a, to perform frequency analysis on all relevant simulation parameters, e.g. velocity, temperature, mass fraction of methane, pressure, and have a clear time-dependent history of the development of the unsteady features of the combustion chamber. In particular, the following monitor points were placed at positions which are very important for the discussion in section 4.3.2: monitor point 1 is directly next to the dump plane, at the flame root, monitor point 4 was set at the average position of the flame front and monitor point 8 is at the tip of the averaged flame configuration. Moreover, contour plots of the time-averaged and instantaneous simulation results will be presented in the following along the extracted surface marked in figure 4.3.3a, and profiles of the main relevant quantities are extracted at different heights in the chamber to enable a direct confrontation between the test-cases. Some of the findings presented in the following parts of this section have already been published by Rebosio et al. [74].

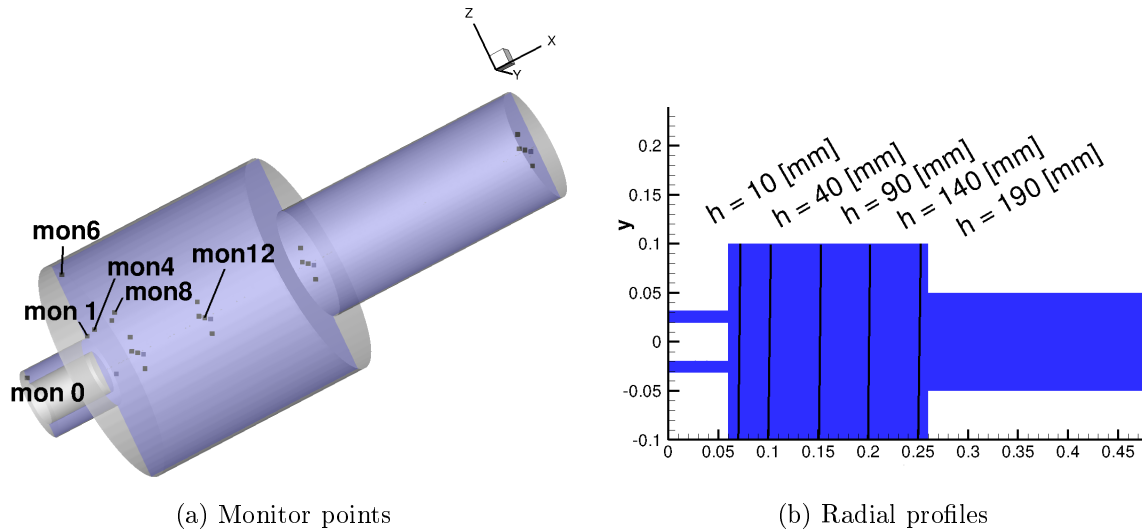


Figure 4.3.3: Monitor points and radial profiles used for post-processing.

4.3.2 Results

When creating a numerical database to analyze physical problems, as it was the aim of this study concerning high frequency instabilities, and not being able to rely on a large amount of experimental results, it is crucial to ensure a good quality for the performed numerical work. It was already pointed out that the computational grid as well as the time step were chosen in order to obtain overall values of the Courant number around one, ensuring the turbulence model to work within the prescribed boundaries. Moreover it is known from literature, see

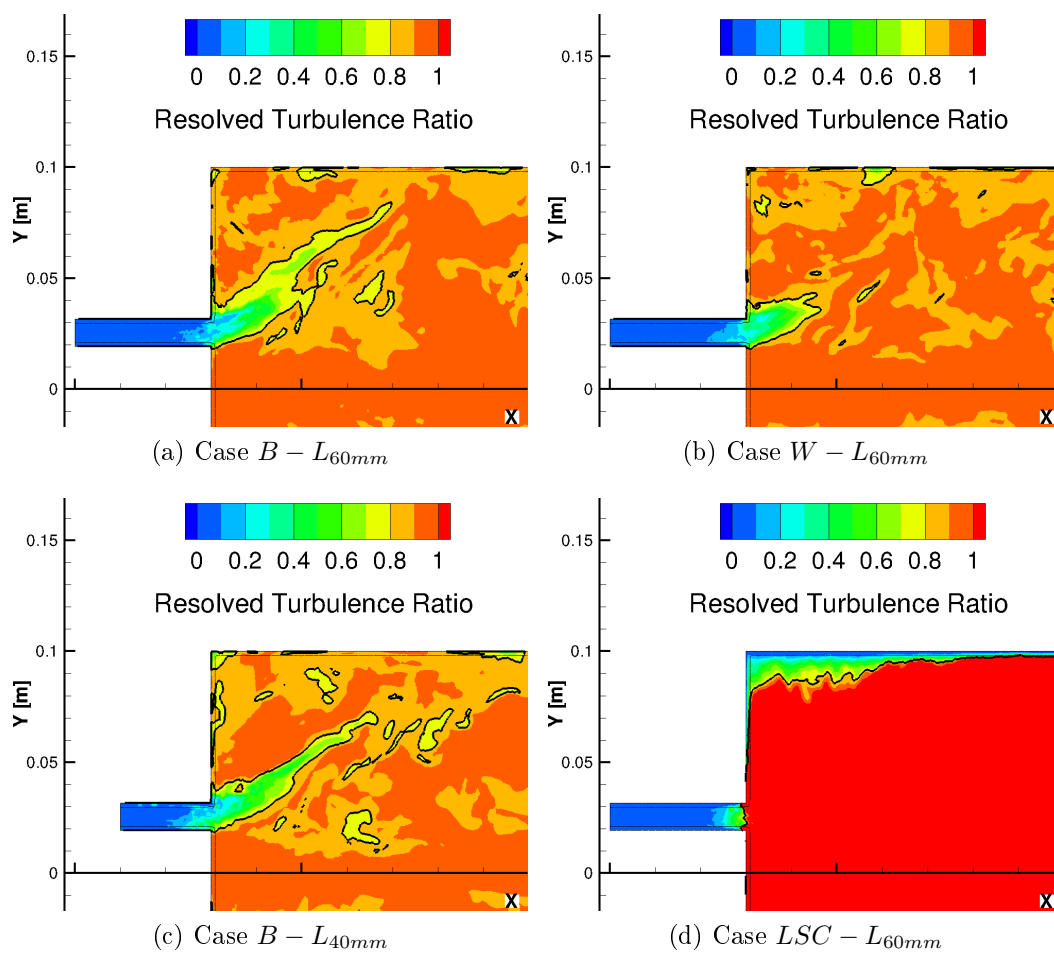


Figure 4.3.4: Resolved turbulence ratio (R_{Tu}) contour plots and isolines at $R_{Tu} = 0.8$.

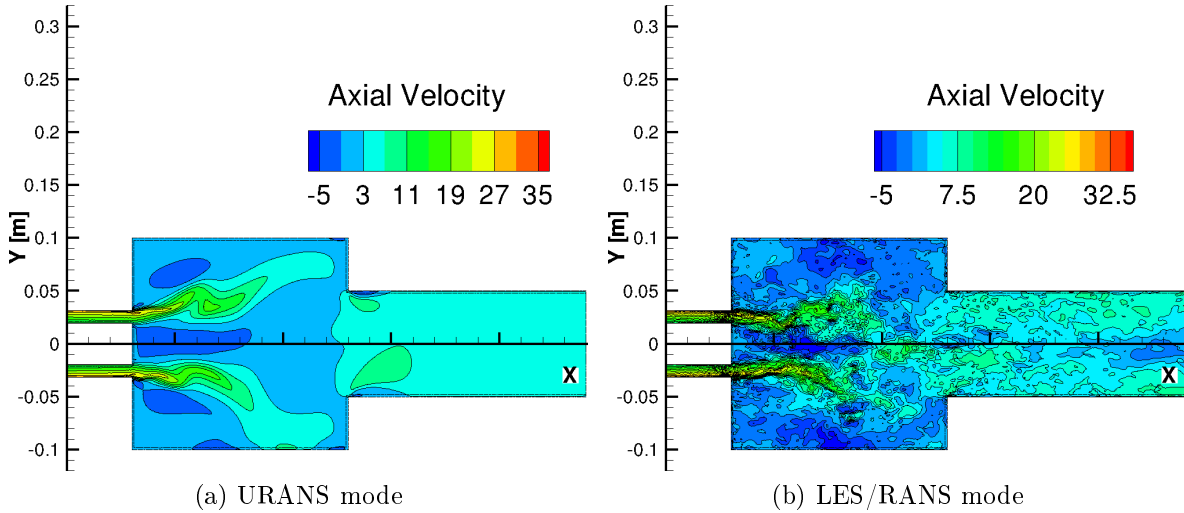


Figure 4.3.5: Instantaneous axial velocity field [m/s] for case $LSC - L_{60mm}$ performed with URANS and hybrid LES/RANS approach.

chapter 2, that the interaction between turbulence and chemistry can eventually play a decisive role, which implies the need of the good resolution of a large part of the turbulent spectrum. Figure 4.3.4 reports the resolved turbulence ratio, which identifies the ratio of resolved to global, i.e. resolved and modeled, turbulence energy, and is defined by equation 4.3.2:

$$R_{Tu} = \frac{0.5 (\bar{u}'^2 + \bar{v}'^2 + \bar{w}'^2)}{0.5 (\bar{u}'^2 + \bar{v}'^2 + \bar{w}'^2) + \bar{k}} \quad (4.3.2)$$

When the value of R_{Tu} is close to one, a very large part of the turbulent spectrum is resolved, so that it is possible to say that the SAS-SST model works in an LES-like mode and its results are of the same quality as an LES. In figure 4.3.4 the black line marks the value $R_{Tu} = 0.8$, the zones in orange and red, are those at higher values, where very large portions of turbulence are resolved. As a matter of fact, the computational field was solved in LES mode in the zones of highest interest, i.e. directly after the dump plane and in the recirculation zones. It is interesting to notice that case $LSC - L_{60mm}$ is almost completely resolved in LES-mode.

To clarify the differences between a URANS and a hybrid LES/RANS approach figure 4.3.5 shows the instantaneous axial velocity field for case $LSC - L_{60mm}$ calculated with the two different turbulence modeling approaches. Clearly, also the URANS simulation, figure 4.3.5a, captures some unsteady features of the flow, like the flapping of the fresh reactants stream entering the combustion chamber, but fails to predict all small structures, which are intrinsically connected with a detailed resolution of the turbulence spectrum and are well reproduced when performing the same simulation with the hybrid LES/RANS method, figure 4.3.5b.

4.3.2.1 Characterization of Flow Field and Combustion Main Features

The main features typical of swirled flows are clearly visible in figure 4.3.6. The streaklines, superimposed in the plots to the time-averaged axial velocity contours, evidence the central recirculation zone (CRZ) as well as the outer recirculation zone (ORZ). The three test-cases

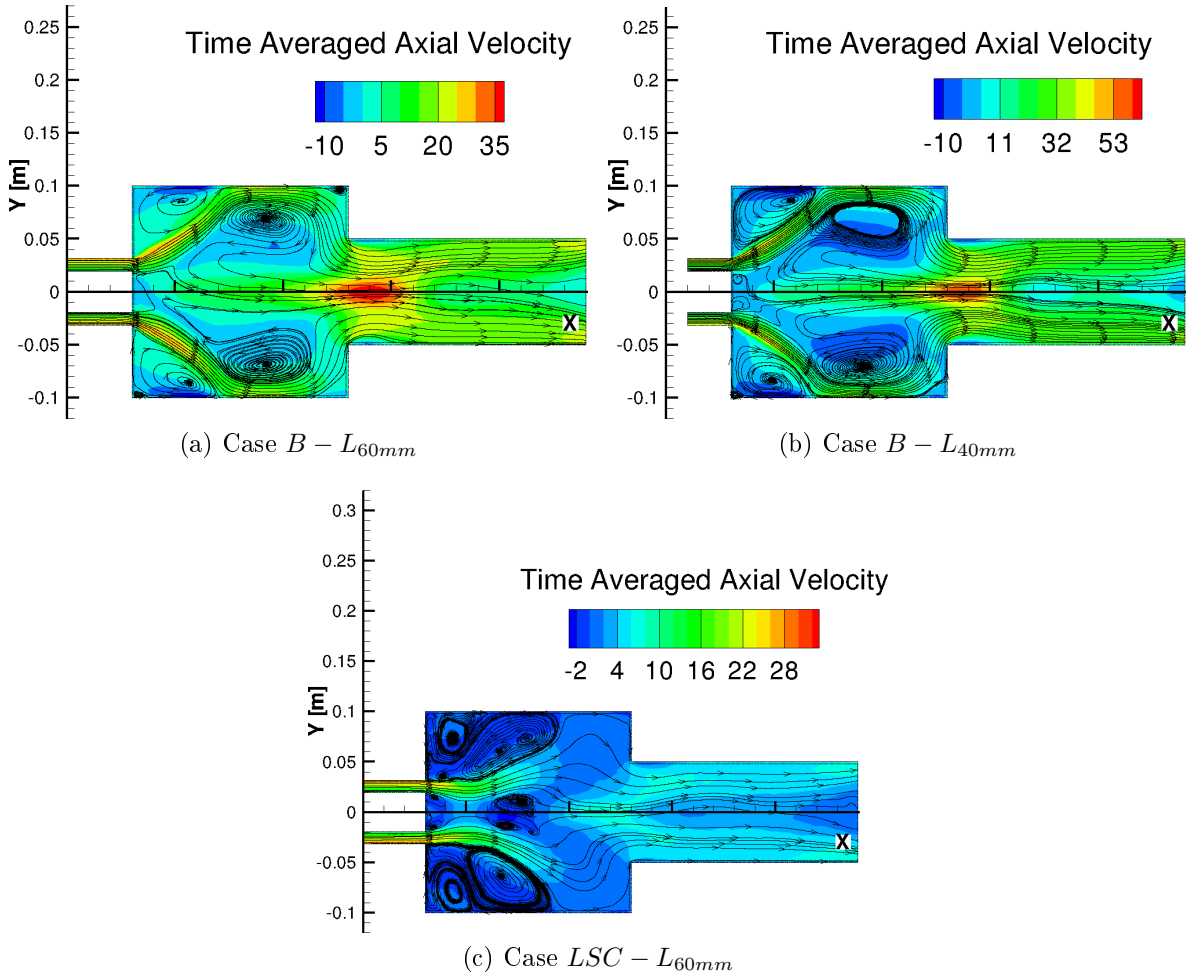
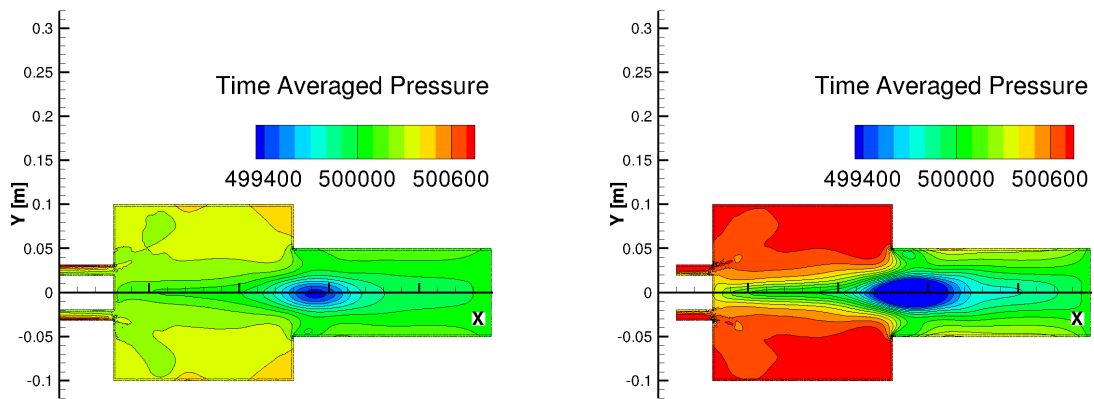
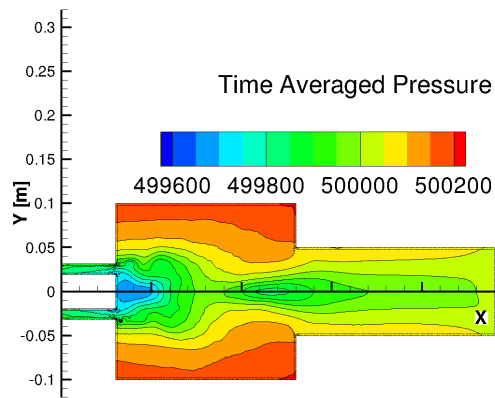


Figure 4.3.6: Contour plots of time-averaged axial velocity [m/s] and streamlines.

in figure 4.3.6 present some differences. In particular, case $B - L_{40mm}$, which differs from case $B - L_{60mm}$ due to the shorter inlet duct and the higher overall velocity at the inlet, presents a higher velocity in the recirculation zones as well as in the streams coming from the inlet. The lower swirl number in case $LSC - L_{60mm}$ causes a drastic change in the flow structure, figure 4.3.6c: although the CRZ and the ORZ are visible, the flow assumes a V-shaped configuration, which is much more closed towards the centerline than that of the other two cases; the ORZ is much larger than in the other cases and penetrates much deeper in the combustion chamber.

The data that can be extracted by the observation of the time-average pressure field for the three test cases resemble those of the time-averaged velocity field, figure 4.3.7. All three test-cases reveal a pressure minimum at the contraction of the combustion chamber into the exhaust tube, which will be shown in the following to be very important for the dynamics in the chamber. Case $LSC - L_{60mm}$, figure 4.3.7c, shows a different configuration, compared to cases $B - L_{60mm}$ and $B - L_{40mm}$ at the dump plane, due to the different shape of the ORZ.

The time-averaged flow field of case $W - L_{60mm}$ is not presented, since its structures and intensities are almost coincident with those of case $B - L_{60mm}$, as it can be seen by means of the profiles of time-averaged velocity components extracted 20 mm above the dump plane, see

(a) Case $B - L_{60mm}$ (b) Case $B - L_{40mm}$ (c) Case $LSC - L_{60mm}$ Figure 4.3.7: Contour plots of time-averaged pressure [Pa].

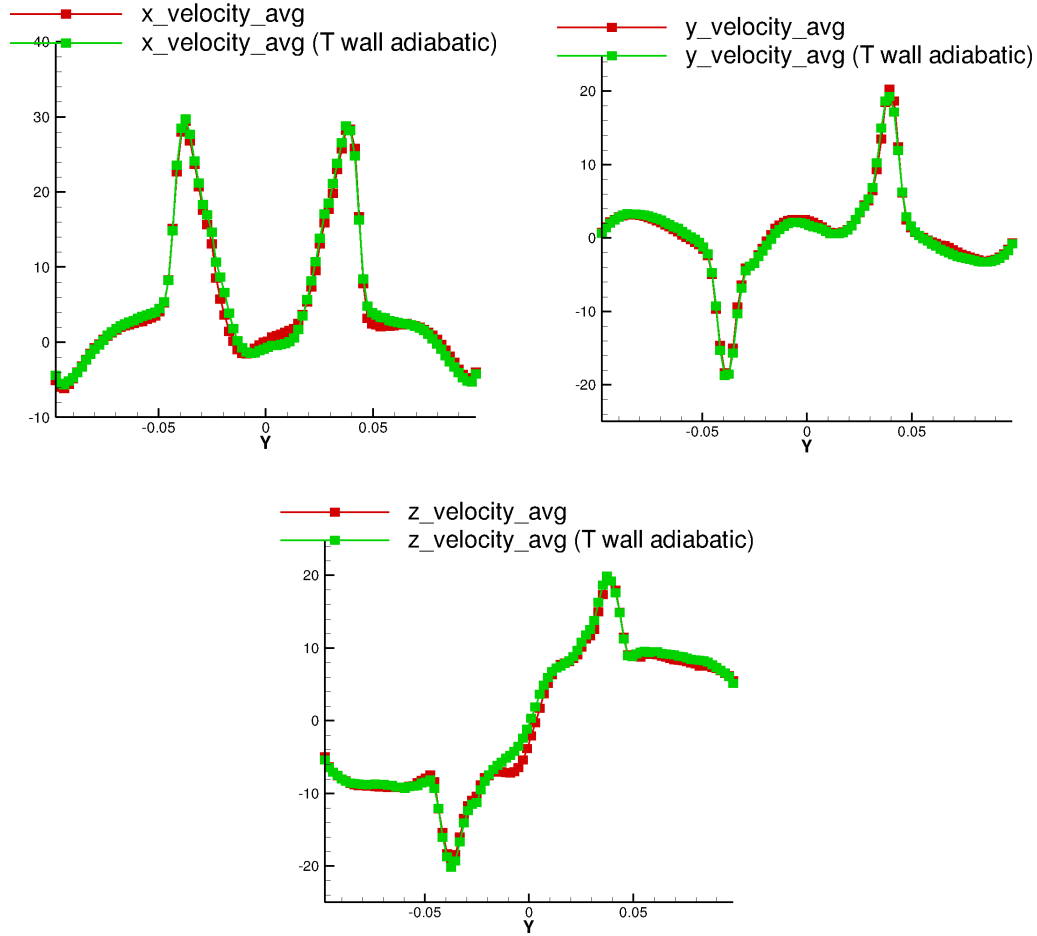


Figure 4.3.8: Radial profiles of time-averaged velocity components [m/s] at $h = 20$ mm. Red lines: case $B - L_{60mm}$. Green lines: case $W - L_{60mm}$.

figure 4.3.8; the same behavior was observed for all profiles all along the combustion chamber. In fact the two test-cases were run with the same boundary conditions for the flow field, but differed because of the boundary condition applied at the dump plane wall, which influences the resulting time-averaged temperature field, reported in figure 4.3.9. In case $B - L_{60mm}$ the dump plane was set to isothermal, 400 K; this causes the cooling of the recirculated gases which can be seen in figure 4.3.9a. When switching the boundary condition to adiabatic, case $W - L_{60mm}$ figure 4.3.9b, the cooling effect of the wall goes missing, so that not just the ORZ flow is hotter but also the flame root and this has a stabilizing effect on the dynamics of the combustor as it will be shown in the following.

The time-averaged temperature contour of case $B - L_{40mm}$ is not presented, since the field is very similar to that of case $B - L_{60mm}$, which means that although the recirculated gases proceed along the dump plane at higher velocities, these still ensure to a certain extent the cooling effect of the wall on the ORZ, as it can be seen by the comparison of the profiles of time-averaged temperature extracted at 10 and 20 mm above the dump planes for both cases $B - L_{60mm}$ and $B - L_{40mm}$, figure 4.3.10.

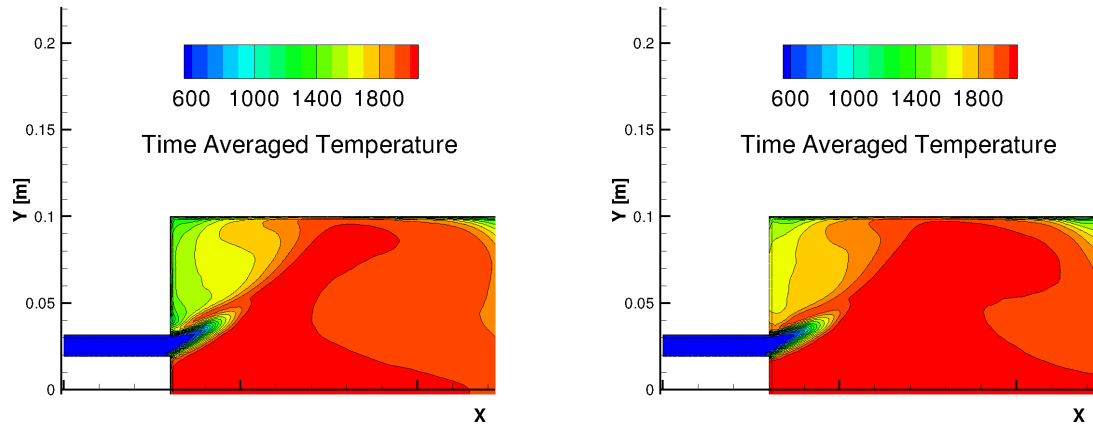
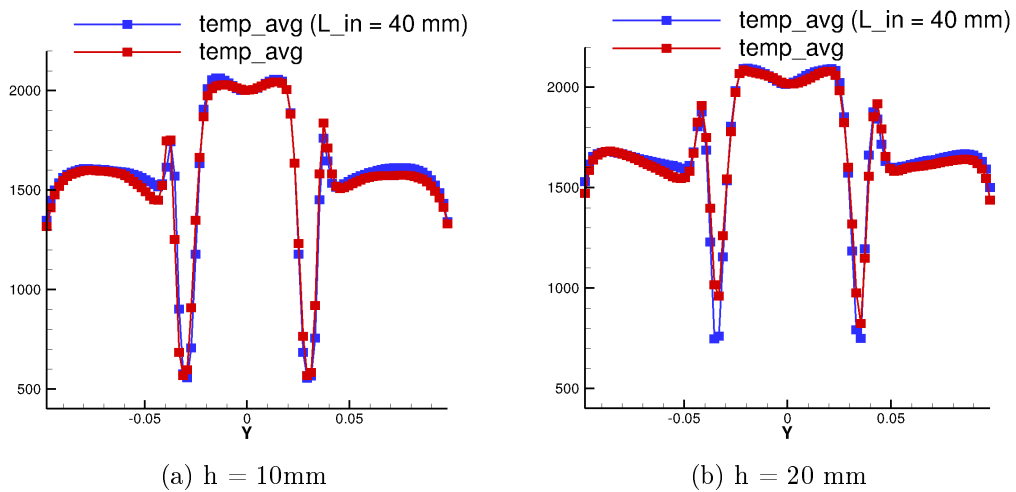
(a) Case $B - L_{60mm}$ (b) Case $W - L_{60mm}$

Figure 4.3.9: Contour plots of time-averaged temperature [K].

(a) $h = 10\text{mm}$ (b) $h = 20\text{mm}$ Figure 4.3.10: Radial profiles of time averaged temperature [K]. Red lines: case $B - L_{60mm}$. Blue lines: case $B - L_{40mm}$.

4.3.2.2 Oscillatory Behavior

The study of power spectra of time-dependent signals at different points within the computational domain enables to recognize the main periodic features of the dynamics arising in the combustion chamber. Therefore, a Fourier analysis is performed for all cases in order to identify the main frequencies characterizing the unsteady flow, afterwards these frequencies can be associated to instabilities observed in the simulations.

The Fast Fourier Transformation (FFT) for case $B - L_{60mm}$ revealed two distinct frequencies one at 2650 Hz and one at 3300 Hz. These could be seen for all analyzed quantities, i.e. axial, radial and circumferential velocity components, temperature and pressure, directly at the dump plane, monitor point 1 in figure 4.3.3a, as well as at the averaged position of the flame front, monitor point 4; exemplary in figure 4.3.11 the power spectra of axial velocity and temperature are reported. Moving downstream the combustion chamber, e.g. monitor point 8 and 12, the 2650 Hz signal disappeared, while the 3300 Hz could still be clearly identified. In a configuration similar to the presented swirled can combustor, Haung, et al. had already been able to observe a disruption of coherent structures, which could be directly related to the high swirl number, [33]. Therefore, to assess the influence of the swirl number, test-case $LSC - L_{60mm}$ has been performed and its results will be described in the following.

In chapter 2, the importance of presenting the frequency results in their non-dimensional form has already been pointed out, the Strouhal number was calculated using the hydraulic diameter of the inlet and the mean axial velocity at the inlet and is 3.25 for the 2650 Hz frequency and 4.06 for the 3300 Hz frequency. Following the definition given in chapter 2, combustion dynamics characterized by Strouhal numbers larger than one can be considered high frequency instabilities. An effort was made in order to understand which mechanisms could lead to the identified high frequency instabilities. For the 2650 Hz signal, first it was assumed that the vortices shedding at the dump plane of the combustion chamber could initialize the instability. However, the high swirl number realized in the combustion chamber would cause a fast disruption of such vortical structures, [33], so that the vortices could unlikely be able to drive the combustion oscillation. Finally, the simulation of case $W - L_{60mm}$ gave new insights in the problem and delivered valuable information for the understanding of the mechanism leading to the 2650 Hz instability. Case $W - L_{60mm}$ differs from case $B - L_{60mm}$ because of the imposed thermal boundary condition at the dump plane: in case $W - L_{60mm}$ the dump plane wall is treated as an adiabatic surface, preventing the wall to cool down the flow in the outer recirculation zone, as already shown by the time-averaged temperature contour plots in figure 4.3.9. Therefore the flame root at the dump plane experiences temperatures next to the adiabatic flame temperature and burns much more stable than in case $B - L_{60mm}$ so that no instability at 2650 Hz is present [74]. This is highlighted in figure 4.3.12, which presents the FFT of the temperature signal at monitor point 1.

The 2650 Hz dynamics was therefore supposed to be driven by a thermo-kinetic intrinsic instability as that already observed by Di Sarli, et al. [19]. The loop, which describes such

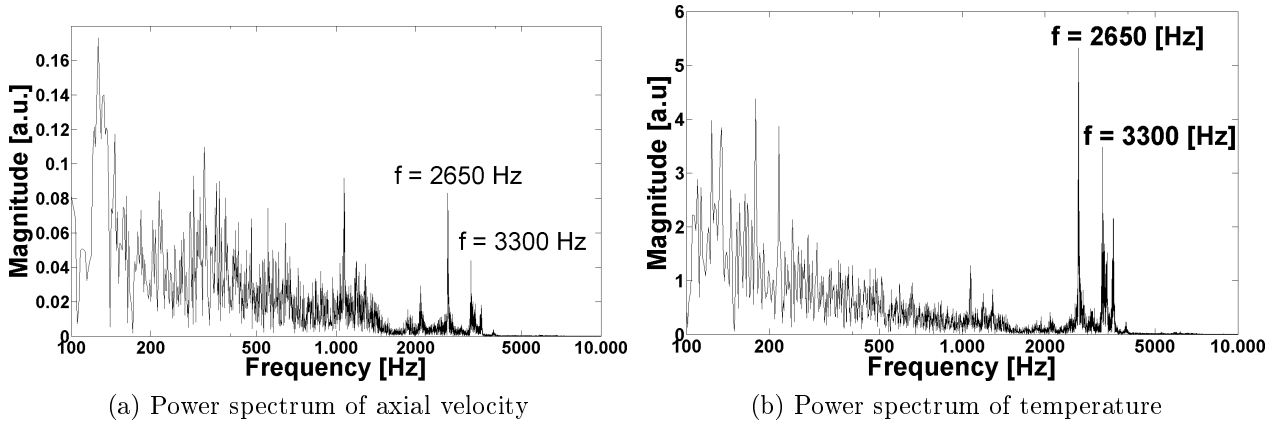


Figure 4.3.11: Case $B - L_{60mm}$. Power spectra from the Fourier analysis at monitor point 1.

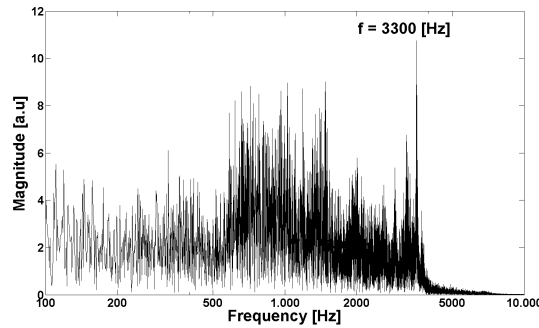


Figure 4.3.12: Case $W - L_{60mm}$. Power spectrum from the Fourier analysis of the temperature signal at monitor point 1.

a self-sustained instability, is based on the flame root cooling effect of the bottom wall of the combustion chamber and the consequent modification of the reaction rates time-lag. In fact, the flow in the ORZ experiences low velocities and the hot recirculated gases cool at contact with the dump plane, due to the high temperature gradients and in particular the root of the flame itself is cooled. The temperature in proximity of the inlet is therefore lower and the time requested to heat up the fresh mixture of air and methane entering the chamber is longer. This results in a delay in the reaction rates, so that the methane mass fraction at the flame root increases until the fuel concentration becomes sufficiently high for the combustion reaction to accelerate again. Afterwards, the temperature of the flame root increases again, creating higher temperature gradients at the wall, which drive an increase of the heat losses at the dump plane, enabling the loop to start again. Given that the described mechanism forces the instability, then the oscillating temperature and methane mass fraction signals at the flame root must be in counter-phase. Therefore, the time-dependent signals of temperature and mass fraction at monitor point 1, were reconstructed in terms of phase shift and magnitude, obtained by the FFT, and were found to oscillate in counter-phase as expected, figure 4.3.13.

Although the simulations depicted in Table 4.5 do not take into account the coupling with the acoustics of the combustor, it is legitimate to expect that, if a characteristic frequency of

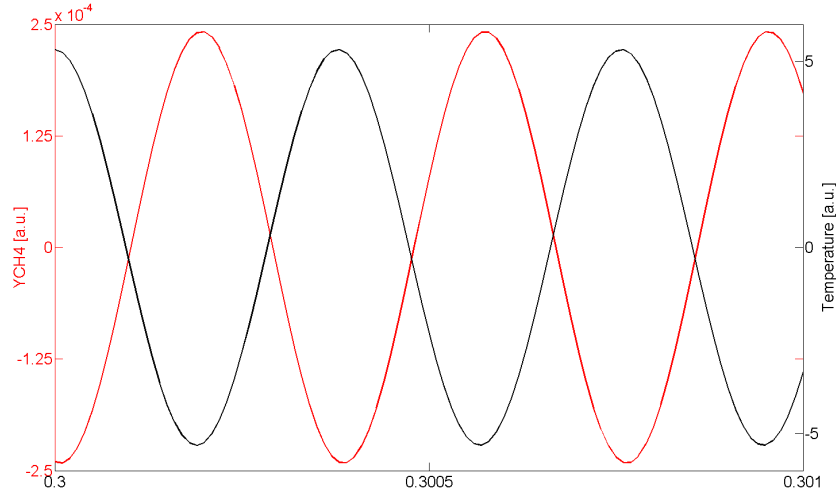


Figure 4.3.13: Case $B-L_{60mm}$. Reconstructed profiles for frequency $f = 2650$ Hz of temperature and methane mass fraction at monitor point 1.

the combustion chamber is close to the frequency of an intrinsic-instability, these will couple in the system. Therefore, the Helmholtz equations have been resolved adopting the geometry and the time-averaged temperature and density fields from case $B-L_{60mm}$ [89]. As it is highlighted in the black box in figure 4.3.14, the geometry for this simulation is slightly different than that of the CFD domain: in order to properly simulate an acoustically open end at the exit of the combustion chamber the extra portion of domain had to be added. Figure 4.3.14 shows the resulting pressure field for one of the eigenfrequencies calculated through this analysis. The mode pictured in figure 4.3.14 is a radial mode, developing at 2464 Hz. Since most of the high frequency oscillations observed in the past link with radial modes, the mode shown in figure 4.3.14 seems likely to be able to couple with the observed thermo-kinetic mechanism.

The further detected frequency of 3300 Hz, was not just present in the power spectra of case $B-L_{60mm}$, but also in those of cases $W-L_{60mm}$ and $B-L_{40mm}$. Furthermore all pressure signals from all monitor points in the chamber in the three configurations registered this frequency, e.g. the FFT of the pressure signal at monitor point 12 is shown in figure 4.3.15. The pressure field is characterized by a tornado like structure, which forms at the contraction of the combustion chamber into the exhaust tube. This structure was found to pump in and out the combustion chamber with the evidenced frequency, as it can be seen by the sequence of pictures reported in figure 4.3.16, which shows the behavior of the tornado-like structure over an oscillation period by means of a pressure isosurface for case $B-L_{40mm}$.

As already anticipated the influence of the swirl number on the coherent structures developing at the combustion chamber dump plane and their disruption while moving downstream the combustion chamber was also investigated. It is beyond the scope of this analysis to quantitatively evaluate the impact of the swirl number on the test cases, still a qualitative analysis delivers some interesting information. Figure 4.3.17 reports the instantaneous pressure field from case $LSC-L_{60mm}$ and case $B-L_{60mm}$. The two test cases differ because of the swirl

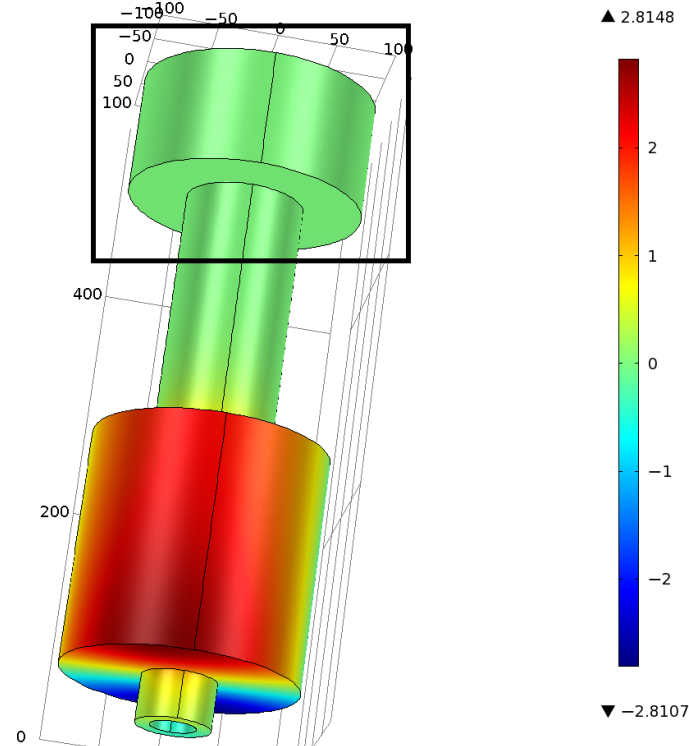


Figure 4.3.14: Case $B - L_{60mm}$. Analysis of the acoustic modes of the chamber. Eigenfrequency at 2464 Hz.

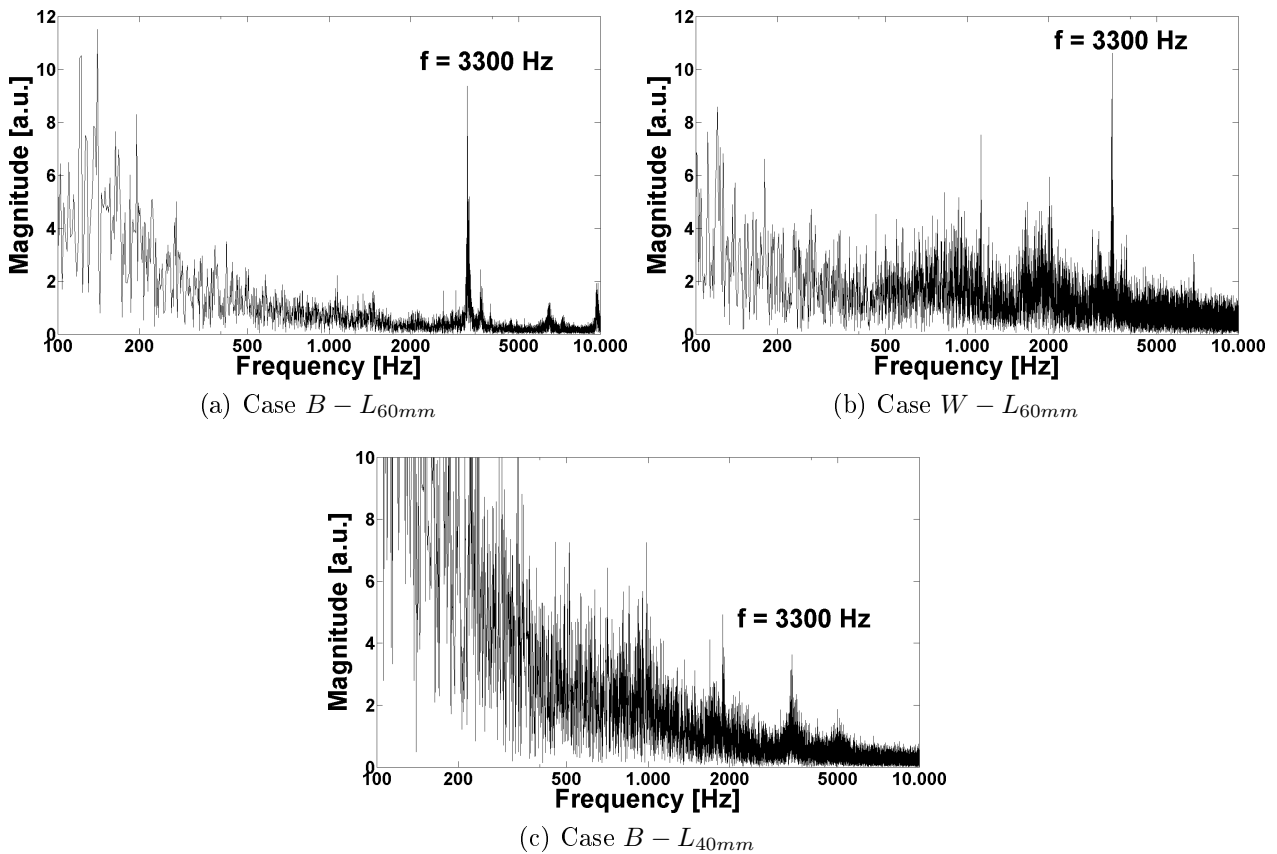


Figure 4.3.15: Power spectra of pressure signal at monitor point 12.

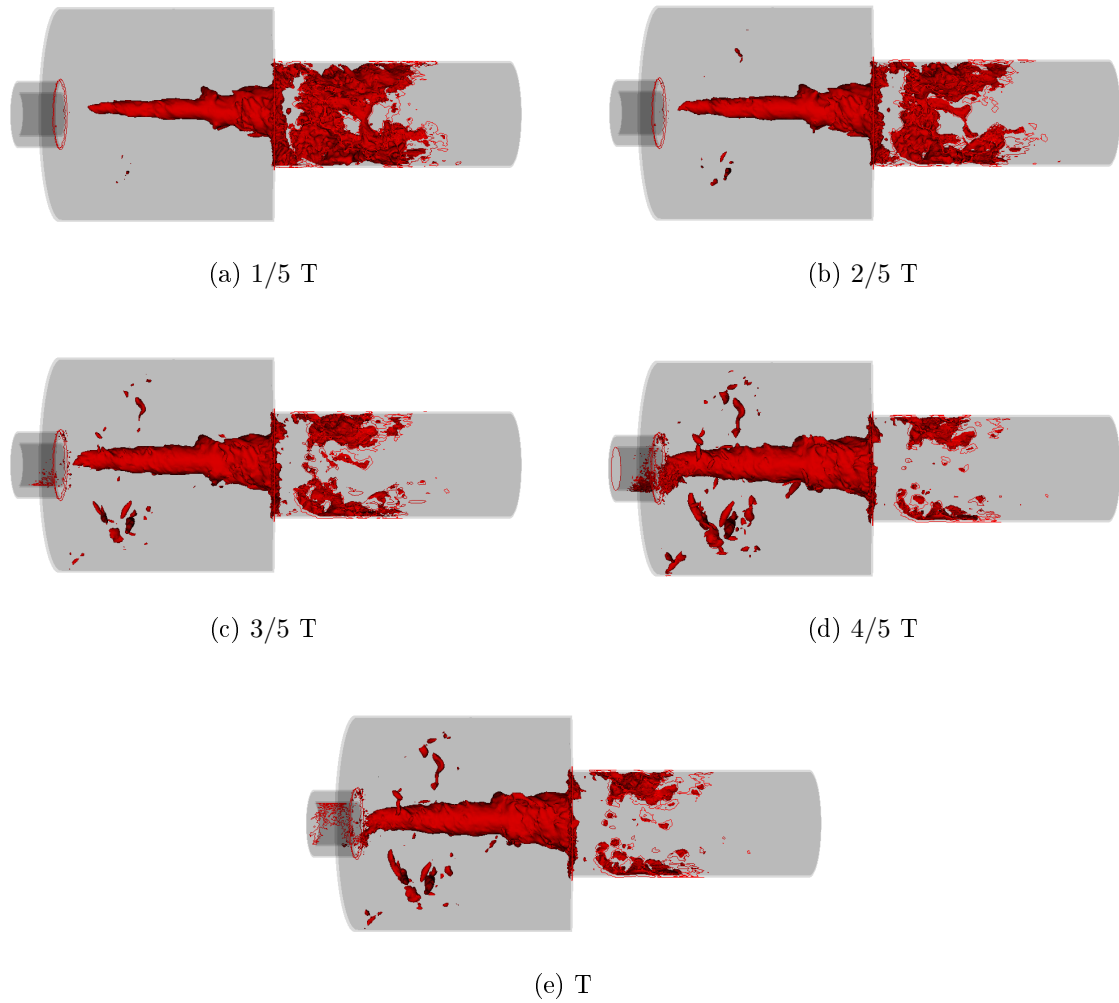


Figure 4.3.16: Case $B - L_{40mm}$. Development of the pressure isosurface at 500400 Pa over a period at $f = 3300$ Hz.

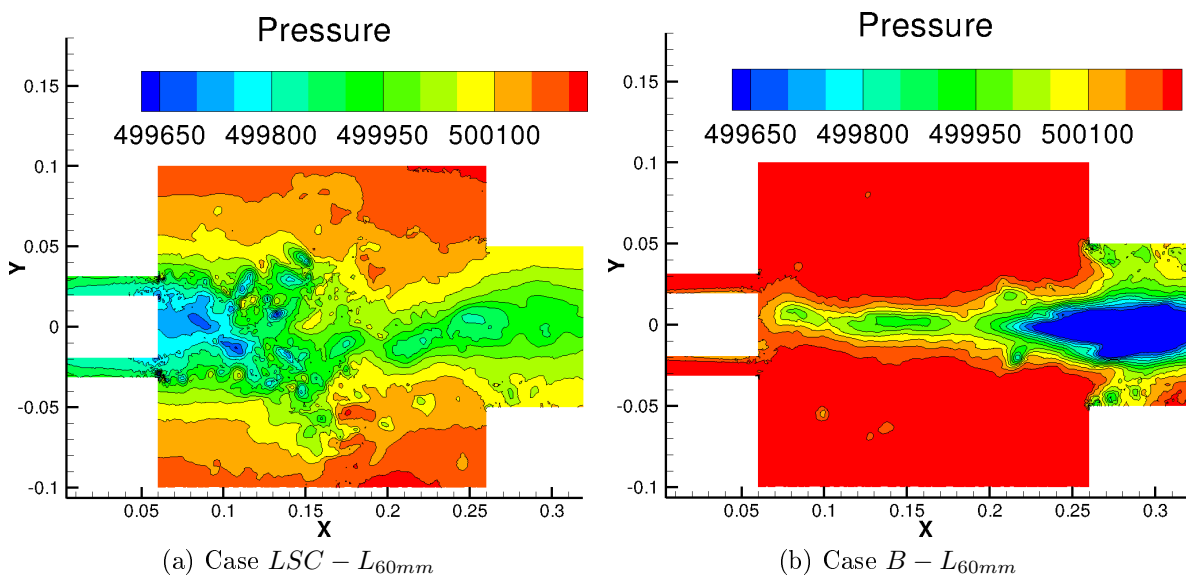


Figure 4.3.17: Instantaneous pressure field [Pa].

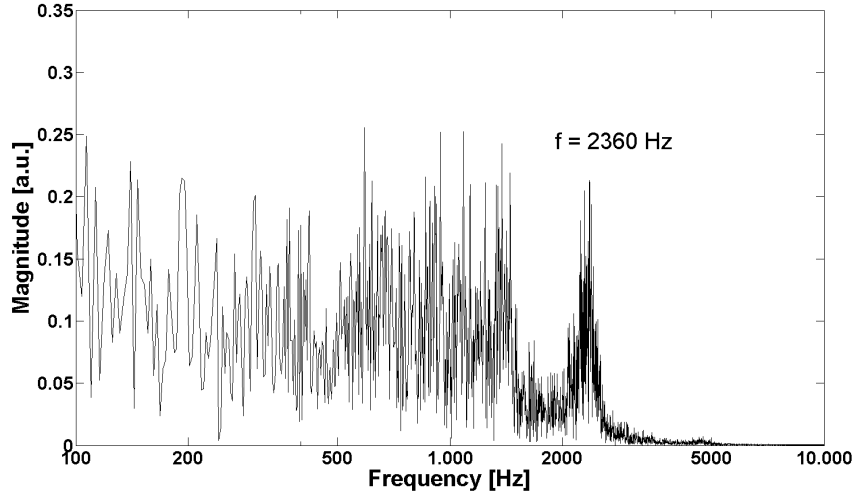


Figure 4.3.18: $LSC - L_{60mm}$: Power spectra of axial velocity signal at monitor point 1.

number: the boundary conditions of case $LSC - L_{60mm}$ were set to create a flow with swirl number $S = 0.37$, while case $B - L_{60mm}$ develops at $S = 0.9$. In case $LSC - L_{60mm}$ the shedding of vortices, which align both at the inner shear layer and outer shear layer, is clearly visible, while it disappears for case $B - L_{60mm}$. However, the analysis of the power spectra of both velocity components and pressure for case $LSC - L_{60mm}$ revealed that a coherent signal could be detected just directly after the dump plane, figure 4.3.18, while downstream in the chamber the Fourier analysis of time-dependent signals became very noisy. Indeed, when analyzing high frequency instabilities the order of magnitude of the length- and time-scales are close to the turbulent scales, this suggests that the noise shown by the FFT of the signals, registered downstream the combustion chamber, for case $LSC - L_{60mm}$ can be due to the overlapping effect of turbulence and high frequency oscillatory phenomena and not to a real disruption into a random flow of the coherent vortices developing at the dump plane. A method for scale distinction could enhance the quality of the results, enabling to keep the random turbulent signal distinct from a high frequency oscillation. Such a method, which is relying on triple decomposition method, will be treated in the following chapter.

5 The Triple Decomposition Method

The numerical simulation of combustion oscillations in general, and more specifically of high frequency instabilities, in highly turbulent flows requires the resolution of different time and length scales simultaneously.

The usual approach, as shown in Chapter 4, is to adopt LES or LES/RANS hybrid methods, therefore solving a large spectrum of scales. Moreover, for combustion modeling, it is crucial to take into account both turbulence-chemistry interaction as well as the chemical kinetic effects. Considering figure 5.0.1, this would mean solving the red dotted space. This leads to very high computational costs, which are mainly due to the wide range of structures, from very coarse to very fine, which must be resolved. It is also necessary to point out that part of the turbulent scales spectrum almost coincide with the scales of high frequency instabilities, leading to further difficulties in the interpretation of the results. In fact, in such situations, a simulation with conventional Reynolds Averaged Navier Stokes (RANS) method, which would be very cheap from the point of view of CPU-time, would not allow the distinction of the effects, with a consequent loss of information. In this chapter an alternative to the usual methods is presented: the different time and space scales are solved separately and influence each other through source and convective terms. The method requires a computational effort of the same order of magnitude of a normal unsteady RANS simulations, i.e. very low compared to LES or LES/RANS hybrid methods, see also sections 3.2.1, 3.2.2.

5.1 The Triple Decomposition Ansatz

The Triple Decomposition Method (TDM) is a splitting technique, in which the decomposition of the field variables recollects the phase-locking method used in the experimental practice. As already described by Reynolds and Hussain, [75], when measuring a coherent wave in a shear flow, the signal can be divided into a time averaged, a phase locked and a random signal. In this same way, for the numerical simulation, every independent field variable is split into a background time averaged, a coherent and a random component. Equation 5.1.1 can be therefore written for a general field variable ϕ .

$$\phi(\mathbf{x}, t) = \bar{\phi}(\mathbf{x}) + \tilde{\phi}(\mathbf{x}, t) + \phi'(\mathbf{x}, t) \quad (5.1.1)$$

In equation 5.1.1 the single terms can be formally described as follows:

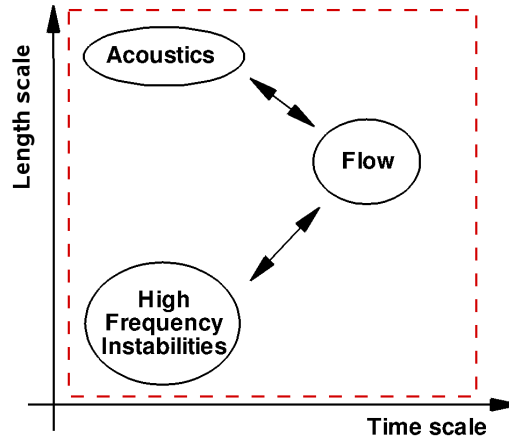


Figure 5.0.1: Schematic representation of time and length scales in a complex CFD simulation.

- $\bar{\phi}(\mathbf{x})$ is a time averaged quantity or mean field quantity, defined as:

$$\bar{\phi}(\mathbf{x}) = \lim_{T \rightarrow \infty} \frac{1}{T} \int_0^T \phi(\mathbf{x}, t) dt \quad (5.1.2)$$

- $\tilde{\phi}$ is a coherent motion developing in the mean field. Considering the variable $\phi(\mathbf{x}, t)$, its phase average is defined as follows

$$\langle \phi(\mathbf{x}, t) \rangle = \lim_{N \rightarrow \infty} \frac{1}{N} \sum_{n=0}^N \phi(\mathbf{x}, t + n\tau) \quad (5.1.3)$$

τ being the period of the wave traveling in the field. Therefore the coherent motion $\tilde{\phi}$ can be written as:

$$\tilde{\phi}(\mathbf{x}, t) = \langle \phi(\mathbf{x}, t) \rangle - \bar{\phi}(\mathbf{x}) \quad (5.1.4)$$

- ϕ' is a random quantity, e.g. turbulence

In the derivation of the modified Navier Stokes equations for TDM a first strong assumption has been made: the flow has been considered non reactive. The reason for this, is the difficulty to treat the splitting of density. In fact this leads to open terms, which need modeling for closure. On the other hand, for incompressible flows the splitting of temperature ensures that fluctuations in density caused by the heat variations are taken into account. Therefore the equations presented in the following can be further developed also for reactive but incompressible flows. Thus, assuming a non reactive, incompressible, single species flow and adopting pressure and velocity as independent variables, the governing equations, chapter 3, reduce to:

$$\frac{\partial u_j}{\partial x_j} = 0 \quad (5.1.5)$$

for the mass conservation equation and:

$$\frac{\partial u_i}{\partial t} + \frac{\partial (u_i u_j)}{\partial x_j} = -\frac{\partial p}{\partial x_i} + \frac{\partial}{\partial x_j} \left[\nu \left(\frac{\partial u_i}{\partial x_j} + \frac{\partial u_j}{\partial x_i} \right) \right] \quad (5.1.6)$$

for the momentum equation.

In order to obtain the new set of equations for the resolution of the time averaged field and of the coherent wave traveling through it, first equation 5.1.1 is substituted into the two above simplified equations and then further steps are done, which are highlighted in section 5.2. Throughout the derivation of this new set of equations some basic rules must be observed. In fact, considering two generic functions $f(\bar{x}, t)$ and $g(\bar{x}, t)$, when phase-averaging the following properties must be satisfied, [75][71][70].

$$\begin{aligned} \langle f' \rangle &= 0; & \langle \bar{f} \rangle &= \bar{f}; & \langle \tilde{f} \rangle &= \tilde{f}; \\ \langle \bar{f}g \rangle &= \bar{f} \langle g \rangle; & \langle \tilde{f}g \rangle &= \tilde{f} \langle g \rangle; \\ \langle \tilde{f}g' \rangle &= 0; & \langle \bar{f}g' \rangle &= 0 \end{aligned} \quad (5.1.7)$$

For time-averaging the following rules are applied.

$$\begin{aligned} \overline{\tilde{f}} &= 0; & \overline{\langle f \rangle} &= \bar{f}; \\ \overline{\tilde{f}g'} &= 0; & \overline{\bar{f}g} &= \bar{f}\bar{g} \end{aligned} \quad (5.1.8)$$

5.2 The TDM Equations

For the mass conservation equation the substitution of equation 5.1.1 into equation 5.1.5 and the subsequent phase averaging of the obtained equation yields:

$$\frac{\partial \bar{u}_j}{\partial x_j} + \frac{\partial \tilde{u}_j}{\partial x_j} = 0 \quad (5.2.1)$$

Time-averaging equation 5.2.1 results in

$$\frac{\partial \bar{u}_j}{\partial x_j} = 0 \quad (5.2.2)$$

which consequently leads to:

$$\frac{\partial \tilde{u}_j}{\partial x_j} = 0 \quad (5.2.3)$$

For the numerical resolution of the mean and tilde field, equation 5.2.1 guarantees that the two fields are inherently coupled.

The conservation equations for the momentum are obtained through the following steps:

- Equation 5.1.1 is substituted into the momentum equation, 5.1.6.

- The new equation is first phase-averaged and then time-averaged in order to obtain the Navier-Stokes equation for the time-averaged field.
- Consider again the equation obtained by substituting equation 5.1.1 into equation 5.1.6 and perform a phase-averaging, subtracting the Navier-Stokes equation for the time-averaged field from the phase-averaged equation leads to the Navier-Stokes equation for the field of the coherent oscillation.

Thus, the momentum conservation equation for the mean flow is:

$$\underbrace{\frac{\partial \bar{u}_j \bar{u}_i}{\partial x_j}}_A + \underbrace{\frac{\partial \bar{u}_j \bar{u}_i}{\partial x_j}}_B + \underbrace{\frac{\partial \bar{u}_j' u_i'}{\partial x_j}}_C = \underbrace{-\frac{1}{\rho} \frac{\partial \bar{p}}{\partial x_i}}_D + \underbrace{\frac{\partial}{\partial x_j} \left[\nu \left(\frac{\partial \bar{u}_i}{\partial x_j} + \frac{\partial \bar{u}_j}{\partial x_i} \right) \right]}_E \quad (5.2.4)$$

Equation 5.2.4 has the same form as the steady RANS formulation for the Navier Stokes equations but for term B. This partial derivative represents the effect of the coherent wave field on the mean field; it will be shown in section 5.4.2 that B constitutes the feedback term for the coupling of the momentum equations.

For the coherent wave the momentum conservation is ensured by the following equation:

$$\begin{aligned} & \underbrace{\frac{\partial \tilde{u}_i}{\partial t}}_A + \underbrace{\frac{\partial \tilde{u}_i \tilde{u}_j}{\partial x_j}}_B + \underbrace{\frac{\partial \tilde{u}_i \bar{u}_j}{\partial x_j}}_C + \underbrace{\frac{\partial \bar{u}_i \tilde{u}_j}{\partial x_j}}_D - \underbrace{\frac{\partial \bar{u}_i \bar{u}_j}{\partial x_j}}_E \\ & \quad + \underbrace{\frac{\partial}{\partial x_j} (\langle u_i' u_j' \rangle - \bar{u}_i' u_j')}_{F} \\ & = -\underbrace{\frac{1}{\rho} \frac{\partial \tilde{p}}{\partial x_i}}_G + \underbrace{\frac{\partial}{\partial x_j} \left[\nu \left(\frac{\partial \tilde{u}_i}{\partial x_j} + \frac{\partial \tilde{u}_j}{\partial x_i} \right) \right]}_H \end{aligned} \quad (5.2.5)$$

Confronting equation 5.2.5 with the unsteady RANS formulation of the Navier Stokes equation, some additional terms can be highlighted. Term C represents the convection of the coherent signal by means of the time averaged field, term D the convection of the mean field by the coherent oscillation, term E is equivalent to term B of equation 5.2.4 and it here has a negative sign. Finally term F represents the effect of the turbulent stresses.

5.3 Application of the Triple Decomposition Method

The equations presented in section 5.2 have already been used by Reynolds et al. [75], [34] as well as by Reau and Tumin, [71], [70], who reduced them to the Rayleigh equation to perform a linear stability analysis of perturbations in turbulent shear flows. Moreover Apte et al. [5] and Habisreuter, et al. [30] adopted the decomposition scheme to develop post processing tools

for scale decomposition in LES resolved fields, in order to selectively visualize and analyze particular frequency dependent structures in combustion chambers, decoupled from the turbulent background.

The following approach uses the equations in a complete new way, solving two separate fields, i.e. filtering coherent oscillations automatically from the turbulent stochastic background field.

5.4 A Solution Methodology

The equations presented in section 5.2 have been implemented in the DLR-THETA code,[3], see also section 4.1. The assumptions for the implementation were to consider an incompressible, non-reactive, single-species flow. Since it was desired to handle unsteady as well as steady simulations in the same way, it has been decided to approach the pressure-velocity coupling problem adopting the Semi-Implicit Method for Pressure-Linked Equations (SIMPLE) iterative scheme [67]. This section presents the original form of the algorithm and a modified version developed to solve the mean and the coherent flow field. Moreover, the further assumptions made for the numerical resolution of the TDM equations are presented.

5.4.1 The SIMPLE Algorithm

The SIMPLE algorithm is a pressure correction technique; figure 5.4.1 shows the flowchart of the algorithm in its original form, [67]. When running a steady simulation just the inner loop is performed. The convergence criterion is based on the continuity equation: as soon as the divergence of mass is zero, i.e. the velocity field satisfies the mass conservation equation, the end of the iterative inner loop is reached. The outer loop is controlled by the simulation time set by the user as a computation criterion.

5.4.2 The Time Marching Solution Strategy

The TDM solution is achieved by performing a time-marching simulation and is based on the SIMPLE algorithm. The flowchart in figure 5.4.2 presents the solution strategy adopted.

From the derivation of the governing equations for the TDM, as shown in equation 5.2.4, the mean field is formulated in steady state form, i.e. without time-term, though, for achieving a better convergence $\partial \bar{u}_i / \partial t$ is added and used as a relaxation term. It was ensured that the term reduces to zero as soon as convergence is reached. Furthermore for a fast convergence of the solution, it can be useful to initialize the mean field with an Unsteady Reynolds Averaged Navier Stokes (URANS) solution obtained without the TDM splitting. The decision of whether to run the loop for the mean or the coherent field succeeds based on a user-defined variable. The user of the THETA-code assigns the number of time-steps to run before switching from one field to the other. The time-development of the solution can be sketched as in figure 5.4.3. The number of time steps in the present work was set according to a trial and error procedure.

Moreover, both fields are simulated with the same time-step, which suffice for the resolution of the easy test-case adopted so far, see chapter 6; anyhow a possible enhancement would be to adopt two different time steps, with $d\tilde{t} < d\bar{t}$.

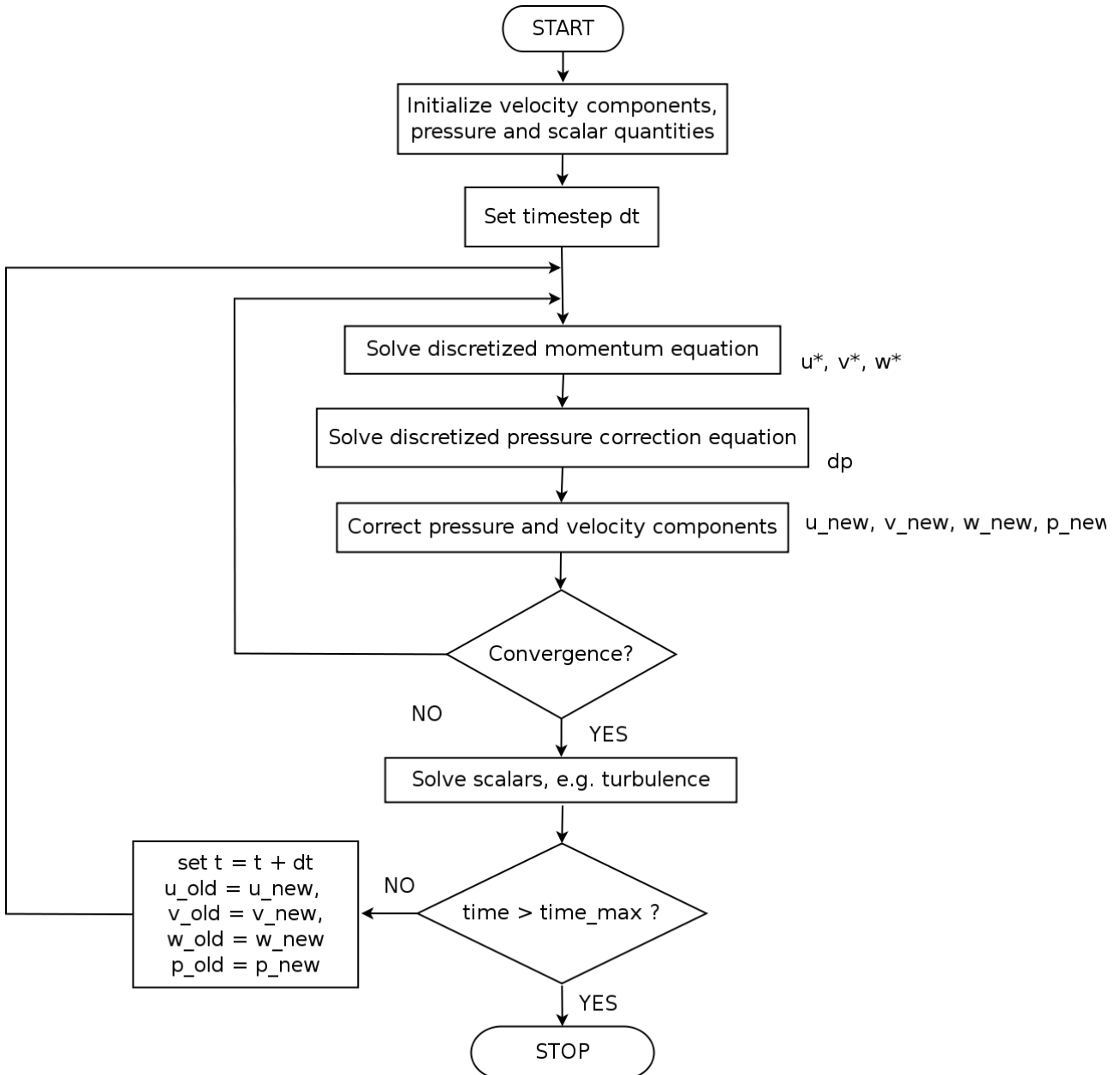


Figure 5.4.1: Flowchart of the SIMPLE algorithm.

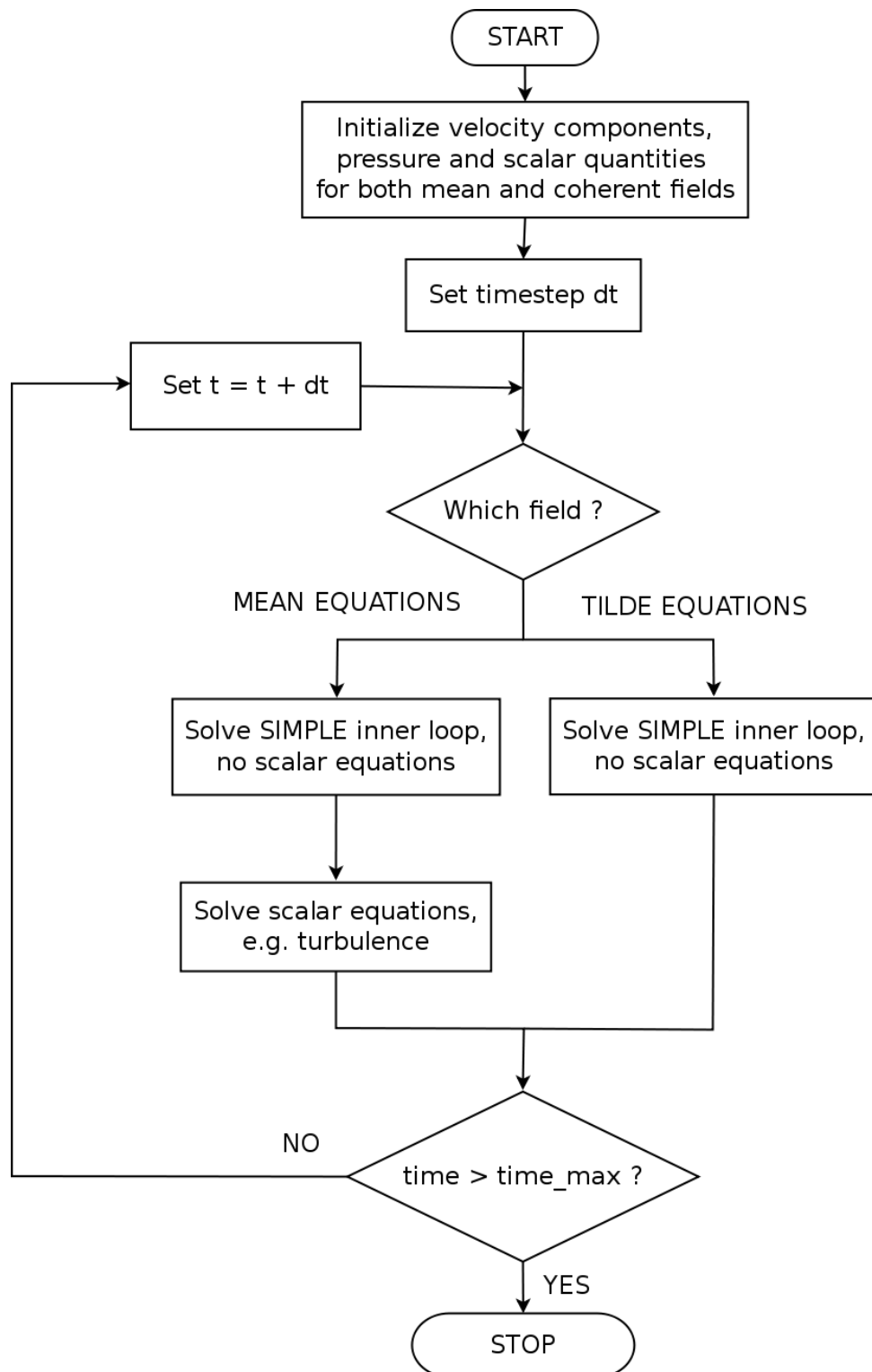


Figure 5.4.2: Flowchart of the solution strategy of the TDM equations.

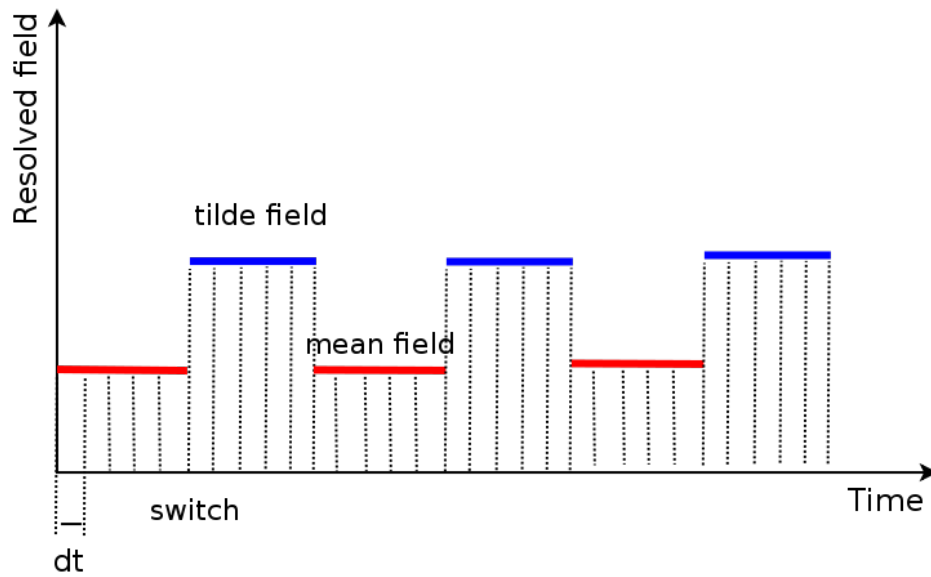


Figure 5.4.3: Time development of the solution.

The two fields are treated within two separate simple loops, when the mean field is resolved the coherent oscillation field is frozen and vice versa. The coupling of the two fields succeeds by means of the feedback term $\partial(\rho\overline{u_i\tilde{u}_j})/\partial x_j$, which appears in both momentum equations, 5.2.4 and 5.2.5, with opposed sign. Moreover, the coupling of the two fields is ensured by using the divergence of mass of the mean field acting as a mass source for the tilde field in the pressure correction equation and the other way around.

Since the final scope of the TDM equation was the simulation of high frequency instabilities, which are relatively small in comparison to the Kolgromov scale, the further assumption made was to consider the coherent oscillation as a laminar disturbance, therefore neglecting term F in equation 5.2.5. If the term needs to be considered, the Boussinesq hypothesis for modeling of the new Reynolds stress tensor can be adopted, as suggested by Reynolds et al. [75].

6 Verification of the Triple Decomposition Method

The capability of the triple decomposition method (TDM), based on the equations presented in Section 5.2, was tested by simulating the flow field around a square rod positioned in a channel perpendicularly to the flow field direction. The geometry, often addressed to as “square cylinder” in literature, is based upon that of the experimental measurements of Lyn, et al. [47]; this work has become a standard reference to the flow analysis around bluff bodies in turbulent flows. In fact, the experimental study of Lyn and coauthors is particularly significant because they adopted for their LDA measurements the triple decomposition method, and were therefore able to provide phase- or ensemble-averaged values for all relevant flow quantities describing the development of the flow past the obstacle.

The test-case suited the scope of the present analysis because of several reasons: it reveals a self-induced, periodic effect due to the shedding of vortical structures created from the detachment of the shear layer on the upper and lower edges of the square cylinder. These coherent structures arise without the application of any external forces and their frequency is directly dependent on the bluff body shape and Reynolds number [61]. Moreover, unlike for a cylinder, the separation point is fixed and independent of the shear layer thickness, [47], and therefore the flow can be more easily characterized.

Focus of the simulations performed and presented in section 6.2 is not the farfield wake structure and its development but the shedding of the vortical structures, i.e. the capability of the tilde field, section 5.2, equations 5.2.3 and 5.2.5 to capture the arising of such coherent structures.

6.1 The Square Cylinder Test Case

The square cylinder test case has been adopted by many researchers: it has been analyzed, in both experimental and numerical works, in channels exhibiting laminar flows [36], [16], [84] as well as turbulent flows, [79], [7]. Therefore the basic numerical set up, which would be able to reproduce the experiments of Lyn, et al. [47] was defined, following the findings of the other studies. In fact, particular attention must be focused on the computational domain chosen, in order to be able to assign block velocity boundary conditions at the inlet and to make sure that the outlet does not influence the computational field. Bosch, et al., [7], provided an analysis of the minimum computational field which must be simulated; assuming as scaling length the size of the square cylinder, D , the authors were able to demonstrate that in the standard

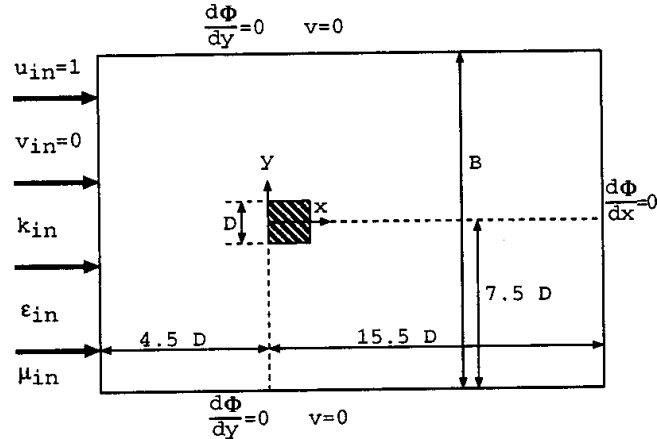


Figure 6.1.1: Original computational domain, as reported by Bosch et al., [7].

Reynolds Number	Free Stream Turbulence Level	Blockage	Aspect Ratio	Strouhal Number (Experiments [47])
21400	2 %	7%	9.75	0.13

Table 6.1: Main parameters for the square cylinder testcase.

configuration, figure 6.1.1, the flow field was still sensitive to the inlet, therefore they suggested to adopt a prolonged channel, where the inlet is at $x = -10 D$ to avoid the influence of the blockage of the square cylinder on the inlet. The blockage ratio of 7%, from the experiments of Lyn, et al. imposes the height of the channel. This configuration has been adopted in the present computations.

The general parameters for the simulation are summarized in table 6.1, the working fluid is water.

Turbulence modeling is a crucial point when simulating the square cylinder: already in the work of Franke and Rodi [26] it was evidenced that adopting different turbulence models influences the correct development of the vortical structures shed at the lower and upper edge of the square rod. In particular the authors found out that the standard $k - \epsilon$ formulation [42] strongly underpredicts the strength of the shedding motion, leading therefore to a larger recirculation zone behind the square cylinder. Bosch and Rodi [7] made a further step forwards and presented a comprehensive parametric analysis regarding turbulence modeling. They discovered that the size and the roll up strength of the vortical structures shed at the cylinder edges depend on the turbulence model adopted, and specifically on the near wall treatment of the turbulent quantities.

The simulations presented in section 6.2 are performed with a standard $k - \epsilon$ model; an attempt was made of simulating the shedding with a $k - \omega$ model, but the computation did not provide the arising and shedding of the vortices. In section 6.2 two different simulations are shown: at first a benchmark simulation with a standard URANS approach and a $k - \epsilon$ model for the turbulence closure. Furthermore, a second simulation with the TDM approach, i.e. solving the equations presented in chapter 5, was performed with the same computational parameters adopted for the benchmark simulation.

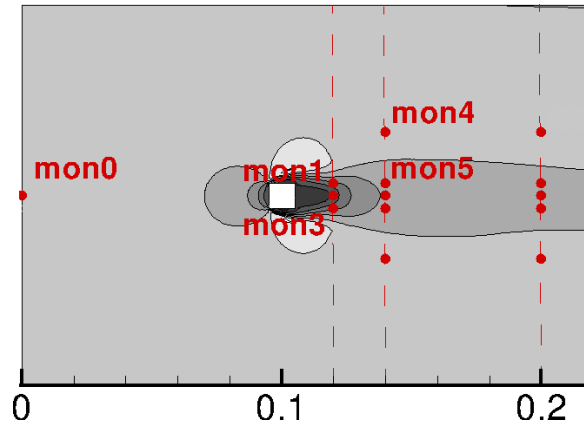


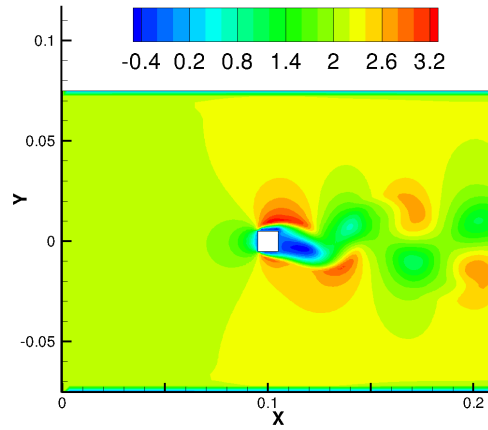
Figure 6.1.2: Monitoring points.

Finally for the simulation performed as a benchmark, i.e. without solving the TDM equations, the following boundary conditions were chosen: at the inlet a block velocity profile was adopted realizing a Reynolds number of 21400 and for the resolution of the turbulence, a turbulence degree of 2% and a turbulent length scale of 0.001 m were prescribed. At the outlet a constant pressure was imposed, walls boundary conditions ensured the proper treatment for the channel boundaries and for simulating the square cylinder. Moreover, the simulation was performed quasi two dimensional, so that periodic boundary conditions were applied at the upper and bottom boundaries of the domain. In the simulation solving the TDM equations, a set of boundary conditions needed to be applied for each field: while the boundary conditions for the mean field recollect those of the simulation without TDM, for the tilde field a zero velocity boundary condition was imposed at the inlet and no turbulence quantities prescribed, since it was supposed that the oscillations were small enough to be considered laminar. Moreover no turbulent wall law was imposed for the tilde field.

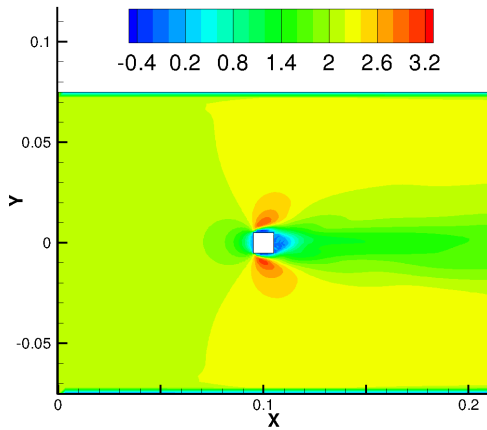
The computational field was equipped with monitor points for post-processing scope, these are evidenced in figure 6.1.2.

6.2 Results

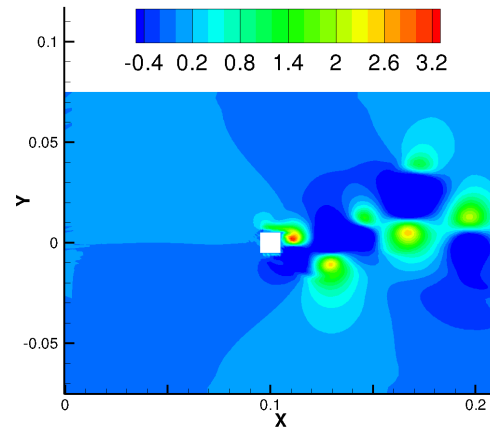
The instantaneous axial velocity field of the benchmark simulation, figure 6.2.1a, performed with a standard URANS approach and a $k-\epsilon$ model for the turbulence closure, shows the vortices arising from the edges of the square cylinder, which are transported downstream by means of convection. When simulating this same configuration by solving the set of equations given by the triple decomposition method (TDM), chapter 5, the solution is split in two distinctive fields: a mean, i.e. time-averaged field, and what is further on in this discussion called a tilde field, i.e. a computational domain containing just the coherent oscillation; these two partial solutions are shown in figures 6.2.1b and 6.2.1c respectively. The mean field, once convergence is reached, assumes a stable configuration which resembles that of the time-averaged axial velocity field obtained with the URANS simulation, figure 6.2.2. The tilde field, figure 6.2.1c is all over zero, but for the vortical structures initiated at the edges of the square cylinder. The transport of



(a) Simulation without TDM



(b) Simulation with TDM - Mean field



(c) Simulation with TDM - Tilde field

Figure 6.2.1: Instantaneous axial velocity field.

the vortices downstream the square cylinder succeeds through convection effects ensured by the mean field, which are represented by the term $\partial\tilde{u}_i\tilde{u}_j/\partial x_j$ in equation 5.2.5. Figure 6.2.1c shows a slightly asymmetry of the coherent axial velocity field, but the reason for this behavior could not be clarified in the present work.

The same features evidenced when confronting the instantaneous axial velocity field of the URANS and the TDM simulation can be observed in the comparison of the instantaneous y-velocity components, figure 6.2.3. It is interesting to notice that the mean field reports as expected the features of the steady flow, showing a local maximum and minimum at the edges of the square cylinder due to the separation of the flow after the impingement on the square cylinder. The tilde field on the other side, reproduces the positive and negative velocities downstream the square cylinder due to the transport of the vortical structures towards the outflow.

The convergence of the TDM solution could be proved analyzing the x- and y-component of the feedback term $\partial(\tilde{u}_i\tilde{u}_j)/\partial x_j$, which are reported in figures 6.2.4a and 6.2.4b respectively.

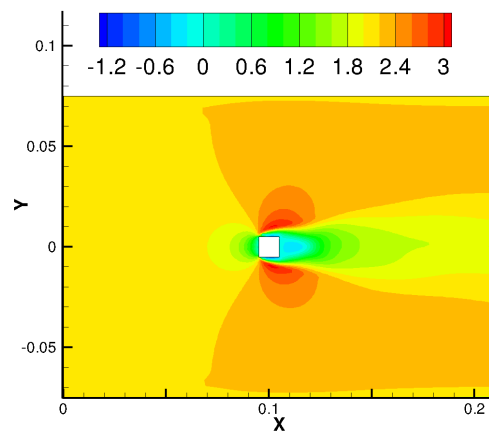
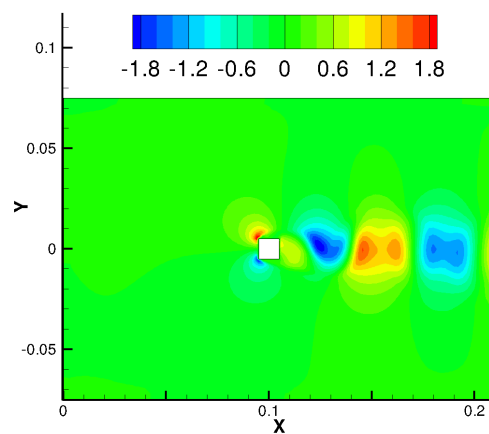
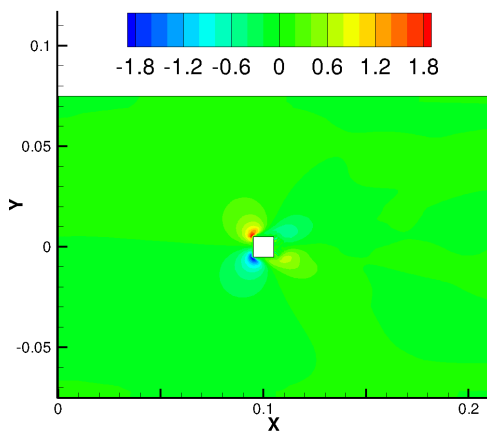


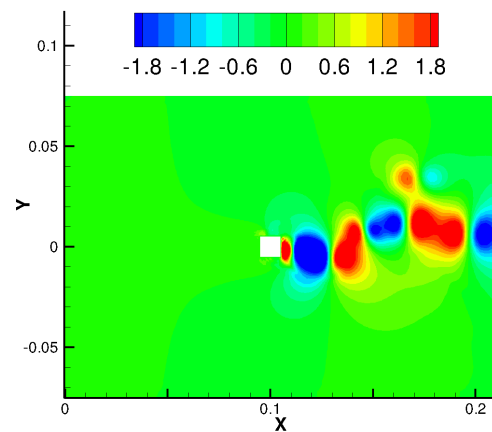
Figure 6.2.2: Simulation without TDM: Time-averaged axial velocity field.



(a) Simulation without TDM

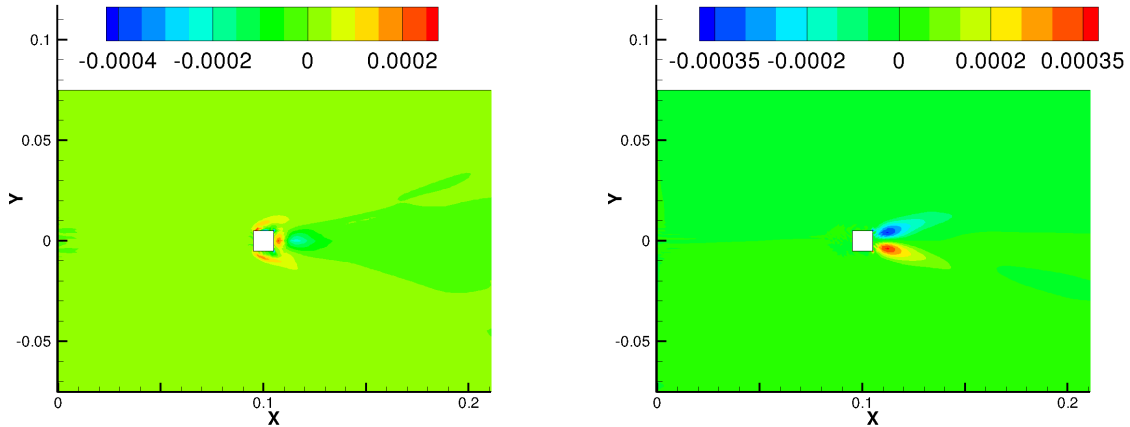


(b) Simulation with TDM - Mean field



(c) Simulation with TDM - Tilde field

Figure 6.2.3: Instantaneous Y-velocity field.



(a) Simulation with TDM - Feedback, axial direction (b) Simulation with TDM - Feedback, Y-direction

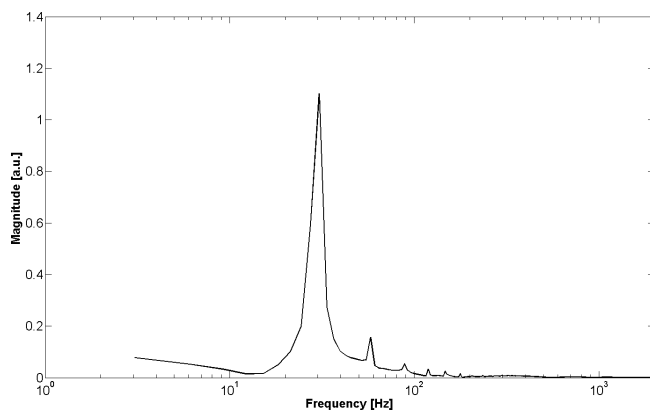
Figure 6.2.4: Feedback field at convergence.

Once the solution has reached convergence the two fields remain constant and are symmetric with respect to the middle of the square cylinder.

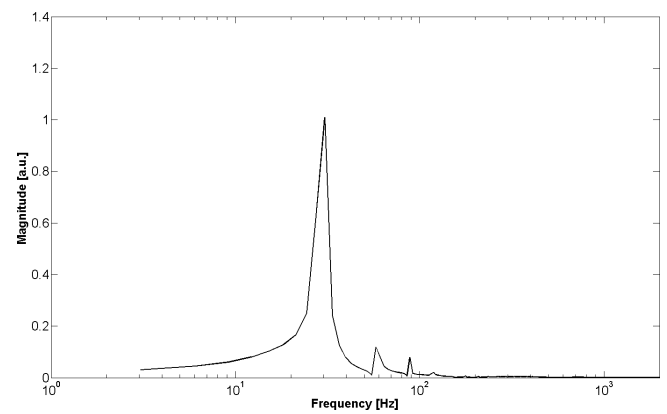
The Fast Fourier analysis (FFT) has been used to identify the frequency of the shedding; figure 6.2.5 shows the power spectra of the velocity components and of the pressure signal extracted at monitor point 1, i.e. 1.5 diameters behind the cylinder (figure 6.1.2) for the benchmark URANS simulation. All three quantities show a clear peak at 30 Hz, i.e. at a Strouhal number, $S = f_s D / U = 0.143$; this value is in good agreement with the experimental value $S = 0.134$ from the work of Lyn et al. [47]. A second peak at 58 Hz can be clearly seen in the magnitude spectrum of the pressure signal: this frequency is the pairing frequency of the vortices flowing downstream. In fact at monitor points 6, i.e. far away enough from the shedding points, the predominant frequency is the 58 Hz signal.

While the power spectra from the URANS benchmark simulation show clear peaks with no further harmonics, figure 6.2.5, those obtained from the tilde quantities of the TDM simulation, figure 6.2.6, recollect more the spectra of LES simulations known from literature, [58], [46].

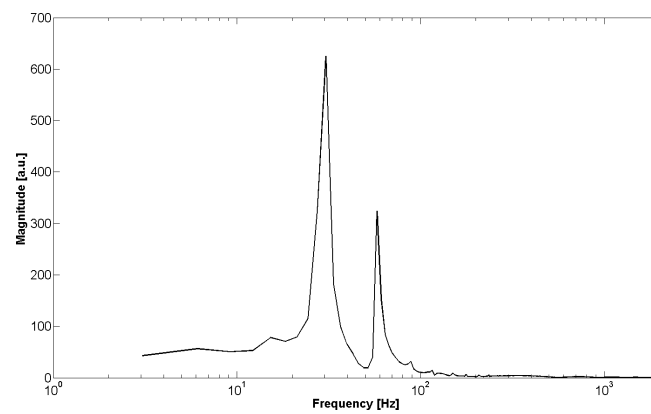
The x- and y- velocity components, registered at monitor point 1, show two slightly different frequency, i.e. 35 Hz and 39 Hz respectively, corresponding to $S = 0.163$ and $S = 0.182$; both values overestimate the frequency known from the experiments. The 39 Hz are to be seen in all y-velocity spectra for the different monitor points and are confidently considered the shedding frequency for the simulation with the TDM. The power spectra of pressure are rather controversial. The FFT of the pressure signal underestimate the shedding frequency dramatically. Murakami et al, [58] also observed unsatisfactory results for what concerns the pressure field when performing quasi 2D LES of the square cylinder; they found out that performing an LES on a fully 3 dimensional field enhances the capability of the simulation to predict the surface pressure field properly. A further hypothesis to explain the unsatisfactory behavior of the pressure field could be the choice of the test-case itself, in combination with the



(a) FFT of the axial velocity at monitor point 1

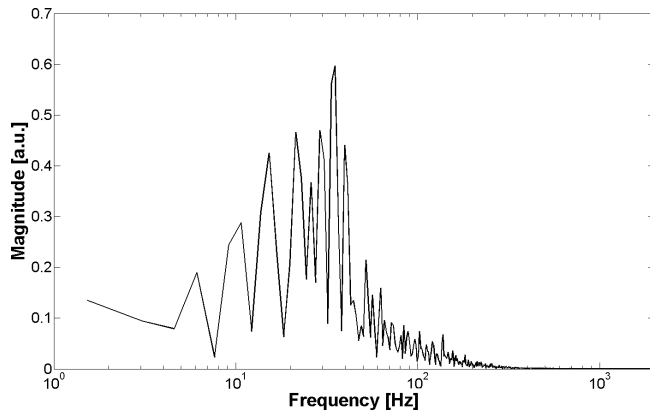


(b) FFT of the y-velocity at monitor point 1

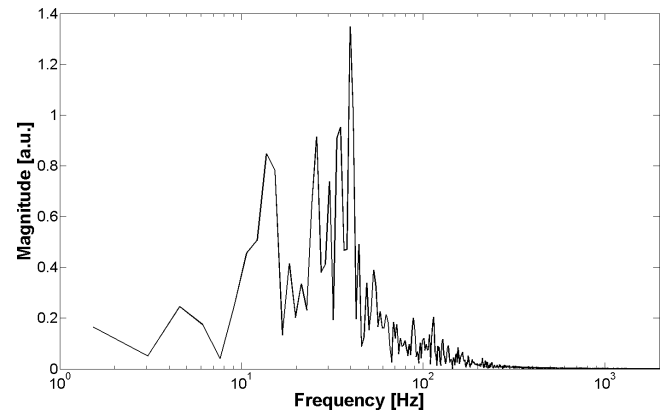


(c) FFT of pressure at monitor point 1

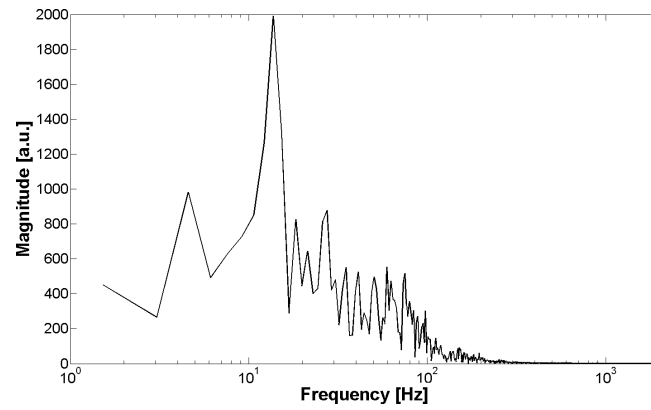
Figure 6.2.5: FFT of the benchmark simulation.



(a) FFT of the axial velocity at monitor point 1



(b) FFT of the y-velocity at monitor point 1



(c) FFT of pressure at monitor point 1

Figure 6.2.6: FFT of tilde field quantities from the TDM simulation.

hypothesis done when solving the set of equations derived from the TDM ansatz. As a matter of fact, the assumption that the tilde field can be considered laminar holds true just when the oscillation length- and time-scales are not of the same order of magnitude of those of the mean field. This is not properly the case for the square cylinder, since the scales of such hydrodynamic oscillation, like the vortex shedding from the edges of the square rod, are comparable with the scales of the mean flow. Still the test-case was able to highlight the capability of the two fields achieved with the TDM computation of reproducing intrinsic instabilities with a complete distinction between the mean turbulent flow and the coherent oscillating motion.

7 Conclusions

This work addresses three main issues; at first advanced CFD simulations were performed to demonstrate if nowadays turbulence and combustion models can capture highly unsteady three-dimensional combustion phenomena in technical relevant configurations. From the comparison of simulations and experimental data, it was possible to demonstrate that such advanced CFD calculations can reproduce the physics of both low and high frequency combustion instabilities. In general the numerical studies evidenced that the modeling approach shall be able to account for the influence of combustion on turbulence and vice versa, in order to obtain successful computations. In particular, the turbulence model shall resolve a large portion of the turbulent spectrum, as it is done by the hybrid LES/RANS (Large Eddy Simulation/ Reynolds Averaged Navier Stokes) model adopted in chapter 4 and the combustion model shall be complex enough to take into account, at least to a certain extent, the chemical kinetic aspects of the combustion process. In fact a relatively simple combustion model, like the EDM (Eddy Dissipation Model), can be enhanced by switching to a FRC (Finite Rate Chemistry) approach in the flame region and with this strategy already a three step mechanism gives very good results, see chapter 4. In the study concerning low frequent unsteady combustion phenomena, section 4.2, the turbulent field was deeply analyzed both by means of time averaged and RMS velocity components and was found in very good agreement with the experimental database. A sensitivity analysis on the combustion mechanism adopted highlighted the importance of correctly taking into account chemical kinetic effects and enabled an enhancement of the simulated temperature distribution and its fluctuations. Moreover the issue regarding the resolution of the turbulent flow was also analyzed in the numerical study on high frequency instabilities (HFI). The visualization of the resolved turbulence ratio in the computational domain evidenced how the hybrid LES/RANS modeling technique resolves large parts of the turbulent structures. A direct confrontation of the flow field simulated with the hybrid LES/RANS approach and with a URANS approach showed the loss of information on the small unsteady structures with this latest approach.

The second question approached in this work concerned the phenomenology of combustion oscillation both at high and low frequencies. Relying on the simulations performed, the unstable behavior of a flame next to lean blow out (LBO) was successfully investigated. The simulation correctly reproduced the frequency peaks spread at low frequencies, in this case 150 Hz, due to the highly unsteady character of the flame; in fact, local disruption of the flame sheet could be observed and was in good agreement with the experiments. The simulation reproduced also a thermo-acoustic instability; the precessing vortex core structure could be identified and the entrainment of fresh mixture in the large vortical structures, which convect downstream the

chamber, could be successfully visualized. Moreover, a high frequency combustion oscillation could be successfully simulated and therefore it was possible to suggest a mechanism, which is likely to be responsible for the arising of such instabilities: this is based on the heat exchange between flame root and combustor dump plane. In this case the resolution of the chemical kinetic effects was crucial, since the fluctuations in the main species causes the self-sustenance of the instability, section 4.3.

Both numerical studies performed on combustion instabilities were very expensive in terms of CPU times and the simulations could anyhow just have been performed on supercomputers. Therefore, a third question has been addressed in this dissertation: with focus on not time-consuming approaches, an alternative method, the so called Triple Decomposition Method (TDM) has been investigated, chapter 5. The independent variables for the flow field were split in a time-averaged, a coherent and a random part and introduced in the conservation laws to obtain a new set of equations, following the work of Reynolds et al. [75]. This new set of equations was implemented in the DLR-THETA code adopting a modified SIMPLE solution strategy, section 5.4. The verification of the method, chapter 6, demonstrated that the TDM approach is able to reproduce coherent structures in turbulent flows and overcome the lack of scale resolution, which is intrinsic in the Unsteady Reynolds Averaged Navier Stokes (URANS) approach. This suggests that the TDM could be further enhanced and used for the simulation of high frequency instabilities in gas turbines combustion chambers.

Bibliography

- [1] Cantera. Website. URL <http://www.cantera.org>. last visited on September 11th, 2008.
- [2] *CFX-Solver Theory Guide - Ansys*. www.ansys.com, 11.0 edition.
- [3] THETA Reference Guide. DLR internal document, 2011.
- [4] J. D. Anderson. *Computational fluid dynamics: basics with applications*. McGraw-Hill series in mechanical engineering - McGraw-Hill series in aeronautical and aerospace engineering. McGraw-Hill, 1995.
- [5] S. Apte and V. Yang. Unsteady flow evolution in porous chamber with surfeca mass injection, part 2: acoustic excitation. *AIAA Journal*, 40(2):244–253, February 2002.
- [6] T. Barth and D. Jespersen. The design and application of upwind schemes on unstructured meshes. In *AIAA, Aerospace Sciences Meeting, 27 th, Reno, NV*, 1989.
- [7] G. Bosch and W. Rodi. Simulation of vortex shedding past a square cylinder with different turbulence models. *International journal for numerical methods in fluids*, 28:601–616, 1998.
- [8] I. Boxx, C. Heeger, R. Gordon, B. Böhm, M. Aigner, A. Dreizler, and W. Meier. Simultaneous three component piv / oh-plif measurements of a turbulent lifted, c3h8-argon jet-flame at (sustained) 1.5 khz repetition rate. *Proceedings of the Combustion Institute*, 32:905–912, 2009.
- [9] I. Boxx, M. Stöhr, C. Carter, and W. Meier. Temporally resolved planar measurements of transient phenomena in a partially pre-mixed swirl flame in a gas turbine model combustor. *Combustion and Flame*, 157:1510–1525, 2010.
- [10] W. Bräuling. *Flugzeugtriebwerke*. Springer Verlag, 2001.
- [11] H. Büchner. *Strömungs- und Verbrennungsinstabilitäten in technischen Verbrennungssystemen*. Habilitationsschrift, 2000.
- [12] S. Candel. Combustion dynamics and control: progress and challenges. In *Proceedings of the Combustion Institute*, volume 29, pages 1–28, 2002.

- [13] L. T. Chong, S. Bomberg, A. Ulhaq, T. Komarek, and W. Polifke. Comparative validation study on identification of premixed flame transfer function. In *Proceedings of ASME Turbo Expo 2011*, number GT2011-46342, 2011.
- [14] A. Chorin. Numerical solution of Navier-Stokes equations. *Mathematics of computation*, 22(104):745, 1968.
- [15] L. Crocco and S. Cheng. *Theory of combustion instability in liquid propellant rocket motors*. Butterworths Scientific Publications, 2 edition, 1957.
- [16] R. W. Davis, E. F. Moore, and L. P. Purtell. A numerical-experimental study of confined flow around rectangular cylinders. *Physics of Fluids*, 27(1):46–59, January 1984.
- [17] M. Di Domenico, P. Le Clercq, and M. Rachner. Numerical simulation of unsteady, multi-phase flows in an aero-engine like combustor. In *ISABE 2011*, number 1101, 2011.
- [18] Massimiliano Di Domenico, Peter Gerlinger, and Berthold Noll. Numerical simulations of confined, turbulent, lean, premixed flames using a detailed chemistry combustion model. In *Proceedings of ASME Turbo Expo 2011, GT 2011*, June 2011.
- [19] V. Di Sarli, F. S. Marra, and A. Di Benedetto. Spontaneous oscillations in lean premixed combustors: Cfd simulation. *Combust. Sci. and Tech.*, 179:2335–2359, 2007.
- [20] N. Docquier and S. Candel. Combustion control and sensors: a review. *Progress in Energy and Combustion Science*, 28:107–150, 2002.
- [21] A. P. Dowling and S. R. Stow. Acoustic analysis of gas turbine combustion. *Journal of propulsion and power*, 19(5):751–764, September 2003.
- [22] X.R. Duan, P. Weigand, W. Meier, O. Keck, W. Stricker, M. Aigner, and B. Lehmann. Experimental investigations and laser based validation measurements in a gas turbine model combustor. *Progress in Computational Fluid Dynamics*, 4(3-5):175–182, 2004.
- [23] G. Eggenspieler and S. Menon. Combustion and emission modelling near lean blow-out in a gas turbine engine. *Progress in Computational Fluid Dynamics*, 5(6):281–297, 2005.
- [24] J. H. Ferziger and M. Peric. *Computational methods for fluid dynamics*. Springer Verlag, 1997.
- [25] A. Fiolitakis. Private communication. 15 April 2011.
- [26] R. Franke and W. Rodi. Calculation of vortex shedding past a square cylinder with various turbulence models. *Turbulent Shear Flows*, 8:189–204, 1993.
- [27] P. Gerlinger. *Numerische Verbrennungssimulation: : Effiziente Numerische Simulation Turbulenter Verbrennung*. Springer, 2005.

- [28] N. Gourdain, L. Gicquel, M. Montagnac, O. Vermorel, M. Gazaix, G. Staffelbach, M. Garcia, J.F. Boussuge, and T. Poinsot. High performance parallel computing of flows in complex geometries: I. methods. *Computational Science & Discovery*, 2(1):015003, 2009.
- [29] O. S. Graham and A. P. Dowling. Low-order modelling of ducted flames with temporally varying equivalence ratio in realistic geometries. In *Proceedings of ASME Turbo Expo 2011*, number GT2011-45255, 2011.
- [30] P. Habisreuter, P. Lischer, W. Cai, W. Krebs, N. Zarzalis, and H. Bockhorn. Visualisation of statistically periodic coherent structures in turbulent flows using a phaselocked averaging method. *Progress in Computational Fluid Dynamics*, 8(5):276–287, 2008.
- [31] J. Hermann and S. Hoffmann. *Combustion instabilities in gas turbine engines: operational experience, fundamental mechanisms, and modelling*, volume 210 of *Progress in astronautics and aeronautics*, chapter 19 - Implementation of active control in a full-scale gas-turbine combustor, pages 611–634. American institute of aeronautics and astronautics edition, 2005.
- [32] Y. Huang and V. Yang. Dynamics and stability of lean-premixed swirl-stabilized combustion. *Progress in Energy and Combustion Science*, 35:293–364, 2009.
- [33] Y. Huang, S. Wang, and V. Yang. *Combustion instabilities in gas turbine engines: operational experience, fundamental mechanisms, and modelling*, volume 210 of *Progress in astronautics and aeronautics*, chapter 10 - Flow and flame dynamics of lean premixed swirl injectors. American institute of aeronautics and astronautics edition, 2005.
- [34] A. K. M. F. Hussain and W. C. Reynolds. The mechanics of an organized wave in turbulent shear flow. *J. Fluid Mech.*, 41:241–258, 1970.
- [35] M. C. Janus, G. A. Richards, M. J. Yip, and E. H. Robey. Effects of ambient conditions and fuel composition on combustion stability. In *International gas turbine & aeroengine congress & exhibition, Orlando, Florida*, number 97-GT-266. ASME, 2 June 1997.
- [36] K. M. Kelkar and S. V. Patankar. Numerical prediction of vortex shedding behind a square cilinder. *International Journal for Numerical Methods in Fluids*, 14(6):327–341, 1992.
- [37] J.J. Keller. Thermoacoustic Oscillations in Combustion Chambers of Gas Turbines. *AIAA Journal*, 13(12):2280–2287, December 1995.
- [38] K. A. Kemenov and S. Menon. Explicit small-scale velocity simulation for high-Re turbulent flows. *Journal of Computational Physics*, 220:290–311, 2006.
- [39] W. Krebs, S. Bethke, J. Lepers, and P. Flohr. Thermoacoustic Design Tools and Passive Control: Siemens Power Generation Approaches. *Progress in Astronautics and Aeronautics*, 210(89-112), 2005.

- [40] K. K. Kuo. *Principles of combustion*. John Wiley and Sons, Inc, 2nd edition, 2005.
- [41] B. E. Launder and D. B. Spalding. Mathematical models of turbulence. *Academic Press - New York*, 1972.
- [42] B. E. Launder and D. B. Spalding. The Numerical Computation of Turbulent Flows. *Computer Methods in Applied Mechanics and Engineering*, 3:269–289, 1974.
- [43] W. Lazik, Th. Doerr, S. Bake, R. Bank, and L. Rackwitz. Development of a lean-burn low NOx combustion technology at Rolls-Royce Deutschland. In *ASME*, number GT2008-51115, 2008.
- [44] A. H. Lefebvre. *Gas Turbine Combustion*. Taylor & Francis, 2 edition, 1999.
- [45] T. C. Lieuwen and V Yang. *Combustion instabilities in gas turbine engines*, volume 210 of *Progress in Astronautics and Aeronautics*. American Institute of Aeronautics and Astronautics, Inc., 2005.
- [46] T.-M. Liou, S.-H. Chen, and P.-W. Hwang. Large eddy simulation of turbulent wake behind a square cylinder with a nearby wall. *Journal of Fluids Engineering*, 124:81–90, 2002.
- [47] D. A. Lyn and W. Rodi. The flapping shear layer formed by flow separation from the forward corner of a square cylinder. *Journal of Fluid Mechanics*, 267:353–376, 1994.
- [48] B. F. Magnussen. The eddy dissipation concept a bridge between science and technology. In *ECCOMAS Thematic Conference on Computational Combustion*, Lisbon (Portugal), 24 June 2005.
- [49] M. Matalon. Intrinsic flame instabilities in premixed and nonpremixed combustion. *Annual Review of Fluid Mechanics*, 39:163–191, 2007.
- [50] W. Meier, X. R. Duan, and P. Weigand. Investigation of swirl flames in a gas turbine model combustor. II. Turbulence-chemistry interaction. *Combustion and Flame*, 144: 225–236, 2006.
- [51] W. Meier, P. Weigand, X. R. Duan, and R. Giezendanner-Thoben. Detailed characterization of the dynamics of thermoacoustic pulsations in a lean premixed swirled flame. *Combustion and Flame*, 150:2–26, 2007.
- [52] W. Meier, I. Boxx, M. Stöhr, and C. D. Carter. Laser-based investigations in gas turbine model combustors. *Experiments in Fluids*, 49:865–882, 2010.
- [53] F. R. Menter. Two equation eddy viscosity turbulence models for engineering applications. *AIAA Journal*, 32(8):269–289, 1994.

- [54] F. R. Menter and Y. Egorov. Revisiting the turbulent scale equation. In *IUTAM Symposium; One Hundred Years of Boundary Layer Research*, Goettingen, 2004.
- [55] F. R. Menter and Y. Egorov. A scale-adaptive simulation model using two-equation models. In *43rd AIAA Aerospace Sciences Meeting and Exhibit*, 10 January 2005.
- [56] K. Midgley, A. Spencer, and J. J. McGuirk. Unsteady flow structures in radial swirler fed fuel injectors. In *Proceedings of ASME Turbo Expo 2004*, number GT2004-53608, 17 June 2004.
- [57] H. C. Mongia, T. J. Held, G. C. Hsiao, and R. P. Pandalai. *Combustion Instabilities in Gas Turbine Engines*, volume 210 of *Progress in Astronautics and Aeronautics*, chapter 3 - Incorporation of Combustion Instability Issues into Design Process: GE Aeroderivative and Aero Engines Experience, pages 43–63. American Institute of Aeronautics and Astronautics, Inc., 2005.
- [58] S. Murakami and A. Mochida. On turbulent vortex shedding flow past 2D square cylinder predicted by CFD. *Journal of Wind Engineering and Industrial Aerodynamics*, 54/55: 191–211, 1995.
- [59] D. G. Nicol, P. C. Malte, A. J. Hamer, R. J. Roby, and R. C. Steele. Development of a Five-Step Global Methane Oxidation-NO Formation Mechanism for Lean- Premixed Gas Turbine Combustion. *Journal of Engineering for Gas Turbines and Power*, 121:272–280, April 1999.
- [60] B. Noll, H. Schütz, and M. Aigner. Numerical simulation of high-frequency flow instabilities near an airblast atomizer. In *ASME TURBO EXPO 2001*, number 2001-GT-0041, 2001.
- [61] A. Okajima. Strouhal numbers of rectangular cylinders. *J. Fluid Mech.*, 123:379–398, 1982.
- [62] D. Panara. *Boundary Layer Response to Combustion Instabilities and Associated Heat Transfer*. PhD thesis, Universität Stuttgart, 2009.
- [63] C. O. Paschereit and E. Gutmark. Passive combustion control applied to premix burners. In AIAA, editor, *40th AIAA Aerospace Science Meeting and Exhibit*, number 2002-1007, January 2002.
- [64] C. O. Paschereit and E. Gutmark. Combustion instabilities and emission control by pulsating fuel injection. *Journal of Turbomachinery*, 130, January 2008.
- [65] C. O. Paschereit and E. J. Gutmark. Control of High-Frequency Thermoacoustic Pulsations by Distributed Vortex Generators. *AIAA Journal*, 44(3):550–557, March 2006.

- [66] C. O. Paschereit, E. Gutmark, and W. Weisenstein. Coherent structures in swirling flows and their role in acoustic combustion control. *Physics of Fluids*, 11(9):2667–2678, September 1999.
- [67] S. V. Patankar. *Numerical heat Transfer and Fluid Flow*. hemisphere Publ. Corp, 1980.
- [68] T. Poinso and D. Veynante. *Theoretical and Numerical Combustion*. Edwards, Philadelphia, 2001.
- [69] S. B. Pope. *Turbulent Flows*. Cambridge University Press, 2000.
- [70] N. Reau and A. Tumin. Harmonic perturbations in turbulent wakes. *AIAA Journal*, 40(3):526, March 2002.
- [71] N. Reau and A. Tumin. On harmonic perturbations in a turbulent mixing layer. *European Journal of Mechanics/Fluids*, 21(2):143–155, 2002.
- [72] F. Rebosio, M. Di Domenico, B. Noll, A. Meyer, H. Büchner, and M. Aigner. Numerical Simulation of Flow and Combustion of a Laminar Multiple Port Burner Using Detailed Chemistry. *Proc. 3rd European Combustion Meeting 2007*, 2007.
- [73] F. Rebosio, A. Widenhorn, B. Noll, and M. Aigner. Numerical simulation of a gas turbine model combustor operated near the lean extinction limit. In *Proceedings of ASME Turbo Expo 2010*, number GT2010-22751, 2010.
- [74] F. Rebosio, M. Di Domenico, B. Noll, and M. Aigner. Numerical analysis of combustion instability mechanisms in a lean premixed can combustor. In *49th AIAA Aerospace Sciences Meeting Including the New Horizons Forum and Aerospace Exposition*, January 2011.
- [75] W. C. Reynolds and A. K. M. F. Hussain. The mechanics of an organized wave in turbulent shear flow. Part 3. theoretical models and comparisons with experiments. *J. Fluid Mech.*, 6:263–288, 1972.
- [76] G. A. Richards and M. C. Janus. Characterization of oscillations during premix gas turbine combustion. *J. Eng. Gas Turbines Power*, 120(2294), 1998.
- [77] G. A. Richards and D. L. Straub. *Combustion instabilities in gas turbine engines: operational experience, fundamental mechanisms, and modelling*, volume 210 of *Progress in astronautics and aeronautics*, chapter 17 - Passive Control of Combustion Instabilities in Stationary Gas Turbines, pages 533–579. American Institute of Aeronautics and Astronautics, Inc., american institute of aeronautics and astronautics edition, 2005.
- [78] G. A. Richards, R. S. Gemmen, and M. J. Yip. A test device for premixed gas turbine combustion oscillations. *ASME journal of engineering for gas turbines and power*, 119:776–782, 1997.

- [79] W. Rodi. Comparison of LES and RANS calculations of the flow around bluff bodies. *Journal of wind engineering and industrial aerodynamics*, (69-71):55–75, 1997.
- [80] R. Sadanandan, M. Stoehr, and W. Meier. Simultaneous oh-plif and piv measurements in a gas turbine model combustor. *Applied Physics B*, 90:609–618, 2008.
- [81] J. B. Sewell and P. A. Sobieski. *Combustion instabilities in gas turbine engines: operational experience, fundamental mechanisms, and modelling*, volume 210 of *Progress in astronautics and aeronautics*, chapter 7 - Monitoring of combustion instabilities: Calpine’s Experience, pages 147–162. American institute of aeronautics and astronautics edition, 2005.
- [82] S. J. Shanbhogue, S. Husain, and T. Lieuwen. Lean blowoff of bluff body stabilized flames: Scaling and dynamics. *Progress in Energy and Combustion Science*, 35:98–120, 2009.
- [83] G. P. Smith, D. M. Golden, M. Frenklach, N. W. Moriarty, B. Eiteneer, M. Goldenberg, C. T. Bowman, R. K. Hanson, S. Song, W. C. Gardiner, V. V. Lissianski, and Z. Qin. Gri-mech 3.0. Website. URL http://www.me.berkeley.edu/gri_mech/. last visited on April 15th 2011.
- [84] A. Sohankar, C. Norberg, and L. Davidson. Low-Reynolds-Number flow around a square cylinder at incidence: study of blockage, onset of vortex shedding and outlet boundary condition. *Internationa Journal of Numerical Methods in Fluids*, 26:39–56, 1998.
- [85] A. Steinberg, I. Boxx, M. Stöhr, C. D. Carter, and W. Meier. Flow-flame interactions causing acoustically coupled heat release fluctuations in a thermo-acoustically unstable gas turbine model combustor. *Combustion and Flame*, 2010.
- [86] M. Stöhr and W. Meier. Coherent structures in partially premixed swirling flames. In *12th International Symposium on Flow Visualization*, 10 September 2006.
- [87] M. Stöhr and W. Meier. Investigation of a Periodic Combustion Instability in a Swirl Burner Using Phase-Resolved PIV. In *3rd European Combustion Meeting ECM 2007*, 2007.
- [88] M. Stöhr, I. Boxx, C. Carter, and W. Meier. Dynamics of lean blowout of a swirl-stabilized flame in a gas turbine model combustor. *Proceedings of the Combustion Institute*, 33(2): 2953–2960, 2011.
- [89] Michael Stöhr. Private communication. 27 April 2011.
- [90] K. Truffin. Modelling of methane/air flames using detailed and reduced kinetic schemes. Rapport de stage de D.E.A. WN/CFD/01-014, CERFACS, July 2001.

- [91] C. O. U. Umeh, Z. Rusak, and E. J. Gutmark. Experimental study of reaction and vortex breakdown in a swirl stabilized combustor. In *Proceedings of ASME Turbo Expo 2009*, number GT2009-60183, 12 June 2009.
- [92] C. Wagner, T. Hüttl, and P. Sagaut. *Large-eddy simulation for acoustics*. Cambridge University Press, 2007.
- [93] J. Warnatz, U. Maas, and R. Dibble. *Verbrennung*. Springer Verlag, 3rd edition edition, 2001.
- [94] P. Weigand. *Untersuchung periodischer Instabilitäten von eingeschlossenen turbulenten Drallflammen mit Lasermessverfahren*. PhD thesis, Institut fuer Verbrennungstechnik der Luft- und Raumfahrt an der Universitaet Stuttgart, Germany, 2007.
- [95] P. Weigand, W. Meier, X. R. Duan, W. Stricker, and M. Aigner. Investigation of swirl flames in a gas turbine model combustor. I. Flow field, structures, temperature and species distribution. *Combustion and Flame*, 144:205–224, 2006.
- [96] C. K. Westbrook, Y. Mizobuchi, T. J. Poinso, P. J. Smithd, and J. Warnatz. Computational combustion. *Proceedings of the Combustion Institute*, 30:125–157, 2005.
- [97] A. Widenhorn, B. Noll, M. Stoehr, and M. Aigner. Numerical Investigation of a Laboratory Combustor Applying Hybrid RANS-LES Methods. In *DESider 2007: Second Symposium on Hybrid RANS-LES Methods*, Corfu (Greece), 17 June 2007.
- [98] A. Widenhorn, B. Noll, and M. Aigner. Numerical study of a non-reacting turbulent flow in a gas turbine model combustor. In *47th AIAA Aerospace Science Meeting Including The New Horizons Forum and Aerospace Exhibition*, number AIAA2009-647, January 2009.
- [99] A. Widenhorn, B. Noll, and M. Aigner. Numerical characterization of a gas turbine model combustor applying scale adaptive simulation. In *Proceedings of the ASME Turbo Expo 2009: Power for Land, Sea and Air*, volume GT2009, 8 June 2009.
- [100] D. C. Wilcox. Reassassment of the scale-determining equation for advanced turbulent models. *AIAA Journal*, 26(11):1299–1310, 1988.
- [101] B. T. Zinn and T. C. Lieuwen. *Combustion instabilities in gas turbine engines*, chapter 1-Combustion Instabilities: Basic Concepts, pages 3–26. American Institute of Aeronautics and Astronautics, Inc., 2005.

Lebenslauf

Persönliche Daten

Name	Francesca Barbara Rebosio
Geburtsdatum	30.05.1979
Geburtsort	Genova (Italien)
Staatsangehörigkeit	Italienisch

Schulausbildung

1985-1990	Scuola elementare "Istituto Santa Dorotea", Genova (Italien)
1990-1993	Scuola media "Istituto Santa Dorotea", Genova (Italien)
1993-1998	Liceo Scientifico "G. D. Cassini", Genova (Italien)

Studium

1998-2004	Università degli Studi di Genova, Facoltà di Ingegneria Meccanica, Genova (Italien)
September 2004	Laurea in Ingegneria Meccanica

Berufliche Tätigkeit

Mai 2005 - April 2011	Wissenschaftliche Mitarbeiterin am DLR in Stuttgart, Institut für Verbrennungstechnik
Seit Juni 2011	Lead Engineer/Technologist am Nuovo Pignone, GE O&G, in Florenz (Italien)